Chemical Process Alternatives for Radioactive Waste

Principal Investigator:

Leonel E. Lagos, Ph.D., PMP®

Florida International University Collaborators:

Dwayne McDaniel, Ph.D., P.E. (Project Manager)
Anthony Abrahao, M.S.
Aparna Aravelli, Ph.D.
Amer Awwad, M.S., P.E.
Mayren Echeverria Boan, Ph.D.
Mackenson Telusma, M.S.
DOE Fellows

FIU | **Applied Research Center**
FLORIDA INTERNATIONAL UNIVERSITY

Addendum:

This document represents one (1) of five (5) reports that comprise the Year End Reports for the period of September 29, 2021 to September 28, 2022 prepared by the Applied Research Center at Florida International University for the U.S. Department of Energy Office of Environmental Management (DOE-EM) under Cooperative Agreement No. DE-EM0005213.

The complete set of FIU's Year End Reports for this reporting period includes the following documents:

Project 1: Chemical Process Alternatives for Radioactive Waste
Document number: FIU-ARC-2021-800012997-04b-006

Project 2: Environmental Remediation Science and Technology
Document number: FIU-ARC-2021-800013918-04b-004

Project 3: Waste and D&D Engineering and Technology Development
Document number: FIU-ARC-2021-800013919-04b-005

Project 4: DOE-FIU Science & Technology Workforce Development Initiative
Document number: FIU-ARC-2021-800013920-04b-017

Project 5: Long-Term Stewardship of Environmental Remedies: Contaminated Soils and Water and STEM Workforce Development
Document number: FIU-ARC-2021-800013922-04b-004

Each document will be submitted to OSTI separately under the respective project title and document number as shown above. In addition, the documents are available at the DOE Research website for the Cooperative Agreement between the U.S. Department of Energy Office of Environmental Management and the Applied Research Center at Florida International University: https://doeresearch.fiu.edu

TABLE OF CONTENTS

LIST OF FIGURES

LIST OF TABLES

PROJECT 1 EXECUTIVE SUMMARY

The Department of Energy's (DOE's) Office of Environmental Management (EM) has a mission to clean up the contaminated soils, groundwater, buildings, and wastes generated over the past 60 years by the R&D and production of nuclear weapons. The nation's nuclear weapons complex generated complex radioactive and chemical wastes. This project is focused on tasks to support the safe and effective storage, retrieval, and treatment of high-level waste (HLW) from tanks at Hanford and Savannah River-sites. The objective of this project is to provide the sites with modeling, pilot-scale studies on simulated wastes, technology assessment and testing, and technology development to support critical issues related to HLW retrieval and processing. Florida International University (FIU) engineers work directly with site engineers to plan, execute, and analyze results of applied research and development. In addition, efforts focus on addressing waste disposal challenges at the sites and issues related to preserving the structural integrity of the H-Canyon Exhaust Tunnel at Savannah River.

DOE Fellows supporting this project include Brendon Cintas (graduate, Ph.D., Mechanical Engineering), Desmond Sinnott (undergraduate, Mechanical Engineering), Gabriel Cerioni (Graduate, M.S., Mechanical Engineering), Joel Adams (graduate, Ph.D., Mechanical Engineering), Josue Estrada Martinez (graduate, M.S., Mechanical Engineering), Nicholas Espinal (undergraduate, Mechanical Engineering), Philip Moore (graduate, M.S., Mechanical Engineering), Rafael Velasquez (Undergraduate, Electrical Engineering) and Sebastian Story (graduate, M.S., Mechanical Engineering).

The following ARC researchers are supporting this project and mentoring the DOE-EM Fellows: Dwayne McDaniel (Ph.D., Engineering Mechanics, Project Manager), Anthony Abrahao (M.S., Mechanical Engineering, Task 18.2.3, 18.2.4, 18.4, Task Manager), Amer Awwad (M.S., Mechanical Engineering, Task 19.2, Task Manager), Aparna Aravelli (Ph.D., Mechanical Engineering, Task 19.1, Task Manager), Jose Rivera (B.S., Civil Engineering, Task 19.2, Research Analyst), Mackenson Telusma (M.S., Mechanical Engineering, Task 18.3, Task Manager), Mayren Echeverria (Ph.D., Chemical Engineering, Task 20, Task Manager), Leonel Lagos (Ph.D., PMP®, Mechanical Eng./Civil/Env. Engineering, PI).

Although several tasks have been initiated and completed over the course of the cooperative agreement, at the end of this past year, there were 4 active tasks. These tasks are listed below, and this report contains a detailed summary of the work accomplished for FIU's Performance Year 2.

Task 17: Advanced Topics for HLW Mixing and Processes

In the U.S. Department of Energy's (US DOE) Savannah River Site (SRS) and Hanford site, systems of pipelines transport high-level radioactive liquid waste for waste processing and storage. After transporting the waste, the lines are flushed with water to ensure that no sludge or sludge solid sediments remain in the transfer line. Current guidelines that establish a minimum flush volume and flush water velocity required for post-transfer flushing operations to achieve a satisfactory cleanliness exist; however, the Defense Nuclear Facilities Safety Board (DNFSB) indicated a need for further investigation on the technical basis for the prescribed guidelines. Consequently, further studies that will assist SRS and Hanford in waste remediation are being done to optimize the operational conditions. This optimization would minimize the flush volume and consequent downstream waste, which ultimately would assist in preserving tank storage,

preventing secondary waste processing, and minimizing changes to the waste's chemistry and rheology.

To perform these investigations, an expandable, 3-inch carbon steel experimental pipe loop was designed and constructed at Florida International University (FIU) to simulate flushing operations of non-Radioactive slurries. The test loop was designed to simulate sediment beds of solid materials and bed heights to investigate what parameters affect the efficiency of flushing operations at various concentrations. Testing was then conducted using non-Radioactive kaolin-water slurry simulants at various concentrations with various flush volume and flush modes to determine the effect of flush volumes for each configuration. These concentrations offer repeatability within the sediment beds inside the pipeline for fully flooded and gravity-drained conditions with one day, one week, and two-week sedimentation. By parametrizing the sediment height and conditions, the flush volume and flush velocity values could be optimized, which leads to satisfactory cleaning of transport lines of varying length with a minimal use of flush water.

This report presents the latest efforts in flush analyses to determine the efficiency of flushing operations. New data with the various configurations for the first of four expansions of the test loop at 330 feet will be presented. This data, which approximates a flush-line volume ratio (FTLV) for fully flooded and gravity-drained conditions with one day, one week, and two-week sedimentation at a range from 2.45 to 2.61, will also be compared to the results from the 165 feet loop. Additionally, the loop will be expanded to 495', and the 330' data and 165' data will be compared to the 495' data when available.

Task 18: Technology Development and Instrumentation Evaluation

Integrity issues in the double-shell tanks (DST) at Hanford have motivated the need for developing innovative tools that can provide information regarding the health of the tanks. These issues include the primary linear failure of AY-102 and recent concerns of thinning in the DST secondary liners. In recent years, FIU has supported DOE-EM by developing tools that can assist in understanding the health of tanks and the waste transport system at Hanford.

FIU has developed a miniature rover that can be deployed through small risers and gain access to refractory slots in the Hanford DSTs. The rover traverses through the slots on the primary liner, via magnets to avoid debris in the slots. The redesigned rover was evaluated in FIU's DST mock up using a test plan that was developed with WRPS engineers. After the testing at FIU, the unit was sent to Hanford for an initial evaluation. Issues were noted related to weld seam traversal so modifications were made to the unit that allows it to navigate over weld seams at oblique angles. Changes also required moving the magnets to the wheels and adding a passive rust removal mechanism. After the changes were made, the minirover was successfully deployed in a DST at Hanford. The unit was able to traverse down to the second major junction in the refractory pad, providing visual feedback of the tank floor.

In addition, FIU has augmented the functionality of the minirover by creating another system that incorporates a UT sensor to take point thickness measurements of the tank floor. Lessons learned from the redesigned minirover deployed at Hanford were also incorporated into the UT rover. The system was then successfully tested in FIU's DST mockup.

To address the secondary liner issue of the DSTs, FIU has continued to develop a marsupial robotic system. It includes a 6-inch peristaltic pipe crawler that operates similar to the previous pipe crawlers developed at FIU that houses a small rover. The objective for this system is to navigate

through the 6-inch drain lines, and deploy the rover at the entrance of the drain slots. The rover is designed with a scissor lift chassis that allows it to navigate on the tank floor or in the slots. A deployment module has continued to be developed to house the rover until the crawler reaches the tank foundation from the drain line. The module sits at the front of the crawler and provides the means for the rover to enter into the drain slots.

During this performance period, however, FIU was asked to change our focus and to investigate the use of an existing 3-inch crawler for its ability to traverse through 3-inch diameter lines underneath single shell tanks (SSTs) and potentially carry a radiation sensor that can be used to inspect for leaks under the tanks. The crawler is a pneumatic system that navigates through pipes using multiple modules that move with a peristaltic-type motion. Multiple aspects of the crawler were upgraded that included adding guides on the modules, improving the controls and adding a reel to control the deployment of the crawler tether. A mockup of the SST line was developed at FIU and the unit was able to transvers through the bend and straight sections. Based on the in-house testing, the unit was taken to the Cold Test Facility at Hanford and was successfully able to navigate through their mockup of the lateral lines.

In addition, FIU is supporting the Savannah River Site (SRS) facility by investigating technologies to evaluate the H-Canyon exhaust tunnel for degradation and potentially assist in avoiding further degradation. Robotic inspections of the tunnel revealed significant degradation of the reinforced concrete structure that was primarily associated with acid attack, and could compromise the structural stability of the tunnel. Thus, the identification and evaluation of potential coatings that could be applied on the degraded walls to mitigate and prevent further degradation is of significant interest to the Department of Energy and the Savannah River representatives. To assist in this effort, FIU is investigating the development of a platform to deploy the potential coatings. A wall crawler system is being developed to climb the walls of the canyon tunnel and will house a mechanism to apply the protective coating. During this past year, efforts have focused on improving the efficiency of the platform by reducing the weight of the chassis and consolidating the on-board electronics. In addition, the electronic ducted fans are being improved by including vector thrust capability and a support arm for the crawler is being developed to offset loads created by applying the coating.

FIU has also recently initiated tasks related to the characterization of EM infrastructure. These tasks will assist DOE-EM and site engineers with understanding various aspects of EM-related sites by using autonomous systems to gather information related to safety and the environmental conditions. Robotic platforms will be developed with an array of sensors that can autonomously provide radiation, LiDAR and other types of maps of the sites while keeping personnel out of harm's way.   This past year has focused on improving the integration and processing of LiDAR data and the localization of the platform. Results are provided that demonstrate the improvements with detailed scans of FIU's facilities.

Finally, during the last year, FIU was asked to develop concepts to assist with sampling tank waste via a robotic manipulator. FIU utilized a UR5 6 degree-of-freedom arm to demonstrate how the arm could be used to conduct various maneuvers and operations. End effectors were added and software was developed to conduct the demonstration at WRPS.

Task 19: Pipeline Integrity and Analysis

Structural health of waste transfer and storage infrastructure is of utmost importance to DOE and communities surrounding the active sites. A Fitness-for-Service (FFS) program for the Waste

Transfer System has been implemented by the U.S. Department of Energy (DOE) through the contractor - Washington River Protection Solutions (WRPS), for the purposes of evaluating and quantifying the structural integrity of critical components such as the pipelines, tanks and tank farm waste transfer system. The purpose of the program is to inspect primary piping, encasements, and jumpers for corrosion/erosion, which this task has assisted with in previous years. Various sensor systems have been investigated, down selected and tested in the past. These included the evaluation of the Ultrasonic sensor system from Permasense for the measurement accuracy and performance under high temperature and humidity conditions and studying the feasibility of radiation effects on the Permasense ultrasonics sensors. Further, SRNL has tasked FIU with lab, bench and engineering scale testing of their patented mass loss coupon technology for small scale wear detection in pipes and transfer lines. The coupons are used to measure slight changes in mass loss due to erosion and to quantify the thinning in the pipe diameter on a precise level using the UT pencil sensor probes. The coupons were able to provide visual erosion when inspected under the microscope/SEM. In Year 2, this task concentrated on completing the carbon and stainless-steel coupon testing on the engineering scale loop with sand and glass particles and initiated the caustic simulant testing. Based on the customized simulant recipe provided by SRNL scientists, a bench scale pipe loop has been designed and constructed at FIU. The loop uses chemical simulants for corrosion testing of the SRNL carbon and stainless-steel coupons. The first phase of testing with 2M salt simulant solutions has been successfully completed this past year and higher concentration testing will follow. Simultaneously, static immersion testing of the coupons has been initiated and 12 months of data (visual, mass change and thickness) has been collected for corrosion evaluation of the coupons. During Year 2, dynamic and static corrosion testing will be continued. Also, during Year 2 fluid dynamic simulations and data analytics models will be developed and used to detect, predict, classify and automate the erosion and corrosion process.

Structural integrity of non-metallic materials is also being investigated under the current research work. Nonmetallic materials used in the Hanford Site Tank Farm waste transfer system include the inner primary hoses in the hose-in-hose transfer lines (HIHTLs), Garlock® gaskets, ethylene propylene diene monomer (EPDM) O-rings, and similar other nonmetallic materials. These materials are exposed to radiation, caustic solutions and elevated temperature and pressure stressors. While the individual effect of these stressors has been well established, their combined effect is of significance to the Hanford site. FIU has been supporting this task by developing a test loop and testing the non-metallic materials under simultaneous stressor exposures.

The objective of this task is also to provide the Hanford Site with data obtained from experimental testing of the hose-in-hose transfer lines, Teflon® gaskets, EPDM O-rings, and other nonmetallic components used in their tank farm waste transfer system under simultaneous stressor exposures. The experiments will be limited to various combinations of simultaneous stressor exposure to caustic solutions, high temperatures and high pressure. Evaluation of baseline materials will be conducted for comparison to materials that have been conditioned with the various simultaneous stressors.

Previous testing included aged HIHTL and material coupons for 6 months and 1 year using elevated temperatures and exposure to caustic material as well as exposure to water only at 170°F. The mechanical and material properties of the samples were characterized and compared with those of the unexposed samples (baseline). Evaluations included burst pressure tests of the EPDM hose-in-hose transfer lines and material tensile strength tests of EPDM dog-bone coupons. It was

observed that both the tensile strength of the EPDM material dog-bones and the burst pressure of the HIHTLs significantly decreased with the increasing temperature and increasing exposure time.

This phase of testing included aging of HIHTL and EPDM dog-bone specimens at various concentrations of NaOH as well as water only at the elevated temperatures. Four test loops were developed at FIU allowing for the aging of HIHTL as well as dog-bone specimens utilizing 6.25%, 12.5% and 25% v/v NaOH and only water respectively at 170°F. After the exposure, the material properties of the specimens were measured and compared to the baseline (unaged) samples. Material properties evaluated included the tensile strength of the EPDM dog-bone samples and the burst pressure of the HIHTL. Both the tensile strength of the EPDM dog-bone samples and the burst pressure of the HIHTL specimens exposed to the 6.25% NaOH solution exhibited the most significant deterioration and those exposed to 25.00% NaOH solution had the least deterioration. Examination of the HIHTL and the EPDM dog-bone specimens with scanning electron microscopy showed that the deterioration for the specimens exposed to 6.25% NaOH solution were the most severe and the samples exposed to 25.00% NaOH solution had the least deterioration.

This task will provide information that will assist engineers with understanding the wear rates in metal pipes and transfer lines along with the effect of various stressors on nonmetallic components. The research will aid in determining the remaining useful life of both metallic and non-metallic components by establishing more detailed/accurate guidelines and avoiding unexpected failures in transfer lines.

Task 20: Corrosion Protection and Characterization of EM Infrastructure

FIU is assisting the Savannah River site engineers with investigations that can assist in the mitigation of degradation of the concrete walls in the H-Canyon exhaust tunnel. The degradation observed could compromise the mechanical strength of the structure. Hence, the search for solutions to mitigate and prevent further degradation is necessary. The identification, evaluation and selection of the best coating candidate that can be applied to the tunnel's degraded concrete walls constitute the main goal of this investigation. The investigation has been divided into different phases: 1) development and evaluation of aged concrete surfaces under accelerated aging conditions and, 2) identification and evaluation of potential coatings applied on aged and non-aged concrete under accelerated aging conditions (preliminary results presented in this report).

During Year 1, efforts were focused on the identification and preliminary evaluation of potential coating candidates for the protection of the degraded concrete walls of the HCAEX tunnel. A comprehensive test plan for the evaluation of the coated surfaces was developed and executed including key variables such as 1) surface preparation, 2) aging conditions of the substrate and 3) presence of rebar. The selected coated samples were exposed to accelerated aging conditions combining a 0.5M nitric acid solution and erosion. Major findings during this year included the preliminary evaluation of selected coating candidates (Carboline and Belzona) for the protection of the tunnel walls. Visual inspection, failure analysis and thickness measurements showed slow degradation of the coatings over time. The degradation of the coatings was characterized by loss of coating particles and in some cases, detachment of some coarse aggregates. The reduction of thickness over time, for all tested coatings, indicated degradation and loss of protective properties. The erosion of the surfaces played a key role in the degradation of the coatings.

FIU is also working on a new task with the Hanford Site. A current challenge for DOE and relevant DOE sites is to understand the durability of the steel canisters/containers that will contain low-activity waste (LAW) and secondary waste forms, encapsulated in glass and grout respectively,

and that will be placed within the Integrated Disposal Facility (IDF) at Hanford. Currently, corrosion data of the steel and weld regions of the canisters at Hanford that is exposed to groundwater is limited. In addition, there is limited information on groundwater in contact with waste forms. The primary technical need is to study the corrosion rate of the steel canister's exterior that is exposed to Hanford groundwater and determine how well it shields the waste form that is inside the canister from exposure. During Year 1, efforts were concentrated on initiating the evaluation of 304 stainless steel in contact with a Hanford simulated groundwater solution through electrochemical measurements. Electrochemical measurements were conducted including corrosion potential (Ecorr), linear polarization resistance (LPR) and potentiodynamic polarizations (PDP) in two different Hanford groundwater solutions. Before that, a Faraday cage for electrochemical measurements was designed and built, facilitating the execution of the electrochemical testing.

MAJOR TECHNICAL ACCOMPLISHMENTS

Task 17: Advanced Topics for HLW Mixing and Processes

- FIU presented 8 posters and 6 oral presentations based on Project 1 research results at the WM2022 Symposia in Phoenix in March 2022.

- After construction of the 330 ft flushing loop, leak tests were conducted. Although the loop was found to not have any leaks, a low spot in the loop was discovered that makes it difficult to remove all liquid from the loop. The loop point was raised eliminating any drainage issues.

- A new data acquisition system has been installed for the loop sensors and a Labview VI has been generated that control the sensors and data flow. Preliminary tests have confirmed operation of the new instrumentation and a trial run was completed for the 330 ft loop.

- For the flushing effort, trials continued with the 330 ft flushing loop. Results were obtained for the 10% and 15% concentrations of kaolin for the gravity drained and fully flooded conditions. Flush-to-line-volume ratios were between 2.45 and 2.61. Testing continued with the preparation of two batches of 10 vol.% slurry simulant to be gravity-drained for two weeks to consider the effects of long-term sedimentation with the extended length. Results demonstrated a slightly higher FTLV required to flush the extended sedimentation versus the average results of the 15% condition.

Task 18: Technology Development and Instrumentation Evaluation

- Efforts for the SST focused on integrating the controls into the tether reel. The reel was divided into two sections: one section for the tether and the other section for the controls which were mounted on the external part of the reel. A cover was printed to protect the control from external elements. The SST lateral gamma scanner crawler system was then tested in FIU's mockup that consisted of a large radius bend with approximately 100 ft of straight pipe. FIU deployed and demonstrated the lateral gamma scanner pipe crawler in March 2022. The pipe crawler, with three small tubes emulating gamma radiation sensors, was deployed at Hanford's Cold Test Facility (CTF), traversing down a vertical section, through an 8 ft radius of curvature elbow, and then through approximately 100 ft of straight sections. The pipe crawler was able to successfully navigate through each section and was also retrieved manually to demonstrate its removal in case of a failure.

- FIU delivered and deployed the miniature rover to WRPS engineers during the month of March 2022. The FIU technology was initially evaluated in a mockup of the tanks and WRPS operators were given a short training. On March 22, 2022, the unit was deployed in AP-105. The mini-rover was deployed through a 4-inch riser and driven down the tank wall. It then entered the refractory slots and continued to the second turn under the tanks. It was then driven back out, having no issues during the deployment.

- FIU conducted a proof-of-concept demonstration at WRPS. DOE Fellow, Joel Adams, demonstrated the feasibility of utilizing a 6 degree-of-freedom robotic manipulator as a tool to perform off-riser sampling operations. The manipulator was placed upside down,

emulating the required orientation for a manipulator when deployed through a riser, and performed various scooping operations to show how the system could be used to collect samples near the riser.

- FIU investigated the incorporation of a support arm for the wall crawler for the H-Canyon tunnel effort. A support bracket has been designed that will allow for an arm to extend from the mother platform and provide stability during coating operations.

- In addition, for the H-Canyon robotic wall crawler effort, teleoperation capabilities were added to the controls of the support arm structure along with the continued development of the vector thrust technology needed for the platform. The dual EDF platform was completely assembled along with initial testing for power distribution and EDF performance.

- FIU attended the DOE-EM sponsored D&D Workshop hosted by SRNL at the Georgia Cyber Center in Augusta, GA from April 25-28, 2022. A presentation titled "Robotic Technology Development for Decommissioning Applications" was delivered based on the research and technology development and deployment efforts conducted under Project 1.

Task 19: Pipeline Integrity and Analysis

- The SRNL mass loss coupons were tested for chemical corrosion for a period of 6 months immersed in 2, 4 and 6 Molar concentrated solutions. The recipes for the solutions were provided by SRNL scientists. It was observed that 6M carbon steel coupons were most corroded while pitting corrosion was observed in stainless steel coupons. The static testing results will provide baseline data for dynamic chemical corrosion tests on the bench scale loop developed at FIU recently.

- FIU completed testing of the erosion loop using glass beads. Results demonstrated that the erosion with bead sizes AE and AC with 10% volume fraction and 45 hours of testing had very minute levels of erosion. FIU will work with engineers at SRNL to determine additional bead sizes and concentrations for further evaluations.

- Computational Fluid Dynamics (CFD) simulations were initiated to study the pipe flows using fundamental structure of the engineering and bench scale loops. Results indicate high flow velocity and high-pressure regions and provide a basis for future evaluation of multi-phase flows and particle erosion effects.

- Framework for machine learning models has been developed to customize the erosion and corrosion effect on the SRNL coupons. Initial results using Convolution Neural Networks (CNN) models indicate an average of 87.5% accuracy in corrosion prediction.

- Riverbend HIHTL as well as EPDM material coupons were aged for 1 year at 170°F with three concentrations of NaOH (6.25, 12.5 and 25%). Burst pressure tests were conducted on the aged and baseline coupons. Interesting results were obtained with the lower concentration and water only aged samples having the largest reduction in burst pressure. The results were discussed with engineers at SRNL and at WRPS.

- FIU completed the material testing of the HIHTL coupons and dog bone coupons. A summary document was submitted summarizing the results.

- FIU completed the retesting of dog bone coupons aged at 170°F with three different concentrations of NaOH. The specimens were aged for 4 weeks and demonstrated similar trends seen in the burst pressure tests. In addition, the aging data was used to generate a prediction formula for burst pressure vs aging for each of the testing phases. The aged dogbone coupons were evaluated using an SEM. As with the previous results, the SEM scans showed increased degradation at the lower concentrations of NaOH. The EPDM dogbones were aged with three NaOH solutions at 170°C (6.25%, 12.5% and 25%).

- Surface porosity and roughness analysis on the dog-bone specimens was conducted. ImageJ software was utilized for the analysis and the results showed that when compared to the baseline (unaged) dog-bones, the surface roughness (Ra) for the dog-bones aged with 6.25%, 12.50%, 25.00% NaOH, and water only increased by 325.16%, 212.53%, 181.00%, and 50.34% respectively. In addition, the porosity (% area) for the dog-bones aged with 6.25%, 12.50%, 25.00% NaOH, and water only increased by 868.95%, 415.82%, 349.36%, and 55.67% respectively. In addition, SEM-EDX analysis was conducted on EPDM dog-bone specimens that were aged with 6.25%, 12.50%, 25.00% NaOH. Results showed Na counts on cross sections of the coupons and confirmed the level of penetration of Na. The results also compared well with the tensile tests.

- Published findings from previous year's research in the Engineering Failure Analysis Journal titled, "Effect of temperature and aging duration on ethylene propylene diene monomer (EPDM) nonmetallic components used in caustic liquid waste transfer lines".

Task 20: Corrosion Protection and Characterization of EM Infrastructure

- Potential coatings (coating systems and single coatings) for the protection of the H-Canyon Exhaust Tunnel walls were identified.

- Carboline and Belzona coated samples initiated the accelerated aging process.

- Preliminary evaluation of the Carboline and Belzona coatings was completed.

- Impedance measurements, with a new procured potentiostat, supported the evaluation of the coating's protective properties.

- Faraday cage for electrochemical measurements was designed and built.

- The potentiostat was set up and overload issues of the potentiostat were resolved. Preliminary corrosion data for 304 SS samples immersed in Hanford simulated groundwater were obtained through electrochemical tests (Ecorr, LPR and PDP).

TASK 17: ADVANCED TOPICS FOR HLW MIXING AND PROCESSES

Subtask 17.2: Evaluation of Pipeline Flushing Requirements for HLW at Hanford and Savannah River Site

Subtask 17.2: Introduction

US DOE sites within the DOE-EM complex, though especially at Savannah River Site's (SRS) Defense Waste Processing Facility (DWPF) and Hanford's Direct-Feed Low-Activity Waste (DFLAW) and Waste Treatment and Immobilization Plant (WTP) are prescribed recommended flushing parameters that establish a minimum flush volume and flush velocity of water required to ensure proper cleaning. This prescription ensures that the pipelines that transfer the high-level radioactive waste are flushed without the solids eroding the pipe, and to also ensure that the post-transfer flushing operations result in a satisfactory cleanliness of the pipes, where there are no residual solids remaining inside the pipeline post-flush. The Defense Nuclear Facilities Safety Board (DNSFB) has indicated a need for vigorous investigation on the technical basis for prescribing flush velocity in pipelines to determine the optimal performance at the Department of Energy sites. The DNFSB justifies this need because transfer of the waste must be operated at a critical velocity of fluid flow to: (a) prevent residual formations from solids sedimentation within the pipe bed and (b) ensure that during the transfer operation, the insoluble solids within the sludge waste do not erode the pipe walls. Additionally, the correct amount of water is used to effectively clean the pipeline without producing surplus secondary waste that would also need to be treated. If flushed improperly, partial or full granular plugs and H-gasses can build up, which result in process upsets, costly delays and potential need for line repair or line abandonment, equipment overloads, or possible destruction of equipment such as a rupture at the pump or within the pipeline [5]. The pretreatment facility design strategy requires that each slurry transfer in the process lines be followed by a flush with water to minimize the chances of a partial or full line plug.

Several studies were done to determine the current prescribed flushing guidelines at Pacific Northwest National Laboratory (PNNL) at the Hanford Site. These studies revealed that the minimum required flush volumes were more than the minimum required values provided by certain design guidelines. The flush velocity that was recommended for a slurry up to 30 Pascals of yield stress is 10 ft/sec to adequately flush the system. Flush velocities in the pipeline exceeded the maximum velocity stated in the flushing guidelines [2] that ensure that the interior of the pipeline does not erode due to the solid particles within the slurry that are agitated during transfer and flushing. In the same study, it was demonstrated that "a flush-to-line volume ratio (FTLV) of 3 was needed to remove sediment bed […] whereas design guide […] provides a minimum flush-volume ratio of 1.7" [3]. From the design guidelines and the study, the prescribed minimum is 1.7 times the volume of the pipeline (an FTLV of 1.7), whereas the actual flush volumes to ensure cleanliness were closer to nearly triple the FTLV.

At Florida International University – Applied Research Center (FIU-ARC), investigations to determine effective flushing operations using a minimal amount of water and to provide additional guidelines in support of recently developed flushing standards indicated by TFC-ENG-STD-26 [4] have been underway. Effective execution of the work requires creation and characterization of sediment beds and their solids concentrations, flushing in different modes, and evaluation of operation effectiveness through post-flush sampling. To extend previous flushing studies, the focus was to create different case studies targeting different materials and pipe lengths. Focus was on

influential parameters set for one simulant in a fixed pipe length for each round of testing. These parameters include varying the initial conditions of the sediment such as the concentration of the solid and its corresponding settlement height, settlement time of one day and one-week flush operation (fully-flooded and gravity-drained).

Subtask 17.2: Objectives

The objective of this effort is to provide a technical basis for flush volume used in the waste transfer process. This includes:

- Implementing optimal flush operations that minimize waste production, pipeline erosion, and ensure satisfactory cleaning of pipelines based on an established criterion for thorough discussions between FIU and personnel at the waste sites and national laboratories.

- Developing a correlation for flush parameters based on characteristics of the system at the start of flushing (initial conditions). Data and correlations will be useful for determination of pumping requirements improving existing guidelines.

Subtask 17.2: Methodology

The experimental set up consists of a test loop composed of 3-inch schedule 40 carbon steel pipes and fittings (Figure 1 and Figure 2). This test loop can perform various functions such as slurry circulation, pump cleaning, flushing, sediment and water retrieval, and post-flush circulation. The pipeline was sloped at the rate of 0.15% (to emulate conditions at Hanford Site and facilitate gravity draining) [5]. A 15 HP centrifugal pump controlled by a variable frequency drive (VFD) is used to circulate the simulant, flush with water, and conduct post-flush analyses. The fluid level, flow speed, and fluid density are monitored using sensors – the VEGAPULS 11 radar sensor and the Krohne Optimass 1000 Coriolis meter, respectively - that report the status of these parameters in real time.
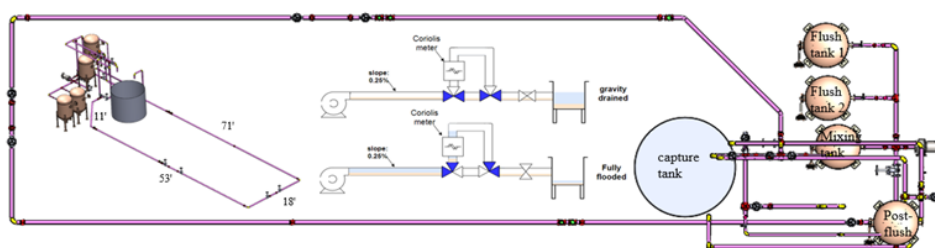
Figure 1. CAD model of the 165-foot pipeline used for flushing experiments.

Figure 2. Constructed 165-foot pipeline for flushing experiments.

Several changes were made to the flushing loop to implement the first phase of the loop expansion from 165 feet to 330 feet of length without altering the general configuration of the loop, as shown in Figure 3. To expand the loop, the ninety-degree intersection was temporarily removed, and eight 20-foot sections (four per side) were added. After ensuring each 20-foot section was at the correct slope to simulate the elevation changes at Hanford and SRS' transfer lines, the ninety-degree section was replaced.

330-feet (New Loop) ■ 165-feet (Old Loop)
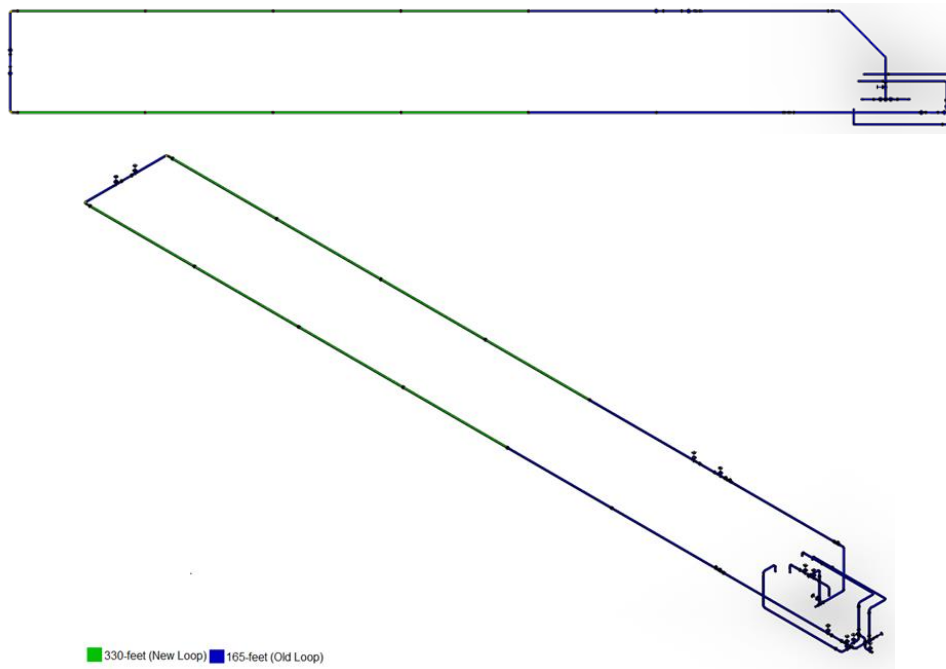
Figure 3. CAD model of the updated 330-foot flush loop.

Figure 4. Constructed 330-foot extension used for flushing.

During the data collection for the 165-foot loop, it was noticed that for the gravity draining operation, some water remained inside the line after the draining completed when observing the clear section. This was likely due to the original gravity drain discharge valve at the tank farm, shown in Figure 5, being higher than the affected portion of the line. For the 165-foott loop, the volume of water that would remain inside the line was enough to not adversely affect the sedimentation of the kaolin. By relocating the gravity drain discharge valve inline at the far end of the loop, the potential risk of water remaining in the loop and adversely affecting the gravity-drain operation is minimized, especially for larger solid concentrations.

Figure 5. Gravity drained discharge valve at the 90-degree section of the flushing loop.

Improvements to Instrumentation and Data Reporting

Additionally, improvements to the instrumentation to capture, read, and export the data was improved. Alongside the construction of the 330-foot extension, a new data acquisition (DAQ) system – the NI USB6001 DAQ was procured and installed. Because of the age of the previous DAQ – the NI FieldPoint 2010, a reprogramming of the LabView VI, which handles the inputs from each sensor, converts the data from a 4-20 mA output into legible values, and stores them for

analysis, was rewritten. After validating the functionality of the DAQ through bench-scale tests, the DAQ and VI were deployed and each sensor was connected and tested for legible outputs within the 4-20 [mA] range, where 4 mA is the minimum reading on the sensor, and 20 mA is the maximum reading on the sensor. Each sensor was tested and calibrated:

a. The level sensor was connected to Channel 0 on the data acquisition system. The change in current was monitored while the level sensor's height over the ground was changed. After, the level sensor was placed at the top of one of the two water reservoirs at the loop's tank farm and checked to see if the calibration of the sensor reported an accurate fluid level, which was validated using a visual inspection of the fluid height.

b. The density sensor was connected to Channel 1 on the data acquisition system. The change in current was monitored while the Coriolis meter was filled with water where air was previously present. Before the Coriolis meter was flooded with water, the current and corresponding density of air was noted, and after flooding, the current and corresponding density of water was noted to create the calibration curve for this sensor.

c. The flow rate sensor was connected to a PRO-FLO200 Flow Batching Totalizer that converts the digital pulses of the flowmeter to a 4-20 mA output. This totalizer was connected to Channel 2 on the data acquisition system. The change in current was monitored while the VFD frequency was varied from 0 Hz to 50 Hz, with the standard operating frequency used in testing (35 Hz) as an intermediate value.

Figure 6. NI-USB6001 Multifunction I/O data acquisition unit.

Lastly, further improvements were made to the data analysis methods via implementation of a stream-lined post-processing script. The script reads the data directly from the .LVM output file from the LabVIEW VI and uses Gaussian smoothing. The density curve can be smoothed to represent a more accurate visual of the density's behavior during the flushing operation. Lastly, the script will automatically export a plot of: (a) the density/flowrate curves as a function of time and (b) the density curve as a function of the flush-line volume ratio that is generated from real-time calculations within the VI. Logic was implemented in the post-processing script, where the script inspects the dataset and determines when the density curve approaches the target cleanliness. The code logic allows an FTLV value to be approximated instead by determining the rate of change of the density curve (its slope value). If the slope is less than a predefined tolerance by the operator, it forecasts the slope values for a predefined forecast range (e.g., check the slope values of the next 50 data points past the initial value), and stores each value into an array. The array is then averaged,

and if the average is less than the predefined tolerance, the program validates a steady state has been reached, and the FTLV value of the initial data point within the steady state array is returned.

Flushing Operation

EPK kaolin with a 2.65 specific gravity was used in tests with both the gravity-drained and fully-flooded conditions. Flushing tests were conducted with system loads of 10, 15, and 20% vol of kaolin-water mixtures using a pump frequency of 35Hz to target a flow velocity below 10 ft/s. Tests were performed using two initial conditions: a fully-flooded condition and a gravity-drained condition. In the fully-flooded condition, the test loop was flooded with a simulant of a specified concentration and left to settle for approximately one day after stopping the slurry pump and without any changes to configurations or system environment. After the settling period, water from flush tanks was flushed through the system using the 15HP pump into a 500-gallon collection tank. In the gravity-drained condition, similar to the fully-flooded condition, the test loop was flooded with a simulant of specified concentration and left to settle for one day for nominal testing.

For the 15% gravity-drained condition, studies were also conducted with variable settling times to determine the effect of prolonged sedimentation times on flush volume requirements. In these trials, the gravity-drained condition was created as described above, but the settling time was increased to one and two weeks before being drained and the test conducted. After the amount of time had passed, a drain valve was opened to remove the water from the settled kaolin, leaving behind a layer of sediment exposed to air within the pipeline. Water was then flushed through the system back into the collection tank.

To determine the effect on flush volume requirements when the flow is pulsated, a trial was conducted for the 15% gravity-drained case by varying the pump's VFD from 0 to 35 Hz over 2 seconds in the ramp-up and ramp-down stages. During each pulse, 35 Hz was maintained for 7 seconds, and 0 Hz was maintained for 1 second before beginning the next pulse. This process was then repeated until the pipe was considered flushed.

Subtask 17.2: Results and Discussion

During the trials, the slurry pump was run long enough to ensure complete flushing, and the data collected was analyzed to determine the actual volume required to clean the system. The calculation of the flush-to-line volume ratio is show in the next section. For the analysis, the clean condition was determined by the Coriolis meter's density reading (showing approximately the density of water). Flow quantities such as mass flow rate and density were also recorded using a data acquisition (DAQ) module (NI USB6001) and a PRO-FLO200 totalizer. Results from the fully-flooded condition are shown in Figure 7 and Figure 8 and results from the gravity-drained condition are shown in Figure 9 and Figure 10. The plots show both the density and flow rates verses time for the three concentrations and for each initial condition.

For the three fully-flooded tests, the density curve starts at just above 1,000 kg/m^3, increases as more fluid with solid particles flows through the Coriolis meter, and decreases to approximately the density of water after all the particles are removed. For the gravity-drained condition, the density starts at zero and increases as the slurry moves through the meter. When the pipe is flushed, the density again returns to just below or just above 1,000 kg/m^3.

Results from the 10% gravity-drained condition (Figure 9 and Figure 10) show an initial oscillatory behavior in the mass flow rate, and consequently, a decrease in material density. This behavior ceases after approximately 20 seconds before it returns to the expected flow pattern. This trial was

conducted multiple times, each time, resulting in the same pattern. It is likely that cause of this behavior is due to resuspension of the solid with water, and during the flushing operation, air is forced from the system as the resuspended mixture flows through the Coriolis meter's flow gauge. This behavior is shown to a smaller extent for 15 vol.% and will be investigated in future trials. In addition, the flow rate for the 20% gravity-drained trial (Figure 6, bottom) was higher than expected for the pump VFD setting of 35 Hz. Results show a quicker return to the nominal density of water, however, as discussed in the next section, the FTLV ratio was consistent with other trials. Figure 11 shows the results for the extended settling time. For the two-week settling trial, it can be that the approximate flush-line volume ratio is higher than the one-day sedimentation. The explanation of why more volume of water may be required is discussed in further detail in the next section.

Fully-Flooded Condition
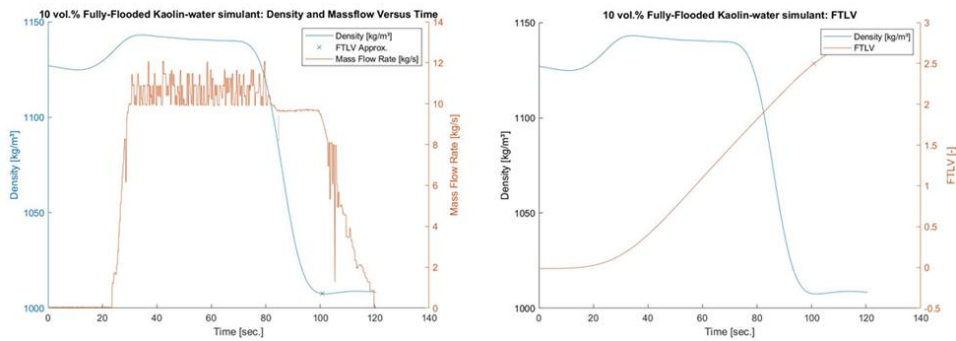
Figure 7. 10 vol.% fully-flooded kaolin water simulant: (left) density and mass flow vs time (right) approximate FTLV.
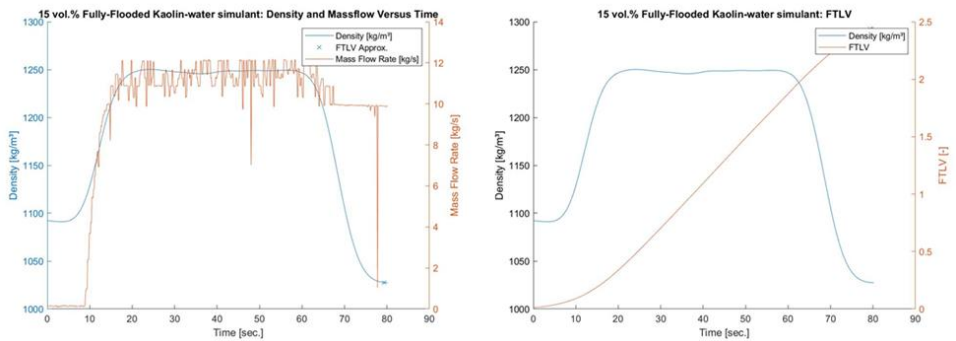
Figure 8. 15 vol.% fully-flooded kaolin water simulant: (left) density and mass flow vs time (right) approximate FTLV.

Gravity-Drained Condition
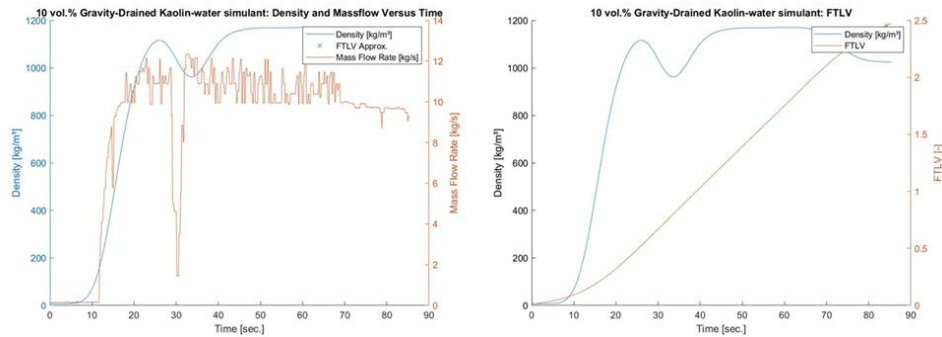
Figure 9. 10 vol.% gravity-drained kaolin water simulant: (left) density and mass flow vs time (right) approximate FTLV.
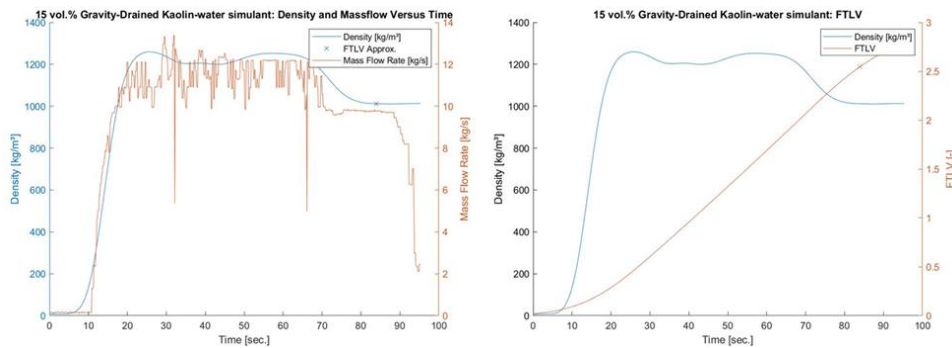
Figure 10. 15 vol.% gravity-drained kaolin water simulant: (left) density and mass flow vs time (right) approximate FTLV.

Gravity-Drained Condition: Extended Settlement
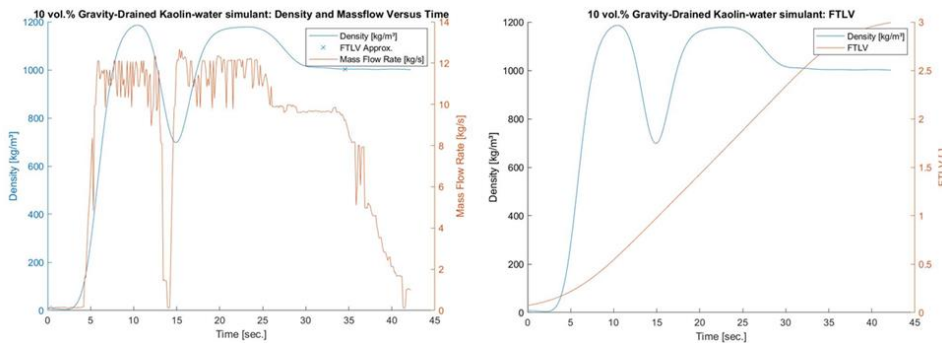
Figure 11. 10 vol.% gravity-drained kaolin water simulant – extended settlement (2 weeks): (left) density and mass flow verses time (right) approximate FTLV.

Flush-Line Volume Ratio

The flush-to-line volume ratio is a ratio of the volume of water being used to flush the line, with respect to the volume of the pipeline.

$$FTLV = \frac{\text{volume used to flush}}{\text{pipeline volume}}$$

In the test loop, the level sensor was installed on the top of the water reservoir tank to monitor the change in volume of the water within the reservoir tank. This parameter was then utilized to

determine the volume of water used to flush by detecting a change of water level within the water tank. During the flushing operation, this variable is monitored coincidentally with density and mass flow rate and saved onto a file for analysis via a script. Results (Table 1 and Table 2) show the FTLV ratios determined by the post-processing script for (a) default settlement time and (b) extended settlement. The results in the tables indicate there is no substantial change when varying the solids concentration for the fully-flooded condition. This is likely to do with the separation of the column of water and the solids; because water is already present, it is possible that this contributes to the resuspension of the solids, removing it from the line faster and therefore not requiring as much water to flush. This is further exemplified with the gravity-drained condition, where the difference between the 10 vol.% and 15 vol.% for gravity-drained tests showed no considerable difference in the amount of water needed to clean the loop; however, when comparing the gravity-drained to fully-flooded – particularly for 15 vol.%, nearly 5% more water is needed to effectively clean the same amount of solids. Extended sedimentation of 10 vol.% kaolin-water simulant, shown in Table 2, indicates a considerable change in the amount of water needed to flush between one week and two weeks. In this table, an FTLV of 2.46 was needed for one day sedimentation, whereas a two-week, extended settlement required nearly over 10% more water. For all the conditions evaluated, the FTLV obtained was 2.5 or below. The conditions included varied volume concentrations (10, 15 and 20%), test conditions (fully-flooded and gravity-drained), and variable sedimentation (1 day, and 2 weeks).

Table 1. Flush-to-Line Volume Ratio Results, One-Day Sedimentation

One Day Sedimentation FTLV Results		
	Fully Flooded	Gravity Drain
10%	2.47	2.46
15%	2.43	2.54
20%	TBD	TBD

Table 2. Flush-to-Line Volume Ratio Results – Extended Settlement

10 vol% Variable Sedimetation Results	
One Day	2.46
1 Week	TBD
2 Weeks	2.71

Subtask 17.2: Conclusions

Results were presented that demonstrate flushing of 10% vol and 15% vol concentrations of kaolin-water slurry sediments within a 3-inch diameter, 165-foot pipe loop using fully-flooded and gravity-drained conditions. Results demonstrated that flushing with these conditions required a flush-line volume ratio of approximately 2.5 using data from the Krohne Optimass 1000 Coriolis meter and VEGAPULS11 level sensor. Via post-processing and code logic, the flush-line volumes were determined. Future work for this research effort includes expanding the test loop to 495 feet, which considers partially redesigning the tank farm and sloping; additionally, with comparable datasets to the 165' loop, computational modeling of the test loop using the parameters from the experimental setups to predict performance at significantly longer lengths and unique geometries will be considered.

Subtask 17.2: References

1. R. Kazban, A., "Plugging and Wear of Process Piping at The Waste Treatment and Immobilization Plant", DNFSB/TECH-40 (2016)

2. A. Poloski, M. L. Bonebrake, A. M. Casella, M. D. Johnson, P. J. MacFarlan, J. J. Toth, H. E. Adkins, J. Chun, K. M. Denslow, M. L. Luna, J. M. Tingey, "Deposition Velocities of Newtonian and Non-Newtonian Slurries in Pipelines", PNNL-17639, WTP-RPT-175 Rev. 0, (2009)

3. S. T. Yokuda, A. P. Poloski, H. E. Adkins, A. M. Casella, R. E. Hohimer, N. K. Karri, M. Luna, M. J. Minette, J. M. Tingey, "A Qualitative Investigation of Deposition Velocities of a Non-Newtonian Slurry in Complex Pipeline Geometries", PNNL-17973, WTP-RPT-178 Rev. 0, (2009)

4. N. Hall, "Minimum Flow Velocity for Slurry Lines", 24590-WTP-GPG-M-0058, Rev 0 (2006)

5. Kazban, A., "Plugging and Wear of Process Piping at The Waste Treatment and Immobilization Plant", DNFSB/TECH-40 (2016)

6. B. Cintas, S. Tashakori, D. Sinnott, D. McDaniel, A. Aravelli, M. Poirier, "Evaluation of Pipeline Flushing Requirements for High-Level Waste at Hanford and Savannah River - 22128", Proceedings from the Waste Management Symposia 2022, March 6 – 10, 2022, Phoenix, Arizona, USA

TASK 18: TECHNOLOGY DEVELOPMENT AND INSTRUMENTATION EVALUATION

Subtask 18.2: Development of Inspection Tools for DST Primary Tanks

Subtask 18.2: Introduction

As part of the Hanford Site DST and SST integrity program review, engineers at Hanford are investigating robotic technologies that can be used for the evaluation of DST and SST tank integrity. The technologies are intended to provide video and other sensory feedback of the tank primary and secondary liners so that an assessment can be made regarding the structural integrity of the tank bottom. Hanford's DSTs have three direct paths of access to the liners: 1) refractory air slots though the annulus, 2) a 4-in annulus air supply pipe to the central plenum, and 3) a 6-in leak detection pit drain from the central sump. SSTs have one indirect viable option of assessment of the primary liner integrity: lateral pipelines installed under the tanks during construction.

Subtask 18.2: Objectives

The objective of this task is to develop inspection tools that can provide information regarding the DST bottoms from within the insulation refractory pads, concrete foundation leading to the tank liners, and SST leaks via gamma scanning from underground laterals. FIU engineers continued to work directly with WRPS site engineers to develop and test systems that can assist in the health assessment of the tanks. After the technologies have successfully demonstrated specified capabilities, FIU worked with site engineers to meet requirements for deployment at the sites. Specific subtasks included:

- Improving a magnetic miniature rover system to navigate remotely controlled through the refractory pad channels and the drain slots of DST tanks and providing visual feedback. The miniature rover system has been successfully tested in a full-scale sectional mock-up test bed and initially deployed at the Hanford site. Lessons learned from the first deployment drove additional design modifications in collaboration with WRPS.

- Developing and improved miniature magnetic rover that can provide point ultrasound thickness measurements of the tank floor from within the slots.

- Retrofitting a previously developed crawler to navigate through the lateral lines underneath the single shell tanks (SSTs) and provide information regarding potential leaks.

- Testing and improving the design for a 6-inch crawler that can navigate through the drain lines to the concrete foundation of the DSTs. A new miniature rover housed in a 6-inch crawler has been developed to deploy and inspect the secondary liners.

Subtask 18.2: Methodology

The approach taken for the development of inspection tools for use at Hanford Site has been to start with concepts that address the necessary issues and work with Hanford engineers to down select from the ideas and focus on the concepts. Once a concept has been vetted, FIU engineers design and develop an initial prototype. Bench scale tests are then conducted to demonstrate the validity of the concepts and develop an understanding of where improvements are needed. After a prototype has been developed and determined to be functional, the system is tested in a mockup

built at FIU. Typically, after testing in our mockups, improvements are made to address issues noted during testing. Issues such as improved functionality and durability are then addressed. Once engineers at Hanford are satisfied that the system meets the necessary requirements, the units are taken to Hanford to test in their Cold Test Facility or for deployment.

FIU has developed inspection tools that can traverse through the refractory slots and through the air supply lines. FIU has also constructed a mockup of the DSTs for cold testing of the inspections systems. During FIU Year 2, FIU continued further optimizing the existing inspection tools with the assistance of site engineers. However, during this past performance period, WRPS requested FIU to shift efforts from the DST secondary liner marsupial system development to focus on the development of an SST lateral gamma scanner inspection tool. Thus, FIU has dedicated efforts to retrofit a previously developed crawler for the DSTs that can navigate through lateral lines underneath the SSTs and provide information regarding potential leaks by scanning gamma radiation levels.

Subtask 18.2: Results and Discussion

The progress made on the development of FIU inspection tools for Hanford tank farm is presented below.

Subtask 18.2.1: Support for Deployment of Miniature Rover at Hanford

In the previous performance period, FIU made modifications to the miniature rover based on new information acquired from the first deployment at Hanford DSTs. The magnets were relocated to the unit's wheels allowing the rover to overcome blunt weld seams located in the refractory slots. A flexible material called thermoplastic polyurethane (TPU) was also used to improve the duration of contact between the wheels and the tank's liner. Torsion in the V-shaped member allows the rover to flex when either the front or back wheels are unevenly displaced. This mechanism lets the rover traverse weld seams at angles nearly parallel to the channel lengths. The newly modified unit was then tested according to a test plan approved by engineers at WRPS.

Upon completion of the WRPS-approved testing performed at Florida International University's full-scale mockup, and working directly with the subject matter experts involved with the tank integrity inspection program, the mini rover system was deemed fit to deploy at Hanford's Cold Test Facility. Figure 12 shows FIU's Mini Rover inspection system.

Figure 12. FIU's Mini Rover inspection tool system.

On March 21, 2022 the mini rover system was tested at IVITS in Richland, Washington (Cold Test Facility). Figure 13 shows images of the Cold Test Facility training and the testing. There were a number of operators and WRPS management personnel on-site to evaluate the capabilities of the

rover. The mini rover managed to surpass the expectations of all personnel present during the rigorous tests it encountered and was unanimously voted to be deployed the following day.

Figure 13. Mini rover tested at IVITS facility and actual deployment at AP-105.

After the traning and evaluation at IVITS facility, the mini rover was succesfully deployed at Hanford to inspect the AP-105 DST, as illustrated in Figure 14. The rover was deployed through the riser located at grade and lowered down via the deployment tray. Upon being lowered to the appropriate length, the rover traversed down the tank wall in the anulus and entered the refractory air slot. Upon the successful inspection of the refractory slot, the rover returned to the deployment tray and was retrieved with its condition operating at full capacity.

Figure 14. Hanford AP-105 DST deployment.

Figure 15 shows a rust management test at FIU's full scale mockup. The exaustive in-house testing done in coordination with WRPS site engineers was crucial to replicate the DST's existing conditions accurately, which was curcial for the successful deployment of FIU technology at

Hanford's tank farm. The lessons learned from the deployment has been paramount for other deployments in the FIU's technology development roadmap pipeline.

Figure 15. FIU's in-house testing (left) and retriever rover after AP-105 DST deployment (right).

This mini rover subtask has been successfully completed and the technology transferred to the DOE Hanford Site. WRPS has requested five more units from FIU, as well as enhancement of the current mini rover integrating sampling tools for material retrieval under the DSTs.

Subtask 18.2.2: UT sensor miniature rover

In the previous performance period, FIU made significant improvements to the UT sensor rover including the incorporation of a cleaning mechanism that can remove debris from surfaces prior to measurements. In addition, a means to apply couplant was also incorporated and allows for significantly more accurate measurements. The system was capable of navigating in the mockup at FIU and could provide reliable measurements for the thickness of the tank floors. Figure 16 shows the original UT rover prototype.
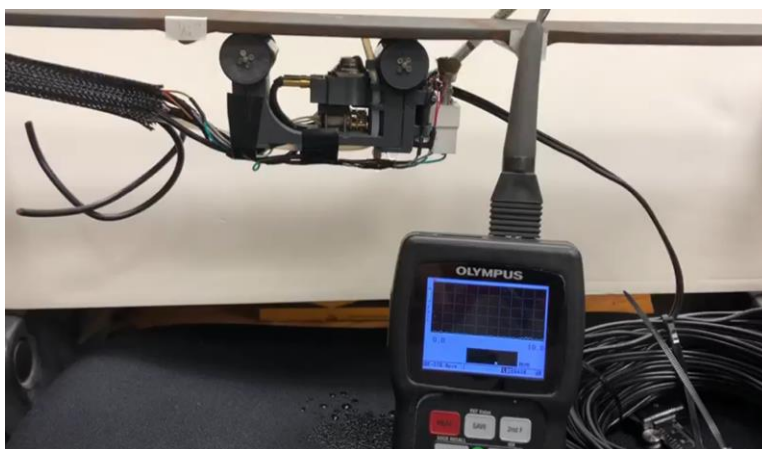
Figure 16. FIU's original UT rover prototype.

Figure 17 shows the UT rover's sensing equipment, a significant challenge in the chassis redesign. The current system integrates an ultrasonic sensor probe, 100 feet tether, and gage to measure primary liner thicknesses. A polyurethane tube within the tether delivers the couplant water required by the sensor.

Figure 17. Current UT rover sensing equipment.

With the successful deployment of the mini rover at Hanford's tank farm, design changes were incorporated to the original UT Rover. The major changes consisted of the magnets being transferred from the body to the wheels and reduction of the overall size of the rover chassis. Minor changes included improved sensing device, software framework, and hardware. The UT probe mechanism was also redesigned to accommodate the new changes. A flexible chassis was also incorporated to accommodate traversing over oblique weld seams the rover will expect to encounter during deployments.

Figure 18 shows the redesigned flexible chassis. The compliant UT rover chassis was prototyped to tackle oblique weld seams and maintain magnetic adhesion to the primary liner.

Figure 18. Compliant UT rover chassis.

Illustrated by Figure 19, the flexible material also behaves like a buffer for the unit reducing the stresses experienced by the chassis while the wheels are interacting with the curved surface of the weld seam. The unit overcomes weld seams by allowing the chassis to bend at angles, reshaping the chassis to match changes in surface topography.
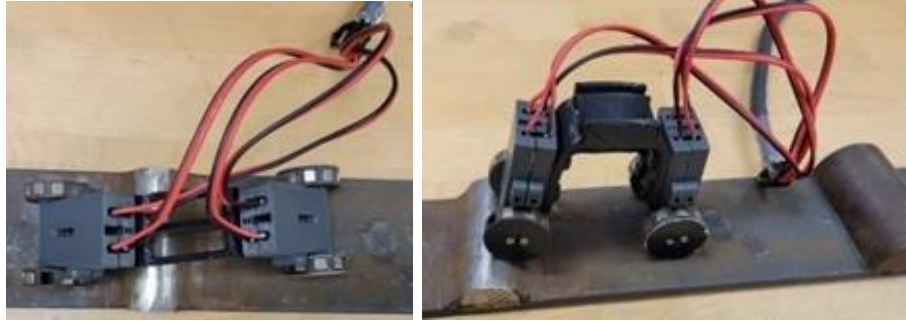
Figure 19. Compliant UT rover weld seam test.

FIU's efforts were also dedicated to exploring and adapting machine vision software to guide the ultrasonic (UT) sensor rover. Extracting surfaces using machine vision techniques can provide the inspection tool with semi-autonomous navigation capabilities and accurate identification of ideal sampling locations for probe ultrasound measurement and create a baseline for future comparison. Identifying the channel features allows the rover to perceive spaces from a single monocular camera. The extracted features fused with inertial measurement unit (IMU) attitude estimations can potentially generate a tridimensional map of inspected areas, visualizing UT sensor measurement locations and other critical features within the refractory channels. Figure 20 shows an initial attempt to detect the channel edges using a classical computer vision algorithm.

Figure 20. Channel edge detection on FIU's full-scale mockup channel.

In addition, methods to extract environment features and classifying surfaces were also explored to segment boundary regions, such as channel walls and tank liners. Figure 21 shows results from a dense optical flow method, a more robust technique to detect motion compare to edged detection features.

Figure 21. Dense optical flow (left) and canny filter edge detection (right) methods.

Subtask 18.2.3: Testing of SST Crawler

WRPS has requested FIU to modify a previously developed pipe crawler for scanning gamma radiation on the lateral lines underneath the SSTs and provide an indirect inspection solution for leak detection and waste plume movement.

In this performance period, FIU continued the refinement of the crawler and supported the deployment of the unit at the Cold Test Facility at Hanford. In addition, FIU automated the system so that it can be used to navigate through multiple lines autonomously. In this capacity, it will be used as a surveillance tool to monitor radiation through multiple lateral lines.

Figure 22 shows a conceptual design of the complete system, including the gamma scanner and the camera front module. FIU's pipe crawler's overall retrofit included: a) pipe crawler modification and improvements, b) sensor module development, c) mockup gamma radiation sensor integration, d) tether assembly, e) cable management automation, f) controls and supporting software framework implementation, g) operator interface development, h) in-house tests, and i) Cold Test Facility deployment at Hanford.

Figure 22. Lateral gamma scanner's delivery pipe crawler.

Pipe Crawler Modification and Improvements

The modules' curved guides were streamlined to reduce further friction and correct failures observed during initial testing. Figure 23 (left) shows a functional prototype of the pipe crawler that was rigorously tested to evaluate the unit's behavior in realistic conditions. Improvements included the addition of rolling bearings to the guides. This helped in significantly reducing contact friction. Improved guides are shown in Figure 23 (right).

Figure 23. Current pipe crawler prototype (left) & improved guides (right).

The inter-module flexible connections and module guides' design were also revisited, as shown in Figure 24. The redesigned links use a monolithic 3D printed compliant part securely fastened to the modules' flanges, eliminating inconsistencies in the previous adhesive joint. The suspension guides were shortened and strengthened solving reported structural issues without compromising functionality.

Figure 24. 3D printed inter-module flexible connection (left) and strengthened guides (right).

Figure 25 shows the redesigned brake mechanism in the gripper modules, improving anchoring strength by shortening the arm's length, and eliminating the articulating pads at the end for better force transfer. A higher gripper strength sustains higher carrying payloads during the peristaltic motion, which is crucial for deploying the gamma sensory modules.

Figure 25. Original (left) and redesigned gripper arms (center and left).

In parallel, the gripper modules were further reengineered to maximize the gripping forces exerted by the pneumatic cylinder. As shown in Figure 26, the alternative design minimizes moving parts, replacing the original sliding mechanism with fiber-reinforced rubber strips. The strips can provide a larger contact area and more potent friction forces. However, further tests and simulations are being performed to optimize and validate the design.
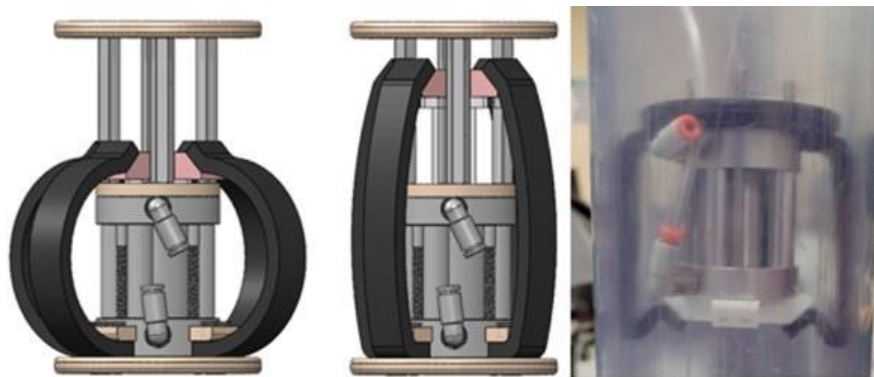
Figure 26. Conceptual gripper design and prototype testing.

The grippers using rubber strips have higher gripping forces compared to the articulated rigid arms, increasing by approximately 10 pounds. The improved design also increases the space available for routing pneumatic tubing, data lines, and integrating additional sensory.

Figure 27 shows the improved rubber strip gripper prototype and a preliminary effort to optimize its gripping force utilizing finite element analysis (FEA).
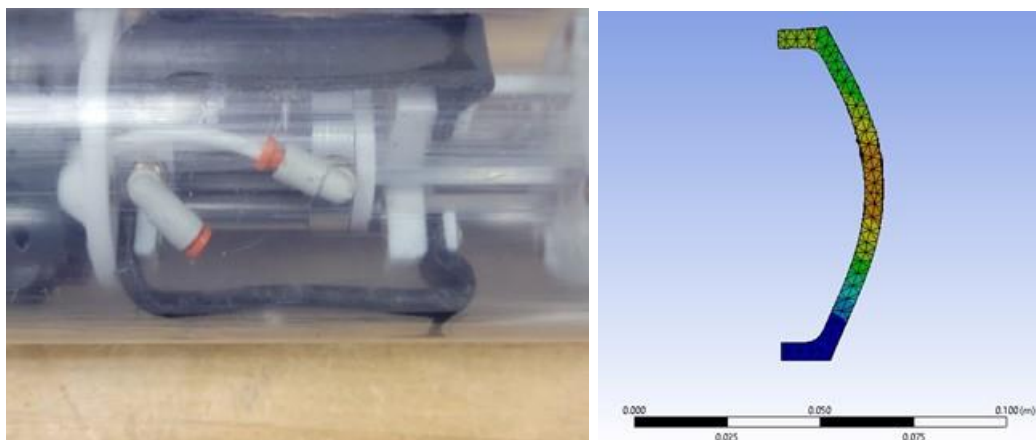
Figure 27. Rubber strip compression and sample FEA analysis.

Efforts were also geared towards literature review, educating the DOE Fellow involved in the crawler's design on modern simulation tools and existing modeling capabilities for non-linear hyperplastic materials. The Fellow focused on modeling the gripper module and its constraints. The process involves an analytical breakdown of the contact between the rubber surface and the pipe wall to better understand the stresses.

Figure 28 shows FIU's final prototypes, the original crawler and the slightly modified prototype with larger actuators. The two versions were deployed at Hanford's Cold Test Facility.

Figure 28. New crawler prototype shown with the older version.

Sensor Module Development

An electronics module, shown in Figure 29, was also developed and is located at the front end of the pipe crawler. It currently houses a range finder, single board computer, wide-angle camera, and a female Ethernet port. The single board computer is utilized to transfer the live video feed, as well as an interface for potential additional sensing equipment. The module itself has guides surrounding it to provide video and images from the center of the pipe it is resting in.

Figure 29. Electronics module with a forward-facing camera and range finder.

Figure 30 shows a successful test of the front module streaming camera video and LiDAR distance measurements simultaneously.
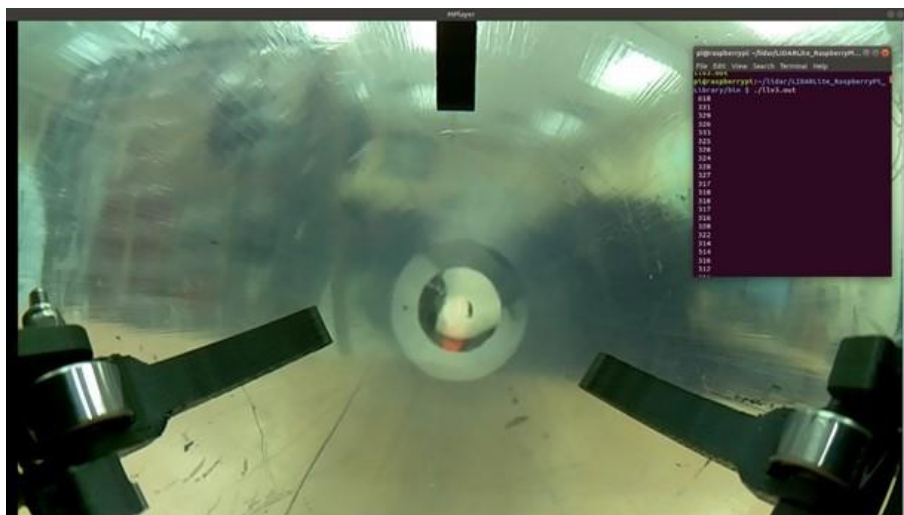
Figure 30. Front module test.

Figure 31 shows the front module's PCB. The board's main improvements include thicker tracks to increase the embedded computing power delivered and light controls, allowing dimming and visual debugging by establishing blinking patterns.
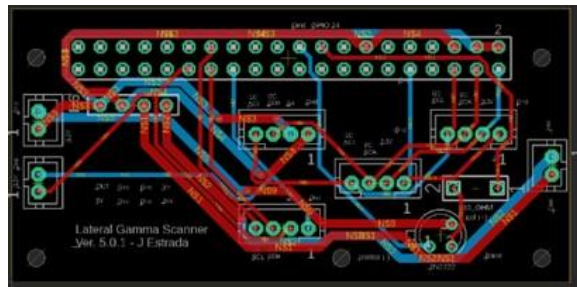
Figure 31. Front module redesigned PCB.

Figure 32 shows the updated schematic, including the transistor in series after the LEDs to mitigate power losses.
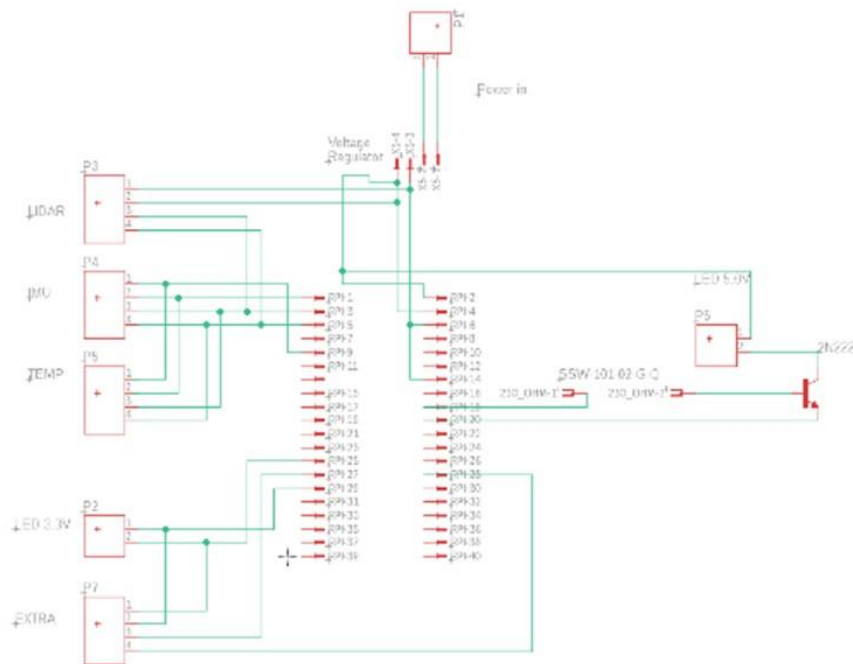
Figure 32. Front module redesigned PCB schematic.

Mockup Gamma Radiation Sensor Integration

Figure 33 shows the mockup sensor built according to WRPS's guidance to simulate the payload weight and shape during mockup tests and deployments.

Figure 33. Mockup sensor payload.

The mockup sensory package has 15" length, 1.9" diameter, and 3 lbs per module in a total of 9 lbs consisting of 3 modules.

Figure 34 shows the FIU Lateral Gamma Scanner crawler, including the retrofitted delivery pipe crawler, the mockup sensor, and frontal camera module in a total length of approximately 8 feet.

Figure 34. FIU's Lateral Gamma Scanner.

Tether Assembly

The quick-disconnect module shown in Figure 35 was designed to facilitate disconnecting the pipe crawler from the tether. This allows the team to efficiently make changes to the crawler without having to dismantle the tether. The tether "egg" houses an RJ45 slot, six push-to-connect straight pneumatic fittings, and a slot for a steel rope. The main housing (large cylinder) seals the components with a lid secured by 4 screws along the circumference. Tubes and wiring remain within the crawler to avoid removing each pneumatic fitting. The steel rope is secured with two loops, the tether and the crawler's, joined with a shorter length than other cables to ensure tension is only on the steel cable.

Figure 35. Tether "egg" for quick detachment.

Figure 36 shows the tether assembly with six pneumatic lines, an Ethernet cable, and a retrieval steel wire. The tether was sleeved using a polyester fray-resistant expandable sleeve.

Figure 36. Tether assembly.

Figure 37 shows the 240-foot assembled tether, containing six pneumatic lines for locomotion, an Ethernet cable for communication and electric power, and a steel cable for retrieval.

Figure 37. LGS tether.

Cable Management Automation

Figure 38 shows a motorized tether reel automated to deploy the inspection tool.

Figure 38. Motorized cable reel.

Figure 39 shows the integration, disassembly, drilling and reassembly of a slipring to provide an Ethernet connection to the reel drum, consequently powering the pipe crawler during the deployment.

Figure 39. Ethernet slip-ring integration.

Figure 40 shows the LGS cable automated management systems final prototype developed at FIU.
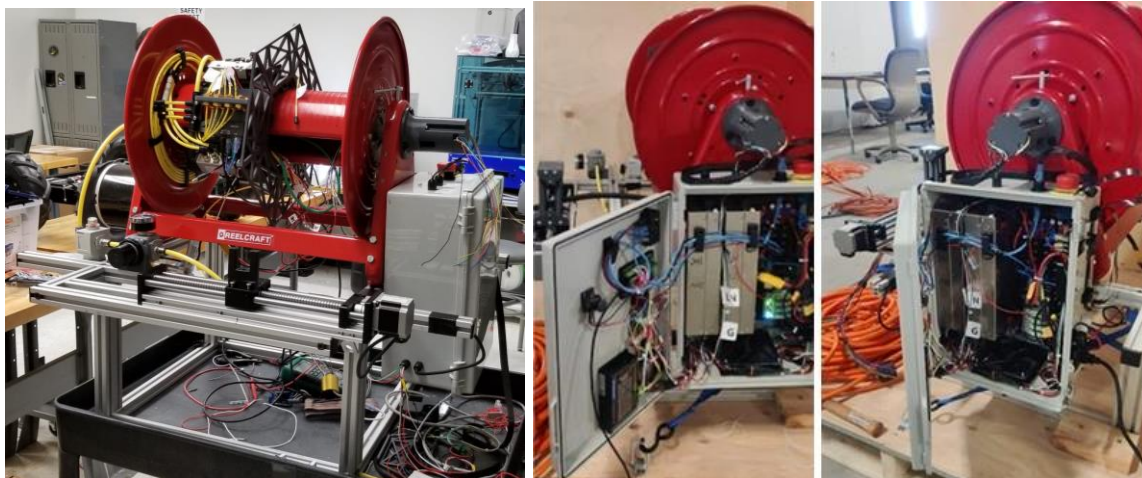
Figure 40. LGS automated cable management.

Controls and Supporting Software Framework

The controls and supporting software framework for the Lateral Gamma Sensor (LGS) was developed using the Robot Operational System (ROS2). Figure 41 shows the current ROS2 node structure, where two main servers respond to the action requests of controlling the Pipe Crawler and the Reel.
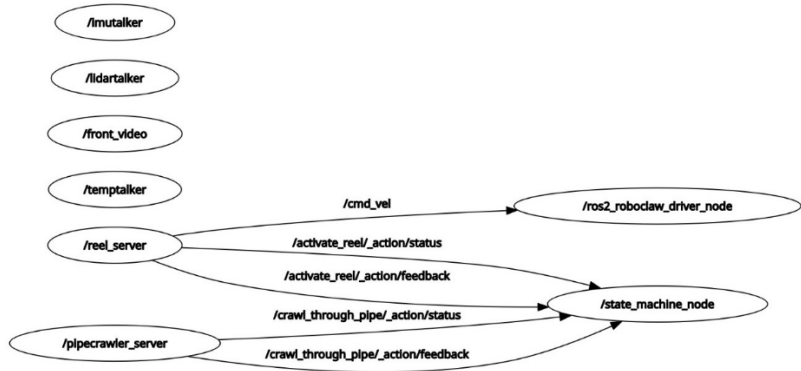
Figure 41. ROS2 node graph for LGS System

The implemented controls use a state machine node to coordinate the crawler movement, the reel rotation, and consequently the winder coiling. In addition, the pre-existing nodes for the LiDAR and the Inertial Measurement Unit (IMU) sensor nodes were reimplemented as ROS2 services answering asynchronous requests instead of the previously published information constantly under a fixed rate.

Figure 42 shows a graph depicting the current node structure, where two main servers, */reel_server* and */pipecrawler_server,* are deployed in the embedded computers that connect to the Solenoid Valves and the Reel's motor controller respectively. These respond to the action requests submitted by the state machine node. This node is the central point of synchronization and control of the system. The node interacts with the sensor nodes deployed in the front module to probe the sensors that determine the state transitions.
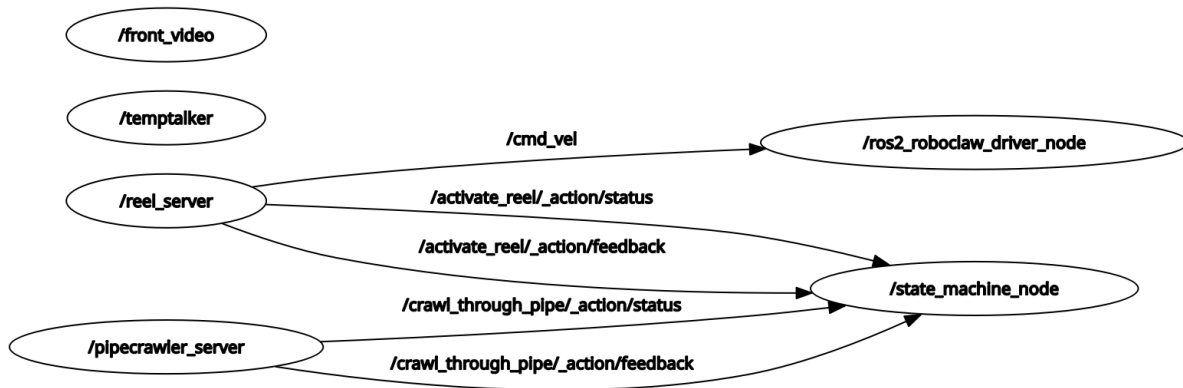
Figure 42. ROS2 Node Graph.

Figure 43 shows a representative section of the flowchart diagram of the state machine program, which handles the transitions between the operational states of the lateral inspection. Each state represents a specific position of the pipe crawler during the operation. The transitions between states have specific conditional checks to control the different functions of the crawler and to perform specific state-related tasks. The state machine operation was selected for the lateral inspection operation since the machine can be triggered to transition to a failure state or to a premature retrieval state in case of unexpected obstacles or system malfunctions.
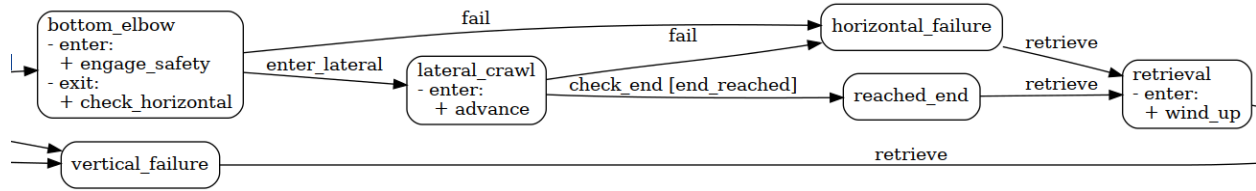
Figure 43. State Machine Diagram (section).

The LGS uses a robust localization technique fusing many sources of odometry. Figure 44 shows a nine-degrees-of-freedom inertial measurement unit (IMU) mounted in the front module. The IMU has been used exclusively for attitude estimation, probing the front module's pitch angle to determine transitions between vertical and horizontal sections during lateral scans.

Figure 44 . BN055 IMU in front module.

The inspection tool estimates position by counting forwarding crawl commands and measuring distances to the end of the lateral unit using the front lidar. The LGS team intends to improve the current localization system by fusing IMU inertial and tether length estimations. The implemented IMU inertial estimation algorithm integrates instantaneous acceleration and angular velocities over time to estimate longitudinal changes in position during forwarding crawling movements. The final position estimate uses an extended Kalman filter estate estimator to fuse all sources of odometry.

The team has also experimented with monocular visual odometry. Video images from the crawler's frontal camera are input into the ORB-Slam package, which tracks visual features in the pipe surfaces as another potential source of position estimation**.**

Operator Interface Development

A custom graphical user interface (GUI) for operating the Lateral Gamma Scanner was internally developed at FIU. The designed GUI is more operator-friendly than the current command line interface, remotely launching multiple robotic operating system (ROS) nodes that synchronize the crawler, cable reel movements, and sensory acquisition during inspections. Site operators will use a touchscreen embedded in the control box to command the tool, visualizing, recording, and playing back all streamed sensors.

Figure 45 shows a preliminary version of the interface running mainly two video views showing the frontal and rear cameras simultaneously and a right toolbar including system controls. The

implemented user interface has also been customized to other inspection tools developed at FIU, such as the magnetic miniature rover.
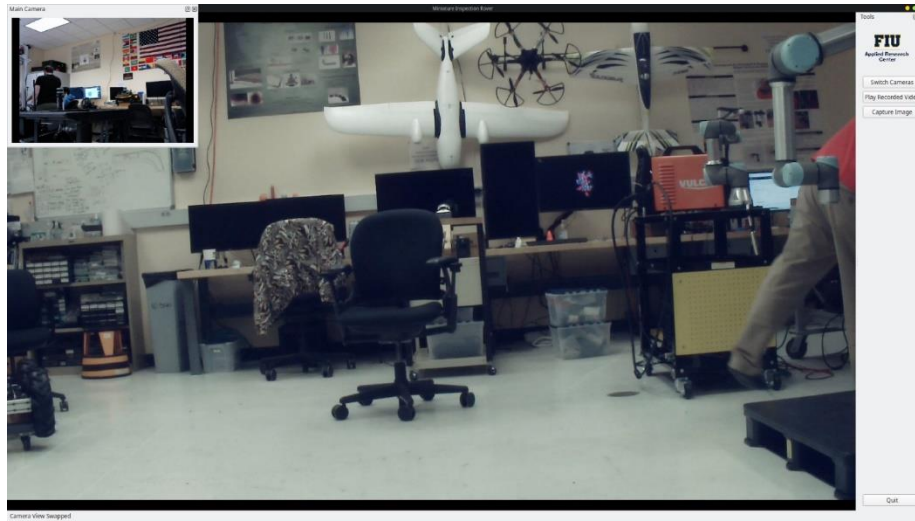
Figure 45. LGS' Graphical User Interface.

The LGS team will continue further improving the graphical user interface, enhancing controls, and including visual indicators displaying multiple system statuses, such as distances, inclinations, speeds, pneumatic pressures, supply voltages, power consumption, among other relevant inspection parameters.

In-house Tests

The LGS efforts performed rigorous testing to evaluate the behavior of the crawler in realistic conditions. Testing combined several different scenarios ranging from jammed guide components to adverse weather.

Figure 46 shows the pipe crawler successfully being tested in a bench-scale mockup. The mockup was originally designed to test other pipe crawlers developed at FIU.
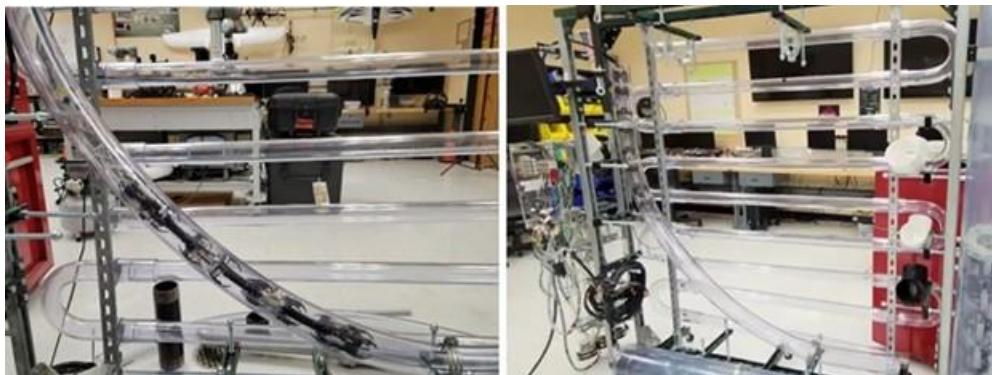
Figure 46. Pipe crawler bench-scale testing.

Figure 47 shows a portable control box retrofitted to test the pipe crawler, also field deployment and quick troubleshooting.

Figure 47. Portable control box.

Figure 48 shows a preliminary in-house test individually testing the mechanical performance of the pipe crawler and the cable management.
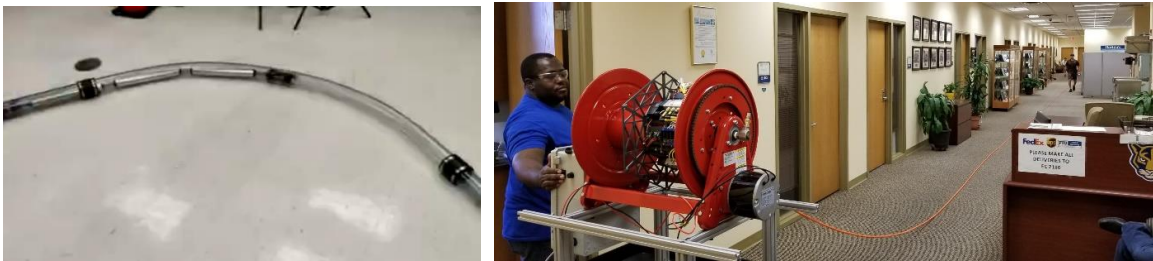
Figure 48. Pipe crawler and tether reel in-house tests.

Figure 49 shows preliminary system integration tests using an extended elbow and 100 ft of straight pipe. The figure also shows the crawler's three sections that emulate the radiation sensors. The crawler successfully navigated through the swept elbow and through the straight sections.

Figure 49. Length of straight section for the in-house testing.

The reel was automated to feed out or retract the tether at a rate that can be controlled by the operator. Figure 50 shows the automated reel during the in-house testing.
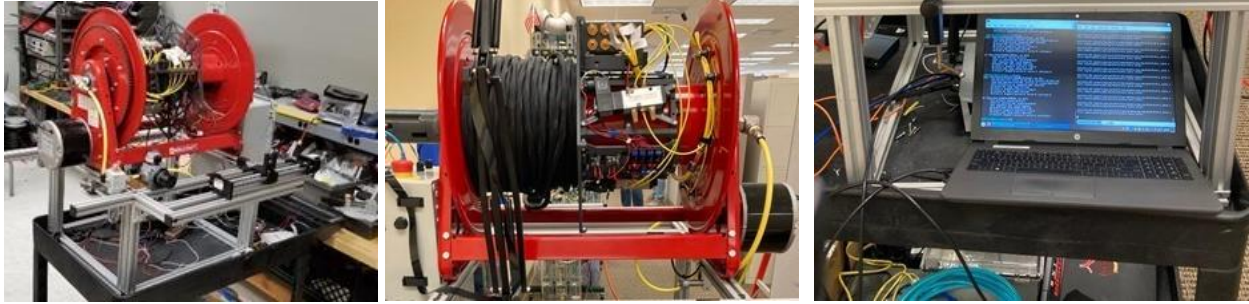
Figure 50. Automated reel during in-house testing.

Cold Test Facility Deployment at Hanford

In March 2022, the LGS crawler was successfully deployed at WRPS's Cold Test Facility in Hanford, Washington. Figure **51** shows test images from the facility.

Figure 51. Cold Test Facility deployment.

The deployment was a combined effort involving Florida International University (FIU), Washington State University (WSU), and WRPS Chief Technology Office (CTO), as illustrated in Figure **52**.

Figure 52. Deployment team.

The tests simulated FIU's peristaltic crawler carrying gamma sensor modules being deployed through a single shell tank's lateral. The sensor payload is a mockup based on a sensor deployed in 2005. The weight and size of the payload were coordinated with Hanford's engineers and scientists. The deployment tested the crawler's mobility throughout bends and the functionality of the cable management developed by WSU, as well as the overall accuracy of the system.

Figure **53** shows the two crawler versions designed at FIU and tested at CTF. The second unit is an improved generation that uses longer actuators for increased displacement along the pipe, decreasing the time required to traverse the laterals beneath SSTs. The gripper modules have also been modified to use rubber strips instead of the locking mechanism arms fixed to the actuator typical in previous generations.

Figure 53. Initially designed gripper module (left) and modified rubber strips (right).

The overall pipe crawler design was reassessed, and changes were incorporated to improve key structural components damaged during the CTF tests. Hinge pins in several flanges were secured by locking screws to prevent potential falls, and heat-sets loosened under higher loads were replaced by flanged ones with larger threads. The cable management in the extender modules was also improved to prevent coiling around the actuators and potential pinching of pneumatic lines.

Textured 3D printed flexible padding was added to the grippers to increase surface friction. The pads were also rounded to fit the pipe wall curvature better.

In June 2022, the LGS system was successfully redeployed at WRPS's Cold Test Facility (CTF) in Hanford during the DOE Fellow's summer internship. The second deployment demonstrated the proof of concept of an automated leak detection system, proposing daily automated gamma inspection of a single-shell tank's laterals without operator intervention. The deployment obtained additional feedback from Hanford Site engineers and demonstrated safe emergency retrieval in case of unexpected inspection failure.

As pictured in Figure 54 efforts were also dedicated to finalizing the feedback control framework that synchronizes the Pipe Crawler and Reel System, which includes: a) finalizing control nodes for reel and pipe crawler control, b) tuning synchronization of the reel, crawler, and winder, and c) testing pipe crawling through mockups using ROS action servers.

Figure 54. DOE Fellow, Josue Estrada, interning at WRPS performing robotic crawler and reel synchronization test at CTF in Hanford.

Subtask 18.2.4: 6-inch Crawler Development

Analyses of the secondary liners in the annulus of DSTs at Hanford have shown unexpected thinning. It is unclear how far the thinning extends toward the center of the tank, and inspection tools are needed to aid in assessing the secondary liners. An inspection tool is needed that can traverse through the drain pit lines to reach the drain pit slots in the tank foundation. Previous inspection tools deployed in the drain lines did not complete the goal of getting to the central plenum due to unforeseen conditions in the pipeline presenting sediments, corrosion, and buildup.

FIU has developed a marsupial-type inspection system that combines a mother pipe crawler that traverses the drain pit lines and delivers a miniature child rover that will inspect the secondary liner in the drain pit slots area of the tank foundation. The child rover can also be fitted with a UT sensor for point inspections.

A prototype for the housing and transport module of the marsupial inspection system was designed. This prototype that includes the deployable and retractable ramp allows the instrumentation rover to access the floor of the DST drain slots. The current design uses a lead screw to carry the ramp assembly forward and back, and a series of guide-pins and springs that let the ramp deploy, retract, and close the first section of the ramp as a lid, a concept shown in Figure **55**.
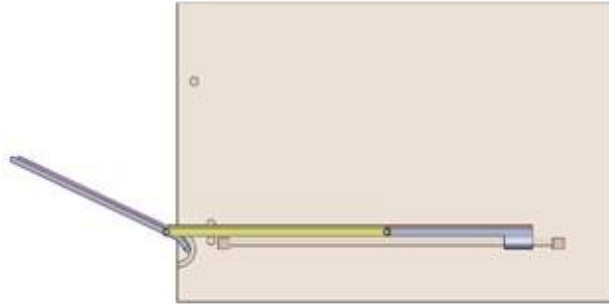
Figure 55. Conceptual design of deployable ramp.

Figure 56 shows the CAD model of the marsupial system including the housing module and the instrumentation rover. The housing module shown in the figure includes the 4 bottom modular tracks that will transport it through the 6-in diameter pipe.

Figure 56. Model of rover in housing module with deployable ramp.

Figure 57 shows the current working prototype with a deployable and retractable ramp. This prototype allows the rover to drive out but requires further work on collecting the rover back in.
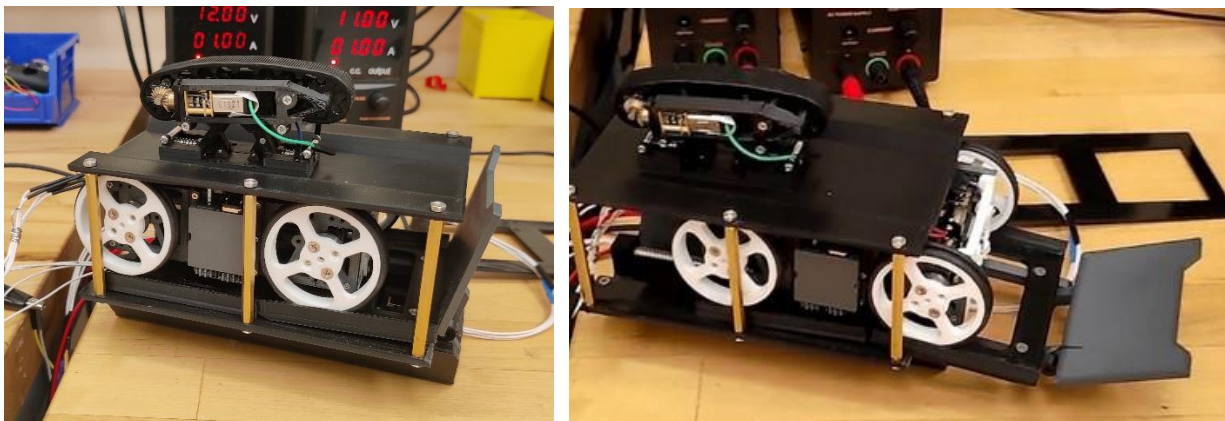
Figure 57. Housing module and ramp prototype

As shown in Figure **58**, the pipe crawler's additional module transports the marsupial inspection system using a deployable and retractable ramp that allows the instrumentation rover to access the floor of the DST drain slots. The tests revealed a few issues that have been addressed in the design.
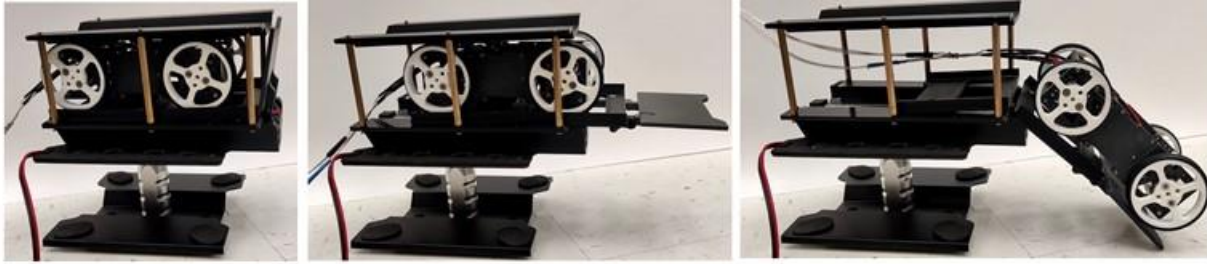
Figure 58. Housing module prototype with ramp.

The main challenge was the restricted space for the rover inside the housing module. The lateral guides of the ramp fit the rover; however, the wheels' rubber interferes with the module's frame. Figure **59** shows a redesigned frame with additional space to address the issue.
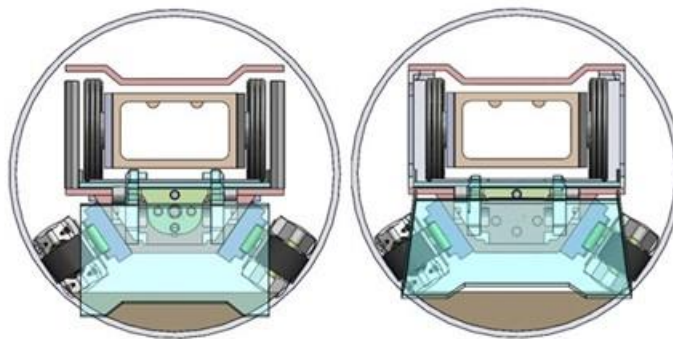
Figure 59. Previous (left) and current (right) module design.

Another improvement addresses the instrumentation rover driving back up the ramp and into the housing module. Illustrated in **Figure 60**, the current design includes a bottom ramp section with a tapered profile to funnel the rover entering the ramp in misaligning maneuvers. Also shown in the same figure is an optical limit switch that has been added to control the deployment and retraction.
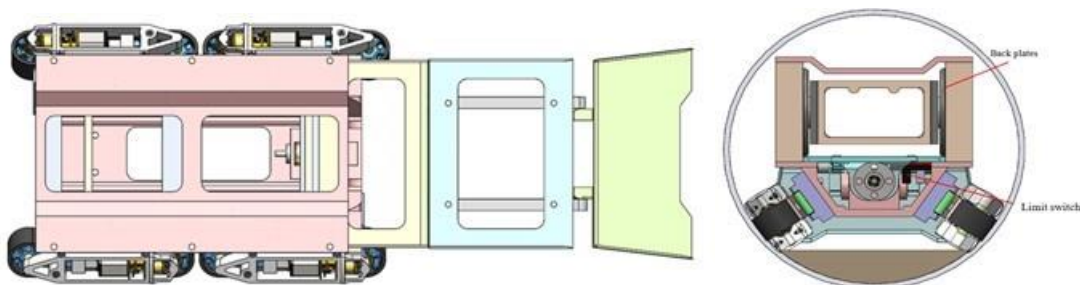
Figure 60. Housing module top view (left) and rear view with limit switch (right).

In coordination with WRPS engineers, the development efforts on the marsupial-type inspection system were reassigned to the SST task.

Subtask 18.2: Conclusions

The miniature magnetic rover subtask has been successfully completed and the technology transferred to the DOE Hanford Site. WRPS requested five more units from FIU, as well as

enhancement of the current mini rover, integrating sampling tools for material retrieval under the DSTs.

Significant improvements were made to the UT sensor rover including the incorporation of a cleaning mechanism that can remove debris from surfaces prior to measurements and means to apply couplant allowing more accurate measurements. The system was capable of navigating in the mockup at FIU and could provide reliable measurements for the thickness of the tank floors. However, in coordination with WRPS engineers, the design efforts on the UT sensor inspection rover have been reassigned to the miniature rover sampling tool development.

The Lateral Gamma Scanner was successfully demonstrated and tested at Hanford's Cold Test Facility. The overall improvements in functionality, automation and robustness of the inspection tool will continue, the integration of a gamma radiation sensor provided by WRPS will be potentially completed, and the system deployed at Hanford's tank farm.

As coordinated with WRPS engineers, the DST secondary liner's marsupial inspection system design effort will be halted, and the effort reassigned to other high priority deployments.

Subtask 18.2: References

1. Randall, R. and Price, R. K., 2006, Gamma Surveys of the Single-Shell Tank Lateral for A and SX Tank Farms, CH2M Hill, RPP-RPT-27605, Rev. 0.
2. Randall, R. and Price, R. K., 2006, Gamma Surveys of the Single-Shell Tank Lateral for A and SX Tank Farms, CH2M Hill, RPP-RPT-27605, Rev. 0.
3. Engeman, J.K., Girardot, C.L., Harlow, D.G., Rosenkrance, C.L. , 2012, Tank 241-AY-102 Leak Assessment Report, Washington River Protection Solutions, RPP-ASMT-53793, Rev.

Subtask 18.3: Development of a Coating Deployment Platform for the H-Canyon Exhaust Tunnel

Subtask 18.3: Introduction

The H-canyon is the only remaining chemical processing facility in America capable of reprocessing plutonium, highly enriched uranium and other radioactive materials [1]. The exhaust air flow from the H-canyon chemical processing areas and HB-line are transported through the H-Canyon Exhaust (HCAEX) tunnel, where radioactive contamination is removed. Robotic inspections of the tunnel have revealed significant ongoing degradation of the reinforced concrete structure that was associated with acid attack. The degradation observed could compromise the mechanical strength of the structure. Hence, the search for solutions to mitigate and prevent further degradation is necessary [2-3]. The application of a protective coating on the degraded tunnel walls could mitigate and prevent further degradation, which constitutes the main goal of this investigation. This research effort has been divided into two phases: 1) Development and evaluation of aged concrete under accelerated aging conditions and 2) Evaluation of potential coatings applied on aged and non-aged concrete under simulated aggressive conditions.

In the preliminary stage of the investigation, a comprehensive literature review was performed and major findings included: 1) the characterization of the tunnel degradation conditions, 2) the identification of the chemical attack and erosion as the primary degradation mechanisms affecting

the tunnel concrete walls, 3) the identification of the acid-type immersion tests as a well-known method for evaluating the materials' resistance to acid attack and, 4) the preliminary selection of potential coatings for aggressive environments similar to the tunnel [3].

Lessons learned and research findings of the initial testing of concrete in acid solutions supported the development and ongoing execution of a comprehensive test plan that will be presented in this report. The test plan execution is an ongoing task allowing the development and evaluation of aged concrete surfaces, with 1) protruded aggregates, 2) exposed steel rebar, and 3) chemically damaged, similar to the tunnel walls after more than 60 years of operation. The degraded (aged) concrete surfaces were developed through various accelerated aging conditions including the effect of some variables such as acid concentration, erosion, mode of action of the aggressive agent, and the presence of steel rebar [3]. Finally, the developed aged concrete surfaces will be used as the substrate for the evaluation of potential coatings in a further stage of the investigation. Because this is an ongoing investigation, preliminary results of the accelerated aging of concrete specimens will be presented in this report.

Due to the hostile environment of the HCAEX tunnel, the ability to enter the tunnel and perform any type of investigative, or in this case damage mitigation to the concrete walls, have been restricted to the use of robotic platforms equipped with the tools necessary to accomplish said goals. The robotic platform would need to work in tandem with another larger ground platform capable of traversing the difficult terrain of the tunnel. The ground platform would need to deploy the secondary platform onto the concrete walls to apply a down selected coating.

The secondary robotic platform will need to be capable of traversing the HCAEX tunnel concrete walls in a manner that does not further damage the surface of the walls and allows accurate positioning of the platform to apply the coating. A literature review regarding the different methods available that would allow a mobile platform to maintain contact with the walls, regardless of the platform's orientation, will be highlighted in this report.

After developing and testing a single fan-based platform, which creates the appropriate adhesion mechanism, the results obtained from constructing a multi-fan omnidirectional platform will be detailed in this report. The goal of the report will also be to show the viability of the platform as an option to a unit capable of traversing a concrete surface without introducing further damage to the wall's surface and at the same time, maneuvering across the surface to reach a desired location when tele-operated.

Subtask 18.3: Objectives

The primary objective is to develop a robotic mobile platform capable of traversing vertical walls with varying surface conditions and applying a coating to the walls with the aim of preventing further surface degradation inside the HCAEX tunnel. The aim is to develop a robotic mobile platform capable of traversing vertical walls with varying surface conditions using a thrust based adhesion mechanism [4,5].

A scaled mockup concrete wall will be constructed using the information from Savannah River Site engineers, and the platform will be evaluated for its ability to maneuver along walls with varying surface conditions. The performance of the platform will also be quantified and used as a baseline to compare to future iterations of the platform as improvements are made during the project cycle.

The platform will be equipped with a coating application system which will be developed for the purpose of applying a selected coating to the concrete walls of the HCAEX tunnel. The application system will be designed to be modular in nature so that it can be incorporated into mobile platforms of varying sizes and configurations.

Subtask 18.3.1: Improvement of Mobile Platform Efficiency

Subtask 18.3.1: Methodology

A platform that included two 90mm electronic ducted fans (EDF) was developed and evaluated for its ability to adhere and traverse along a concrete surface. The dual EDF unit, depicted below in Figure 61, was tested on a small-scale wall mockup with varying surface conditions. The design for the vector thrust module is being refined FEA simulation and topological optimization to reduce the overall mass of the unit and reinforcement areas for increased robustness.
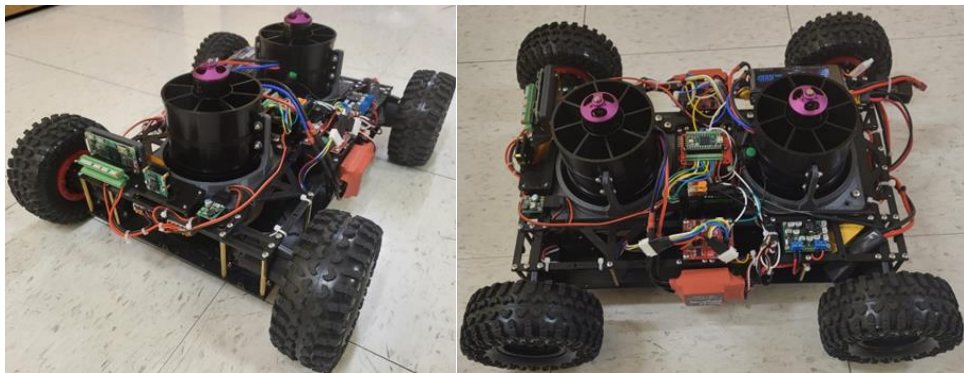
Figure 61. Dual EDF unit.

Next, a supportive arm structure, Figure 62, was prototyped and assembled with the idea of using it to compensate for the negative effects of the tether line used for communication and power on the mobile platform and the weight of the coating transfer lines. The control for the supportive arm structure was improved by adding the ability to control the location of the end effector via an analog joystick. All the components necessary for this basic operation have been packaged into a single module which travels along with the arm for easy setup and testing. The implementation of the PID controller for allowing smooth and accurate positioning of the end effector of the supportive arm structure was also implemented.
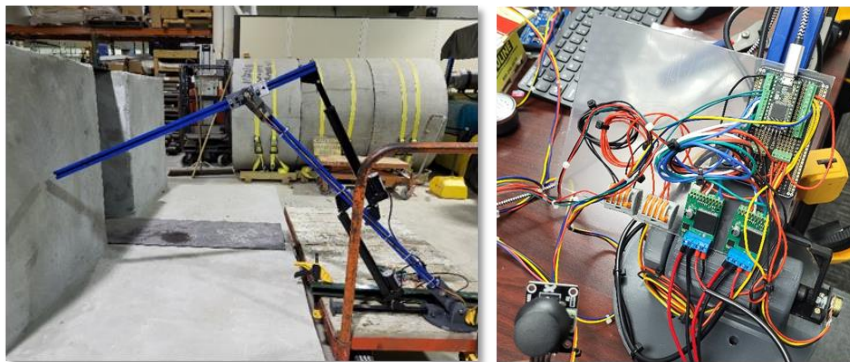
Figure 62. Supportive arm structure.

As a result of the construction of the supportive arm unit, the next task was the development of a gimbal setup which will be used to control the thrust vector generated by the EDF units on the platform. A basic CAD model, Figure 63, was developed with individual components 3D printed using ABS, to confirm that the geometric restrictions designed into the unit did not compromise the maneuverability of the gimbal setup.

Figure 63. Basic CAD model with 3D printed components..

Finally, a sand ingestion test was performed to determine the effects of debris entering the ingestion portion of the EDF unit. The experimental setup, Figure 64, included a chamber designed to direct the inlet flow of air towards a secondary EDF fan which will act as a proxy to the fan on the mobile platform. The ingestion unit was constructed to aid in performing ingestion tests and gather data and develop a model which will be used to investigate the areas of blade degradation, thrust generation reduction via material in flow and filtering. An IMU (inertial measurement unit), load cell, tachometer (to measure the fan speed) and current sensor. All of the sensors are being monitored via a microcontroller and the data generated is being saved as a text file to be post processed.
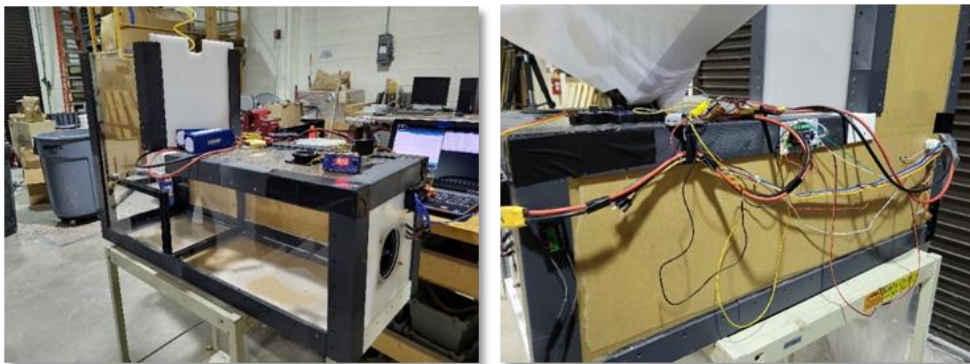
Figure 64. Sand ingestion setup with integrated sensors.

Subtask 18.3.1: Results and Discussion

The dual-fan system, Figure 61, weighs 2.2 kg and can generate a combined thrust force of 7.6kg when each EDF unit is operating at the maximum input voltage of 25.2V. As a result of the power

consumption of each of the EDF units, it was decided to provide a separate power source for each unit to operate.

The supportive arm unit, Figure 62 above, was tested by attaching a total of 30lbs to the end of the second link which it successfully lifted. The control parameters for the PID controller were modified multiple times in order to have the arm behave in a smooth manner when transitioning the end effector from one point to the next. The goal here was to also minimize the jerking action of the arm when sudden changes were made to the end effector destination point.

The initial experimental setup for the debris ingestion test was simplified to varying the input signal to the ESC and monitor the thrust generated using the load sensor attached to the frame of the secondary EDF unit. Figure 65 shows the graph that depicts the response of the EDF unit to the frequency increase. Figure 66 also shows the results obtained from introducing the fine grain sand into the air stream of the secondary fan at a constant mass flow rate of 7.15g/s. From the results, it was determined due to the small grain size of the sand that it did not affect the flow rate to a point of minimizing the generated thrust.
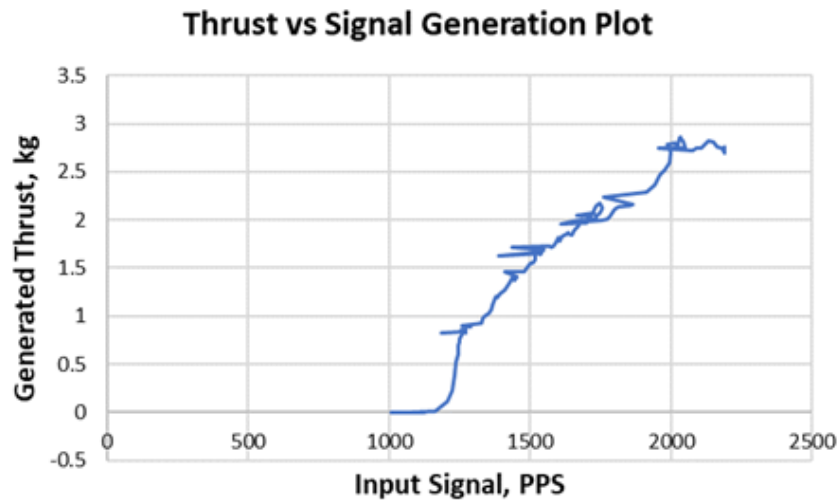
Figure 65. Graph of thrust force generated with no debris.
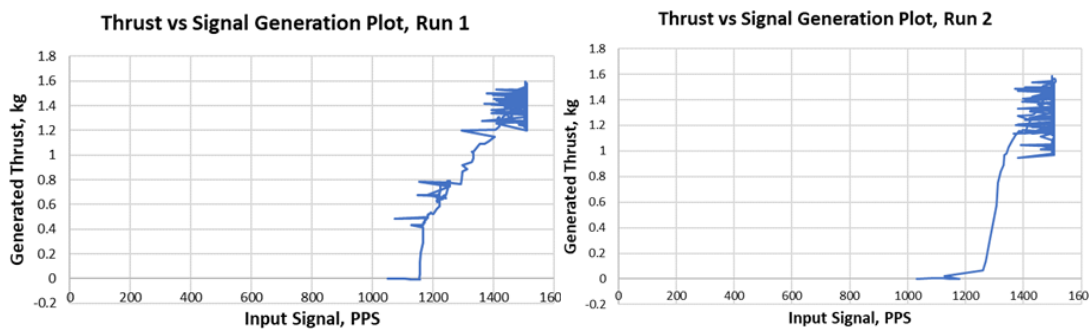
Figure 66. Graph, of two separate runs, of thrust force generated with debris.

Subtask 18.3.1: Conclusions

Different technologies were developed in order to improve the efficiency and performance of the EDF based platform. Also, other tools to deal with the problems introduced by the coating application and H-Canyon environment were prototyped and tested. Specifically, a dual based EDF unit was prototyped and assembled since it is more stable in terms of thrust force distribution along the chassis and wheels of the platform. Next, a supportive unit was constructed with the goal of addressing the problems associated with the forces generated by the surface preparation process, tether line for communication and power and the weight of the coating compound transfer lines. The supportive unit was assembled along with the controls, where it was successfully tested for movement with a load attached to the "wrist" section. Finally, a gimble setup for controlling the thrust vector force generated by the EDF unit was developed to take advantage of the forces that would aid in extending the longevity of the geared DC motors.

Subtask 18.3.1: References

1. Gilliam, Bob J., Ray, J., and Giddings, B. "Inspection and assessment of the H-Canyon ventilation system at The Savannah River Site". Phoenix, Arizona, 2015. Waste Management Conference.
2. Staff Report, Defense nuclear facilities safety board. "H-Canyon exhaust tunnel fragility analysis input and assumptions". 2018.
3. Echeverria, M., Nunez Abreu, A., Lagos, L., McDaniel, D. "Aging of concrete for the evaluation of repair materials to protect the HCAEX tunnel at Savannah River". Waste Management 2020 Conference, Phoenix, AZ, March 2020. (Best Poster of Track). Paper # 20301
4. Telusma, M., Natividad, J., Lagos, L., McDaniel, D. "Development of an Omnidirectional Wall Crawling Mobile Platform, Designed to Aid in the Repair of H-Canyon's Concrete Walls". Waste Management 2021 Conference, Phoenix, AZ, March 2021.
5. Lattanzi, D., Miller, G. "Review of Robotic Infrastructure Inspection Systems". Journal of Infrastructure Systems Vol. 23, Issue 3 (September 2017)

Subtask 18.3.2: Integration of the Coating Application System

Subtask 18.3.2: Methodology

An experiment was designed to measure the forces generated when a fluid is ejected from a nozzle at specific pressures. The setup included setting up a pressure washer, Figure 67 below, and scale to measure the force generated by the interaction between the fluid and contact surface. Meetings were held with Sherwin Williams, Carboline and Belzona coating companies with the aim of determining what coating system would provide the optimum results.

Figure 67. Electric pressure washer.

The electric pressure is outfitted with multiple nozzles, Figure 68 and Figure 69 below, that differed in nozzle angle which varied from 0 to 25 degrees.
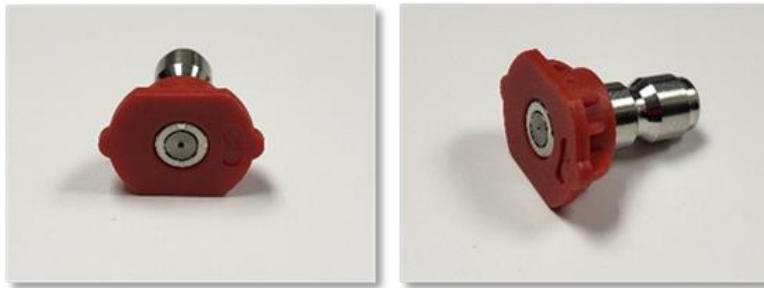
Figure 68. Hight pressure water nozzle with angle of 0 degrees.
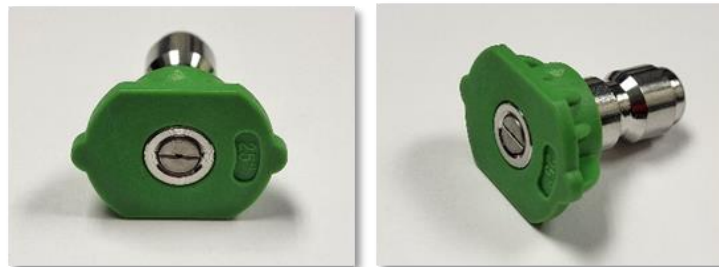
Figure 69. Nozzle with angle of 25 degrees.

Using a weighted scale, the nozzle from the pressure gun was placed six inches above the surface of the scale and measurements were taken in relation to the generated forces because of the fluid interaction and the concrete surface.

Subtask 18.3.2: Results and Discussion

Meetings were held with multiple companies to obtain information regarding the method of application of the coating compounds. Discussion regarding the coating application extended to the type of equipment necessary for the transfer and mixing of the compound mixture. The environment inside the tunnel possesses a unique problem from both logistics and quality of application points of view. Key highlights from the conversation with the companies are outlined below.

Conversations with Sherwin Williams were focused on the selection of the coating and the necessary tests needed to determine the quality of the coating after it has been exposed to a chemical environment similar to that of inside the H-Canyon tunnel. The meetings Carboline and Belzona focused on the selection and application of the coatings along with discussion regarding the type of equipment required to execute and complete a large-scale coating task.

Subtask 18.3.2: Conclusions

In conclusion, results from the experiment to recreate the forces generated during a proxy coating process indicated the platform can create the necessary adherence forces to maintain contact with vertical surfaces. Also, meetings were held with the coating companies to discuss the complexity of the application of the coating product along with the need to redesign the equipment needed to transfer the coating compounds to their destination.

Subtask 18.3.2: References

1. Telusma, M., Natividad, J., Lagos, L., McDaniel, D. " Development of an Omnidirectional Wall Crawling Mobile Platform, Designed to Aid in the Repair of H-Canyon's Concrete Walls". Waste Management 2021 Conference, Phoenix, AZ, March 2021.

Subtask 18.4: Long-Term Surveillance of Nuclear Facilities and Repositories using Mobile Systems

Subtask 18.4: Introduction

Continuous surveillance of nuclear facilities and repositories is a critical element in successfully controlling and understanding radiological environmental impact, planning cleanup efforts, and meeting quality assurance objectives established by the U.S. Department of Energy standards and guidelines. When surveying nuclear facilities and repositories, advanced mobile surveillance systems are safe, efficient, and labor-saving tools that safely deploy state-of-the-art instrumentation without exposing workers to radiation risks. Given the large size of many facilities, coupled with the high cost of radiation sensors and the nature of radiological sources, mobile systems provide a cost-effective solution versus on-site sensor networks or monotonous routine measurements performed by site personnel. In addition, mobile systems deployed in more frequent periodic surveillance missions can provide continuous radiation measurements, simultaneously fusing data from several other embedded sensors, tracking long-term changes in the environment over time, which is needed to assess and document the condition of nuclear facilities during operation, decommissioning, and end state assessments.

In collaboration with Washington River Projection Solution site engineers, this subtask has been investigating robotic platforms and state-of-art field-deployable sensory systems suitable for long term monitoring of nuclear facilities and repositories.

Subtask 18.4: Objectives

This task's primary goal is to investigate fully autonomous off-the-shelf multi-use robotics technologies adequate for surveying nuclear facilities and repositories across the DOE complex. Our investigations pursued the following objectives:

- Develop an agnostic field-deployable sensor package coupled with a robust autonomous radiological survey framework to be deployed at Hanford's mobile platforms during the summer.
- Continue customizing and testing in-house ground and aerial mobile platforms, integrating perception sensors to navigate nuclear facilities, developing digital twins, and fusing data from synthetic gamma measurements, surrounding imagery, and LiDAR mapping.

Subtask 18.4.1: Development, Evaluation and Testing of Agnostic Field Deployable Sensor Packages

This subtask leveraged the implemented framework and lessons learned from surveillance case studies performed during FIU's past performance period to use field sensors coupled with a robust autonomous radiological survey framework to be deployed at Hanford's mobile platforms during the summer.

Subtask 18.4.1: Methodology

Conventional methods of taking radiation measurements by hand within or around the containment areas and analyzing the collected data to obtain the result are ineffective and have put scientists at risk of unnecessary radiation exposure. On the other hand, the current state of autonomy for field-deployed autonomous radiological survey systems is mobile robots with waypoint navigation capabilities. Usually, a scientist selects a series of waypoints on a map, directing the robot to travel autonomously between points. Advanced systems often support obstacle detection and local collision avoidance using LiDAR imagers. However, current surveillance robots in nuclear facilities and repositories do not have a high degree of onboard autonomy to cope with dynamic environments changing over time due to operations, weather events, and site deterioration currently presented in DOE sites.

As exemplified by Figure 70, changes in Hanford's Tank Farm due to retrieval operations [1] and the constant need to manually reconfigure the surveillance mobile platform's mission plan could become a burden to site engineers, which would also be the case in analyzing the captured data over time.

Figure 70. Hanford's Tank Farm retrieval operations in September 2016 (left) and 2018 (right).

The proposed methodology expands traditional autonomous navigation frameworks implementing a novel onboard information-driven planning and control tailored to radiological surveillance of large facilities. The online adaptive planning algorithm [2] takes into account not only navigation

goals and battery constraints, but also includes sensing objectives such as increasing coverage and routing the optimal path that would decrease the uncertainty in the overall radiation map as well as reduce geometric uncertainties in the mapped environment over time. The framework will also implement basic terrain risk-awareness and advanced perception, a crucial issue in taking fully autonomous surveillance systems out of the structured laboratory and mockup environments and deploying them into existing facilities and repositories.

The core areas of development of FIU's Mapping and Robust Localization Framework are:

1) information-driven planning and control in radiological environments,
2) terrain risk awareness in dynamic and unstructured environments, and
3) advanced perception in complex environments.

Information-driven planning and control in radiological environments

The proposed framework uses fully autonomous robots as intelligent agents for sensing locations, actively defining an optimal sequence of consecutive measurements and controlling acquisition parameters of the radiation sensor in real-time (basically dwell time and surface proximity), with the objective of improving the accuracy of the radiation map and addressing common issues with irregularly spaced, noisy, low count data, obstructions, and existing background radiation.

Terrain risk awareness in dynamic and unstructured environments

The proposed framework implements a computer vision module, assisted by a semi-supervised machine learning system that uses video images from surrounding cameras to classify the terrain conditions of the floor segmented by LiDAR data elevation. A convolutional neural network is trained to classify surface types (carpet, vinyl, water, grass), where unknown conditions (low classification probability) are treated as obstacles. Unknown surfaces can be later manually classified by an operator bringing a human in the loop. The terrain awareness improves over time in the proposed framework, keeping the platforms safe in unexpected floor conditions, which is critical in unsupervised robots working in outdoor repositories, especially after weather events.

Advanced perception in complex environments

The proposed framework uses several heterogenous imaging sensors and gamma radiation detectors to construct an immersive environmental map, as illustrated by Figure 71. The framework stores high-resolution maps for digital twin reconstruction and keeps reduced-order ones for navigation and control. The framework also innovates using a robust localization algorithm fusing many sources of odometry (basically ICP, IMU, and visual), suitable in monotonous environments such as hallways and tunnels.
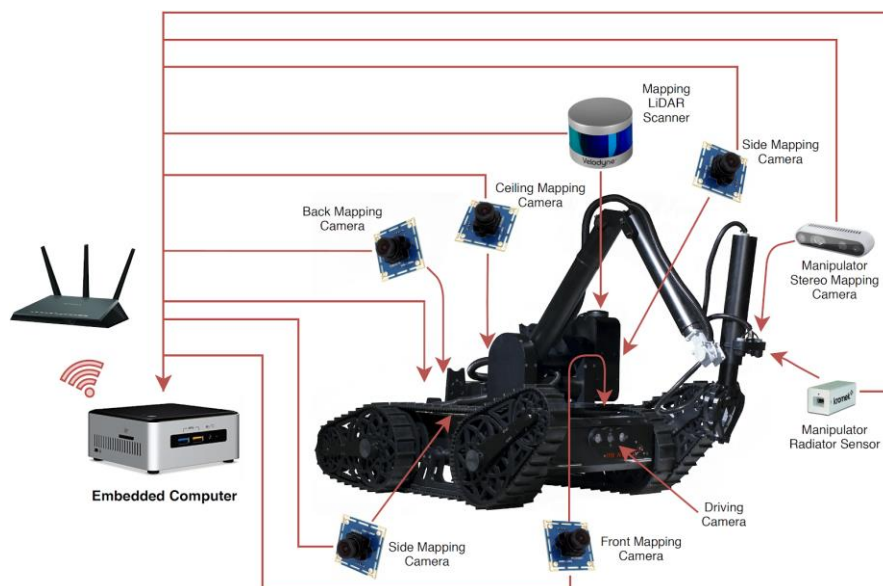
Figure 71. Mobile platform integration.

Robotics Platforms

Figure 72 shows the handheld, ground, and aerial mobile platforms used in our in-house tests. The platforms have been customized, integrating several perception sensors to navigate nuclear facilities, and generate high-fidelity tridimensional digital twins fused with radiation measurements simulated using synthetic gamma sensors.
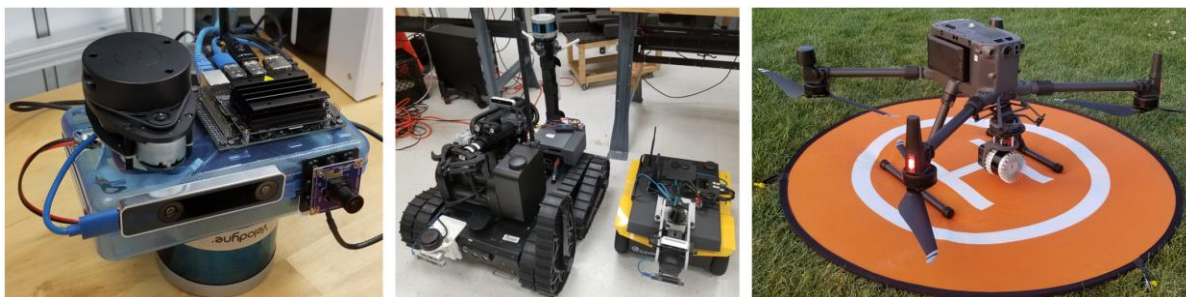
Figure 72. FIU's mobile platforms.

Virtual Radiation Sensing Framework

The framework has been developed using synthetic radiation fields, virtual sources, and simulated sensors. During tests and in-house deployments, simulated radiation sensors mitigate the lack of strong radiation sources and relevant radioactive environments at FIU.

Subtask 18.4.1: Results and Discussion

FIU's long-term surveillance efforts supported: a) mapping and robust navigation, and b) SST's off-riser sampler demonstration.

With the objective of fostering collaboration between FIU and WRPS in applying robotics to alleviate operational issues in Hanford tank farms, the DOE Fellows working on the project began preparing for their summer internships at WRPS to bring some of FIU's technologies and

algorithms to Hanford, which included running simulations of a Ur5e dexterous robotic manipulator sampling single-shell tanks.

Mapping and robust navigation

Since the last performance period, FIU captured maps were significantly improved in accuracy, resulting from fusing IMU data fused with multi-channel lidars, localized by iterative closest point (ICP) scan matching algorithm.
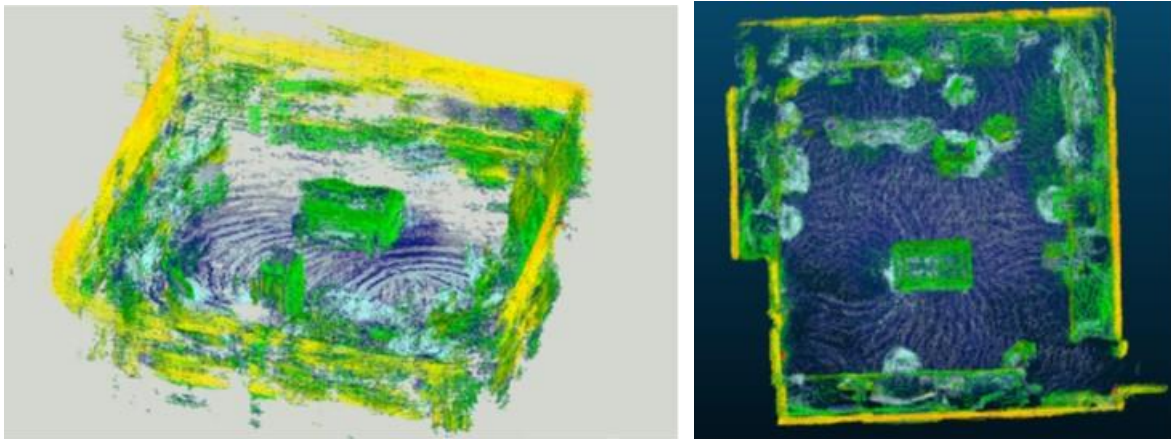
Figure 73. Original ICP point cloud (left) and improved map fusing IMU (right).

Figure 74 shows a map captured from the Robotics Laboratory's hallways, demonstrating the improvement in long-distance surveys and minimal distortion in right-angle turn captured as obtuse corners in previous mapping.
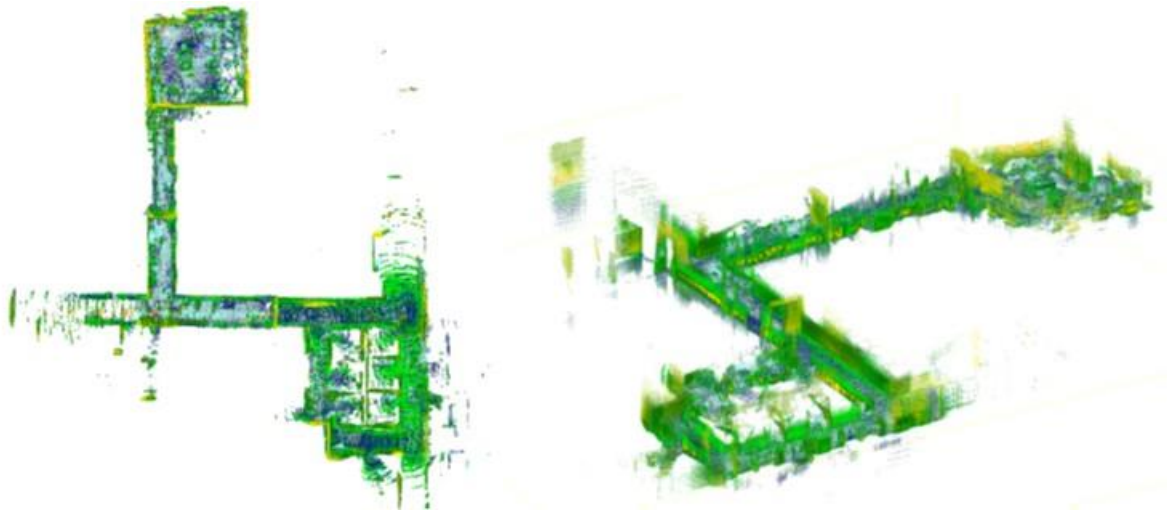
Figure 74. Captured maps from FIU's corridors.

Despite the improvements, the mapping framework needs further tweaking in areas with fewer geometric features. As highlighted in Figure 75, in the case of a specific small hallway, a jump occurred due to closed loop failure in the localization algorithm.
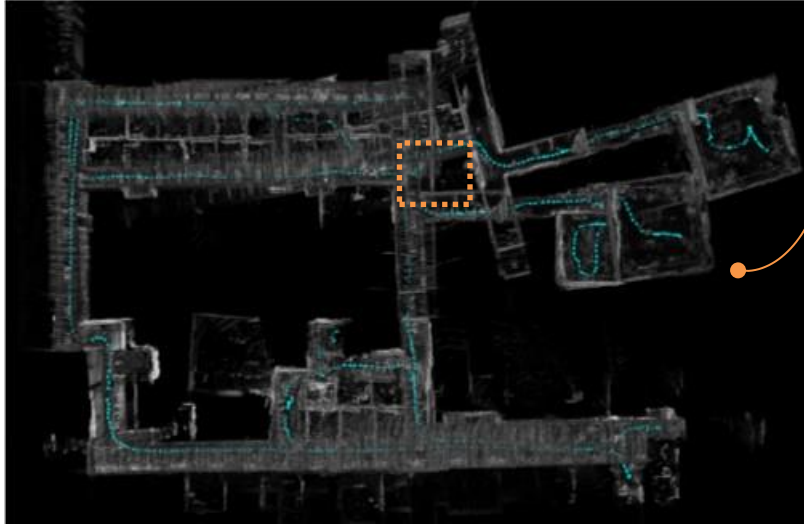
Figure 75. Closed loop failure in the localization algorithm.

To tackle map distortions, efforts were dedicated to fine-tuning the sequential navigation algorithm, which controls FIU's autonomous surveillance framework flow of actions and measurements. The tuning achieved a higher percentage of successful navigation runs traveling longer indoor distances without significant drifts in the captured maps, which is crucial in comparing environmental changes over time.

Figure 76 shows tridimensional maps generated manually and autonomously, replicating the trajectory where the paths are shown in cyan.

Figure 76. Indoor maps manually (left) and autonomously (right) generated.

The team also focused on autonomously surveying outdoor facilities, repeatedly mapping the same areas over time, as typical crew surveillance tasks. The in-house navigational framework was further developed and tested indoors at ARC through the modification of input sensor data and by demonstrating further robustness by mapping a different section of the floor. A 2D lidar was integrated and tested in order to observe if current issues with the navigational smoothness would be alleviated. Minor utility was observed with this sensor. The data from the 3D Ouster lidar was processed through filtering and cleaning techniques before being fed to the framework to detect obstacles. Notable improvements in the occupancy map were noted from this experiment including less noise and greater stability.

Figure 77 shows a new region of the indoor environment where the navigation framework was tested to demonstrate an ability to generalize with new locations.
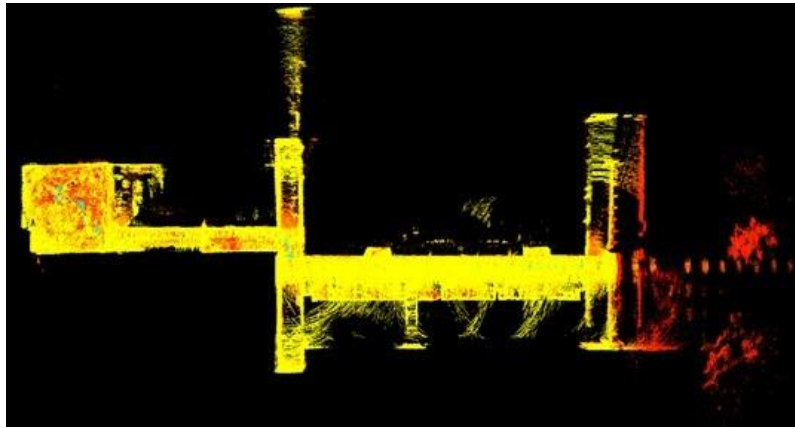
Figure 77. Partial region of ARC constructed using in-house navigation framework.

Figure 78 shows the resulting map created when the robot is driven in a loop a single time and when it is driven twice around the same path. The resulting maps are geometrically similar; however, the improvement is intended for the location of the waypoints which are set during the second lap.
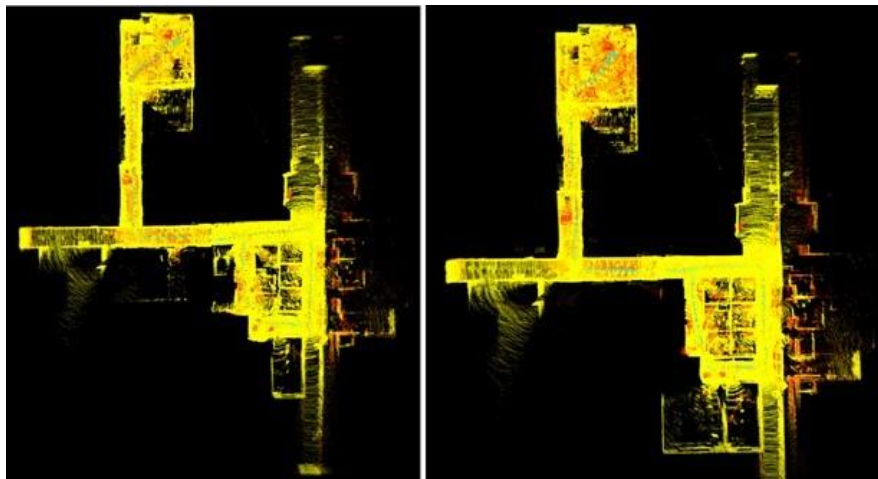
Figure 78. Partial map of ARC constructed using SLAM with a single lap (left) and two laps (right).

The accuracy in point cloud capture and digital twin reconstruction were further improved using FIU's mobile autonomous systems. The measures also include determining how well our simultaneous localization and mapping algorithms (SLAM) behave and tweaking the navigation stack performance to produce better maps during surveillance missions.

Figure 79 shows preliminary efforts to analytically quantify the quality of captured lidar point clouds during mapping instead of visually evaluating them based on known geometric features in the environment. The collapsed point cloud's silhouette was compared with the laboratory's floor plan. The deviation in boundaries gives inaccuracy estimations of our SLAM algorithm over space and time.
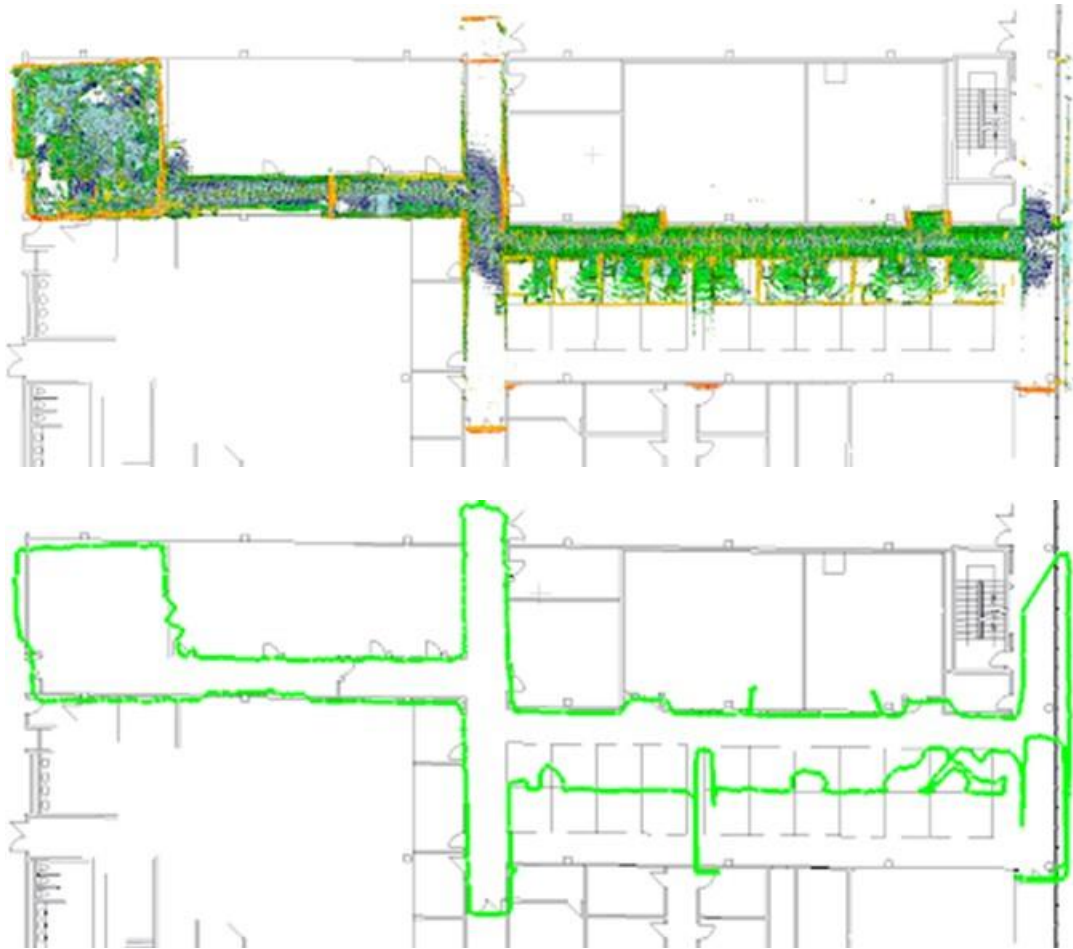
Figure 79. Captured point cloud (top) and collapsed floor plan (bottom).

Even though the scan seems to fit nicely on the floor plan, there is a lack of a well-implemented algorithm to calculate how well the contour from the scan fits into the target points. A method investigated was the classical Gaussian statistical method, which uses least squares to calculate the target point coordinates, conduct a comparative analysis and indirectly obtain accurate evaluation results.

Finally, FIU's framework's navigation stack was improved by integrating Move Base Flex, a highly flexible navigation framework for mobile robots. It exposes action servers for planning,

controlling, and recovering, providing detailed information of the current state and the robot's feedback, allowing better support for state machines. Figure 80 shows the current ROS node graph with the Gazebo setup.

Figure 80. ROS node network.

The team has also worked on transferring an off-road mobile platform from WRPS to FIU. The robot, shown in Figure 81, will be upgraded with FIU's Surveillance Framework and sensory packages to be deployed at Hanford next summer.

Figure 81. WRPS's off-road robotic platform.

SST's Off-riser Sampler Demonstration

In addition, to foster the collaboration between FIU and WRPS in robotics applied to alleviate operational issues in tank farms, the DOE Fellows working on the project began preparing for their summer internships at WRPS to bring some of FIU's technologies and algorithms to Hanford. This included running simulations of a Ur5e dexterous robotic manipulator and sampling single-shell tanks at Hanford, as illustrated in Figure 82.

Figure 82. Single shell tanks sampling simulation using the robotic manipulator.

Figure 83 shows tridimensional probabilistic occupancy maps generated from point clouds captured using depth. The occupancy maps are safety features allowing the manipulator to operate safely without colliding with the environment.
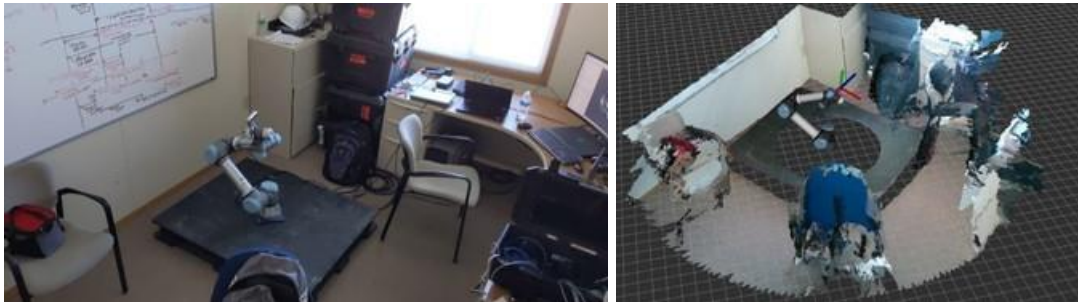
Figure 83. Environment mapping using a depth camera attached to a manipulator.

The robotics team at FIU is also supporting the DOE Fellow, Joel Adams, during his current summer internship at Hanford, by developing and building a vertical stand and tooling to simulate off-riser sampling at single-shell tanks using dexterous robotic manipulators. Illustrated in Figure 84, the motorized stand design uses a hoist and linear guides to lift the manipulator off the ground. There are plans to replace the stands with a cable system deployment at the tank farms.
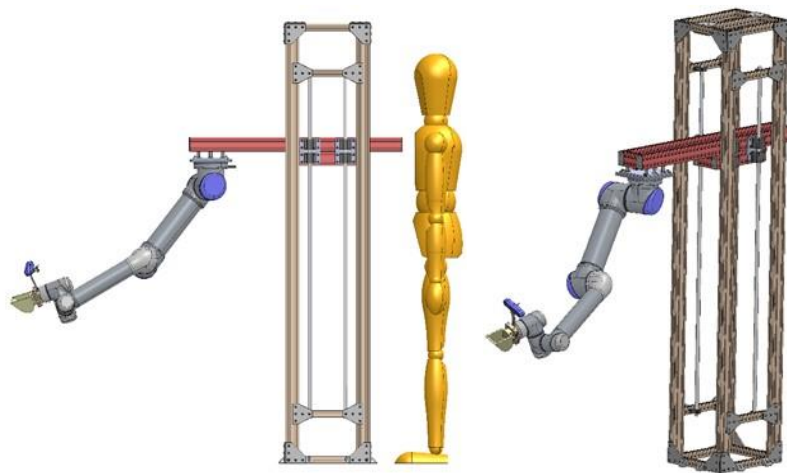
Figure 84. FIU's stand design.

Figure 85 shows the motorized stand built at FIU successfully lifting 45 pounds, equivalent to the manipulator weight. The system was shipped to WRPS's Cold Test Facility (CTF) for demonstration as part of the DOE Fellow summer internship.

Figure 85. FIU's robotics team developed a motorized stand to be used by DOE Fellows interning at WRPS in Hanford.

Figure 86 shows pictures of DOE Fellow Joel Adams' internship research activities, deploying tools and algorithms developed at FIU in coordination with WRPS site engineers.

Figure 86. DOE Fellow summer internship at Hanford.

The demonstration included assembling the robot on an upside-down mount, simulating riser deployment, to reach into a constructed testbed of simulant, as shown below in Figure 87.

Figure 87. UR5e off-riser sampling demonstration scooping simulant.

Figure 88 shows the robot after collecting the simulant by pouring it into a collection jar. The robot was programmed to scoop floor samples using a passive end effector developed at FIU. The system uses tridimensional maps constructed with an integrated stereo camera to perform sampling actions with obstacle awareness and collision avoidance.

Figure 88. Collected simulant sample.

Figure 89 shows a robot's captured environment map during sampling operation. The dark green objects show the pre-programmed mount setup to avoid self-collision with its frame.
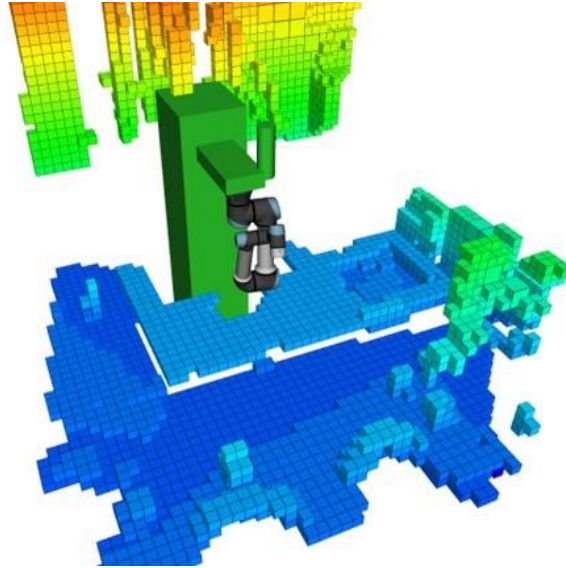
Figure 89. Captured environment map during sampling operation.

On Summer 2022, the off-riser sampler was successfully demonstrated at Hanford's Cold Test Facility in Richland. Figure 90 shows images of the Cold Test Facility technology demonstration. There were a number of operators and WRPS management personnel on-site to evaluate the potential of the sampler. The off-riser sampler managed to surpass the expectations of all and WRPS request FIU to continue the development. However, considering smaller risers and radiation hardened solutions.

Figure 90. Off riser sampler demonstration at Hanford.

Subtask 18.4.1: Conclusions

The efforts will continue the radiation mapping framework development and digital twin capture and reconstruction, improved by rigorous in-house deployments using our customized ground and aerial mobile platforms. The improvements will include:

a) integrating additional sensory relevant to surveillance of tank farms,

b) incorporating Machine Learning into the framework,

c) automating digital twin tasks such as segmentation, object detection, and automatic registration,

d) including more sophisticated models to our virtual radiation sensing framework,

e) implementing information-driven planning and control techniques and comparing their performance with traditional ones, and

f) fusing close-range data captured by 3D cameras with mid-range ones imaged by LiDAR, combining local accuracy with far-field awareness.

Instructions from the Multi-Agency Radiation Survey and Site Investigation Manual (MARSSIM) will be incorporated in our autonomous mapping algorithms to provide detailed guidance for planning, implementing, and evaluating environmental and radiological facility surveys conducted to demonstrate compliance with a dose-based or risk-based regulation.

During the summer, FIU mobile platforms will be potentially deployed at Hanford. Lessons learned during the team summer internships, deploying our sensors and algorithm in the Hanford tank farm, and interacting with scientists and engineers are crucial for further improving FIU's autonomous mapping framework, considering actual site challenges and conditions.

Subtask 18.4.1: References

1. DOE (2018, November). Post-Retrieval Activities Changing Hanford Tank Farm Footprint. https://www.energy.gov/em/articles/post-retrieval-activities-changing-hanford-tank-farm-footprint

2. S. Ferrari and T. A. Wettergren. (2021). Information-Driven Planning and Control. The MIT Press.

3. C. E. Rasmussen and C. K. I. Williams (2005). Gaussian Processes for Machine Learning. The MIT Press.

4. M. Popovic, T. Vidal-Calleja, J. J. Chung, J. Nieto, and R. Siegwart. (2020). Informative Path Planning for Active Field Mapping under Localization Uncertainty, IEEE International Conference on Robotics and Automation

5. C. Miskinis (2018, January). Combining digital twin simulations with virtual reality – what can we expect?. https://www.challenge.org/insights/virtual-reality-and-digital-twin

6. M. Berger, A. Tagliasacchi, L. Seversky, P. Alliez, G. Guennebaud, J. Levine, A. Sharf, C. Silva (2016). A Survey of Surface Reconstruction from Point Clouds. Computer Graphics Forum.

TASK 19: PIPELINE INTEGRITY AND ANALYSIS

Subtask 19.1: Pipeline Corrosion and Erosion Evaluation

Subtask 19.1: Introduction

The Hanford Site Tank Farm has implemented a Fitness-for-Service (FFS) program for the Waste Transfer System. The FFS program, based on API-579-1/ASME FFS-1, examines structural parameters of the waste transfer systems in order to develop erosion/corrosion rates for relevant system components. The FFS information is acquired from opportunistic evaluations of pipelines that have been removed from service. FIU-ARC engineers work closely with key Hanford high level waste (HLW) personnel and the contractor, Washington River Protection Solutions, LLC (WRPS), to support the FFS program, deliver solutions for sensor evaluations, conduct bench-scale testing followed by data acquisition and analysis for corrosion and erosion assessment. Previous efforts at Hanford included the installation of sensors on a number of the POR 104 components, to provide real time pipe wall thickness measurements. Due to various limitations, alternative approaches for remote permanently mounted pipe wall ultrasonic thickness measurement systems are being investigated.

FIU's efforts to support this scope have included investigating key options available in the market for remote, permanently mounted ultrasonic transducer (UT) and other sensor systems for HLW pipe wall thickness measurements and wear. Specific applications include straight sections, elbows and other fittings used in jumper pits, evaporators, and valve boxes. FIU assessed the use of various ultrasonic systems that are either commercially available or used previously at Hanford and selected the most promising systems for further evaluation. Two sensor systems were down selected. The Permasense UT sensor system and the fiber optic sensors from Cleveland Electric Laboratories (CEL) were acquired, and initial bench-scale validation testing was conducted. Following the initial bench scale tests, engineering scale testing was implemented on an in-house designed and installed test loop. The design loop has been established using 2- and 3-inch diameter straight and bend pipe sections to mount the sensors. The loop was eroded using a sand-water slurry and the Permasense sensors and the CEL sensors were used for thickness measurements [1,2,3,4,5,6]. The Permasense sensors were also tested for their performance in extreme environmental conditions under high humidity and temperatures. Finally, the feasibility of conducting radiation testing on those sensors was considered and a test plan was developed for implementation. Permasense UT sensors were used for thickness detection while the CEL sensors were used for anomaly detection. In addition, SRNL mass loss coupon erosion systems were evaluated for erosion and corrosion detection in the pipe loop at FIU. These included the SRNL coupons with the Pencil UT sensor [4,5].

FIU has successfully completed the sand water erosion tests on both carbon and stainless-steel coupons. Currently, FIU is investigating the effect of glass frit particle erosion and caustic simulant corrosion on the SRNL coupons. A bench scale mockup has been constructed and initial caustic simulant testing has been conducted. The static coupon immersion tests are also being performed in parallel. Benefits of this research include providing validation for new methods and technologies that will assist engineers in understanding the fault potential of HLW nuclear waste transfer components due to corrosion and erosion. By providing insights into determining if and when lines need to be removed/replaced, the unneeded excavation of transfer lines can be avoided saving

valuable time and resources. Also, more detailed and accurate guidelines can be developed governing the life expectancy of the transfer system and its components. By being able to have accurate predictions of points of failure from erosion, and by being able to monitor an entire pipeline's status in real-time, resources can be targeted to tackle preventative measures instead of reactive.

Subtask 19.1: Objectives

The motivation for this subtask is to assist DOE, WRPS and SRNL in providing realistic estimates of the remaining useful life of the components, to incorporate those estimates into future design plans and to automate the erosion corrosion monitoring. This subtask includes the investigation of various sensor systems and fluid flow dynamics to detect thinning in pipes and tanks along with real-time evolution of the wear using SRNL's mass loss/erosion coupons. Hence, there are three objectives for this task for structural health monitoring using various types of sensors. Including:

- Evaluation of SRNL's carbon and stainless-steel coupons for erosion testing.
- Caustic simulant-induced corrosion evaluation on FIU's custom bench scale flow loop.
- Development of data analytics and fluid flow dynamics-based models for automated erosion and corrosion detection.

Subtask 19.1.1: Evaluation of SRNL Stainless Steel Coupons for Erosion Testing using DWPF Glass Frit

Subtask 19.1.1: Methodology

The purpose of this research was to test and demonstrate that the SRNL erosion and mass loss coupons could provide an in-situ method for collecting erosion and mass loss rates from a pipeline using the stainless steel and carbon steel coupons during operation. Previous work included initial testing with the first set of carbon steel coupons provided by SRNL to FIU [4]. The application of these coupons was experimentally tested in an engineering scale pipe loop by circulating sand-water slurries of varying densities and grit sizes. The intended advantage of the replaceable coupons is their ability to easily calculate mass loss/gain and to gain insights into qualitative data such as erosion patterns on the inside of the pipes.

This past year's work included the use of DWPF glass frit as a material for accelerated erosion in the pipe sections using the SRNL mass loss coupons and the Permasense Sensors. The present work evaluates the SRNL coupons for erosion characteristics using glass frit replicating the frit used by the DWPF at SRNL and other sites. Testing and evaluation of the glass frit was conducted on the engineering scale test loop at FIU. Initially, FIU held conversations with the SRNL team and was able to acquire a sample frit (size #803) from SRNL. A quick market survey resulted in an initial quote for a similar size frit available commercially. Due to the high cost, alternative glass frits were compared with those available from the company, Bekeson Glass LLC. The glass frit that Bekeson Glass produced was manufactured specifically for vitrification of nuclear waste. For our erosion testing, other glass frits were suggested that are comparable in grit/micron size to the Frit 625 (similar to frit 803). Once samples of alternative glass frit were acquired, they were compared to the original sample sent by SRNL to determine if they can be a viable replacement.

Next, additional information on the glass frit similar to SRNL glass frit #803 was obtained, and meetings were conducted with the SRNL scientists to finalize the test matrix to initiate the experimental testing. Comparing both frit types, it was noted that compared to Frit 803, Frit 625 includes Al_2O_3 and had a slightly lower total alkali concentration (sum of Li_2O and Na_2O). SRNL scientists provided information on studies conducted using Frit 625 that revealed the target frit composition (%wt.) of Frit #625 as Al_2O_3(1%), B_2O_3 (8%), Li_2O (7%), Na_2O (6%) and SiO_2 (78%).

Figure 91. Sample image of Frit 625.

Finally, quotes were obtained for the glass frit # 625 as suggested by SRNL scientists. The frit size available with Bekeson glass LLC, for our experiments, possessed a particle size in the range of 70 to 180 microns. Among those, max weight % greater than 177 microns is 2%, and max weight % < 74 microns is 10%, meaning higher weights with larger size particles in the mixture. Frit availability is in 4.25-gallon plastic pails that contain approximately 40-50 lbs per pail. The original proposed test matrix developed for testing with glass frit is provided in Table 1. Initial testing included only glass frit in increasing volumetric concentration. Sand was to be added during the last three phases of the testing.

Table 3. Proposed Test Matrix for Erosion Tests using DWPF Glass Frit

Test	Coupons	Frit # 625 (gallons)	Medium Sand (30/65) (gallons)	Coarse Sand (20/30) (gallons)	Very Coarse Sand (6/20) (gallons)
Phase 1	2 SS and 3 CS	2	0	0	0
Phase 2	2 SS and 3 CS	4	0	0	0
Phase 3	2 SS and 3 CS	5	0	0	0
Phase 4	2 SS and 3 CS	2	1	0	0
Phase 5	2 SS and 3 CS	2	1	1	0
Phase 6	2 SS and 3 CS	2	1	1	1

Quotes were obtained from Bekeson glass LLC for 100 lbs of size 625 Glass Frit. This amount was based on materials needed for 1 testing cycle and available ordering options that are limited to 4.25-gallon tear-top pails (holding approximately 50 lbs of frit each). The cost of these materials before shipping is quoted to be 800 USD. Alternatively, another source of glass for this experiment was found locally at Florida Silica Sand Company. Glass beads were available in a comparable

size to the glass frit. The same amount of material was quoted to cost $145 USD including freight. Both options were considered with input from SRNL prior to proceeding with the acquisition of the materials. In addition, the glass frit properties were compared to similar size glass beads. The rounded beads have less damaging capacity to the pump when compared to the frit. Glass beads were ordered from Florida Silica Sand Company and SRNL shipped the new machined coupons made of carbon and stainless steel.

Next, FIU moved forward with testing glass beads replicating frit 803 (sample provided to FIU by SRNL) for evaluation testing using the mass loss coupons. Additionally, new coupons received from SRNL were installed in the pipe section. For the first glass testing, two 50lb. bags of the beads were purchased for $70. The glass beads were acquired locally from Florida Silica Sand Co. (FSS) in Miami, FL. The magnified images of the 803-frit sample and the AE glass beads were compared. Physically the glass beads were much smoother in texture, but the size was similar to frit 803. The difference is due to the beads being rounded versus the chipped structure of the frit.

Figure 92. New SRNL coupons (left), 803 glass frit & AE glass bead samples (center) and granular structure (two on the right).

Subtask 19.1.1: Results and Discussion

During the summer, an engineering scale test loop was prepared for testing with glass beads. The new set of coupons received from SRNL were machined to fit the pipe test section and the first round of water tests was also conducted in the loop. The final test matrix listed in Table **4** was followed for conducting the glass bead tests. Changes were made to the previously suggested test matrix based on the initial experimental testing and from comments from the SRNL team. There are 3 carbon steel and 2 stainless steel coupons placed in the 3-inch pipe section with locations in the elbow, top and bottom parts of the pipe.

Table 4. Final Test Matrix for Erosion Tests using DWPF Glass Frit.

Test	Coupons	Glass Beads (gallons)	Medium Sand (30/65) (gallons)	Coarse Sand (20/30) (gallons)	Very Coarse Sand (6/20) (gallons)
Phase 1	2 SS and 3 CS	2	0	0	0
Phase 2	2 SS and 3 CS	4	0	0	0
Phase 3	2 SS and 3 CS	6	0	0	0
Phase 4	2 SS and 3 CS	2	1	0	0
Phase 5	2 SS and 3 CS	2	1	1	0
Phase 6	2 SS and 3 CS	2	1	1	1

In the preparation of the loop, sand deposits located inside the test section from prior testing were removed by flushing with water and vacuuming the pipe section. The coupons were also prepared by cleaning prior to installing in the test section. It is to be noted that some of the coupons are old and some are new. Before and after borescope images inside the pipe are shown in Figure **93**. The left image shows sand deposits at the bottom and the right image is after cleaning. The image also shows coupon flushed inside the pipe section.
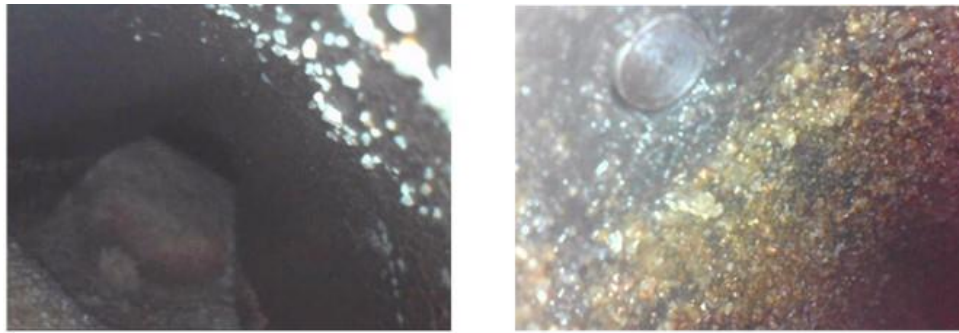
Figure 93. Borescope image of the sand deposited inside the pipe (left) and cleaned pipe section (right) with flushed coupon.

Phase 1 of the glass beads testing was completed successfully, and erosion results were analyzed for future tests. Two different sizes of glass beads (as suggested by the SRNL scientists) were tested. The engineering scale test loop was prepared for testing and the tests were conducted according to the test matrix. A total of about 45 hours of testing was conducted with the first 25 hours using glass beads of size AE (size range – 0.0059 to 0.0035 inches diameter or 100-170 screen size) and the remaining time with bead sizes AE and AC (size range – 0.0049 to 0.0098 inches diameter or 60-120 screen size). The total volume of glass beads was 12 gallons. A higher volume than the standard 10% was chosen to account for the settlement of the beads at the bottom of the tank and some on the pipe sections over time. During testing, sand was added in intervals of 2 hrs. Results are plotted in the graph (Figure **94**). Based on the plots, it is evident that the erosion with bead sizes AE and AC with 10% volume fraction and 45 hours of testing showed very minute levels of erosion (fluctuations in the data). There was 0.01 mm thickness change observed in the elbow and bottom coupon at the beginning of the tests. Later, the top sections showed erosion and at the end of Day 5 of testing, slight erosion was observed at the bottom coupons. The reasons are due to the eroding particles (size and velocities) and some settlement of beads. Results were discussed with SRNL scientists to increase the bead size and volume in future testing.
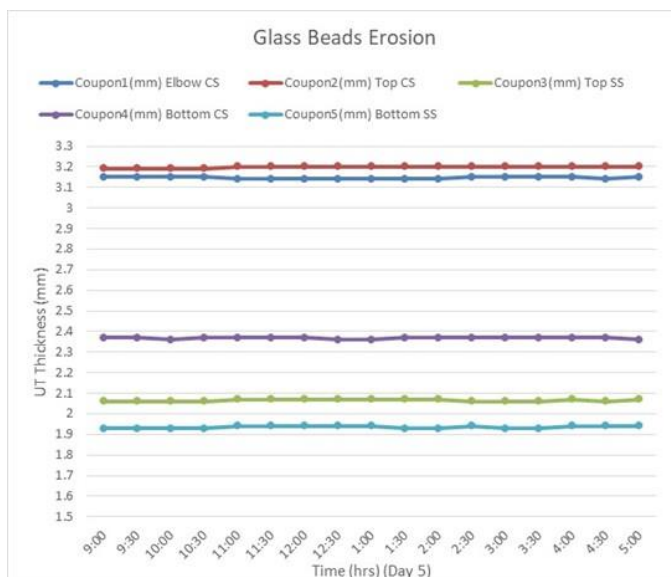
Figure 94**. Erosion data with a 12-gallon volume of glass beads (sizes AE and AC) after 45 hrs of testing.**

After minimal erosion, using simulants suggested by the site contacts, in the initial round of testing, additional materials were also considered that include aluminum oxide, steel shots and larger glass beads.

Figure 95. Different erosion simulant options.

Next, data analysis of the results from previous testing with small size glass beads (2 sizes) was conducted and details were discussed with the SRNL scientists. Test data from approximately 45 hours of testing with two bead sizes (AE and AC) indicated very minute erosion. Hence, based on the advice from SRNL scientists, FIU started to investigate the next level of beads (larger size) and continued to test for erosion. Larger size glass beads were procured by the end of July.

During the month of August, the next stage of glass bead testing with larger sizes was also completed. A total of 60 hrs of testing was conducted. Coupon images were acquired to observe visual erosion. A pencil UT sensor was used to detect the thickness changes (in the coupon surface

thickness). Data analysis was conducted to check for evident erosion. Results showed no evident erosion. Hence, it was decided that the loop will continue to operate conducting tests for a period of 2-3 months with 10-12 hrs per week.

In addition, discussions were conducted with the SRNL scientists regarding the material of the pipe loop. Based on the discussions, new coupons will be made to replicate the material of the pipe loop for investigating the erosion patterns in the same material. To make new coupons, the pipe material specifications have been obtained from the manufacturer and confirmed with the ASTM standards. Accordingly, the following image shows carbon composition in the material selection for carbon steels. The different classes of carbon steels are categorized by the percentage of carbon that is mixed with the base element, iron. The carbon percentages are provided as: Ultra-high carbon steel 1.00 - 2.00 %, High carbon steel 0.60 - 0.99 %, Medium carbon steel 0.30 - 0.59 %, Low carbon steel 0.16- 0.29%, and Mild carbon steel 0.05 - 0.15 %. Additionally, the ASTM standard for the pipe components (nipples) currently used in the engineering scale loop is ASTM A53, material typically denoted as welded steel pipe. Information obtained from the pipe supplier (A&B Pipe Company) is shown in Figure **96** detailing the pipe types and standard dimensions.
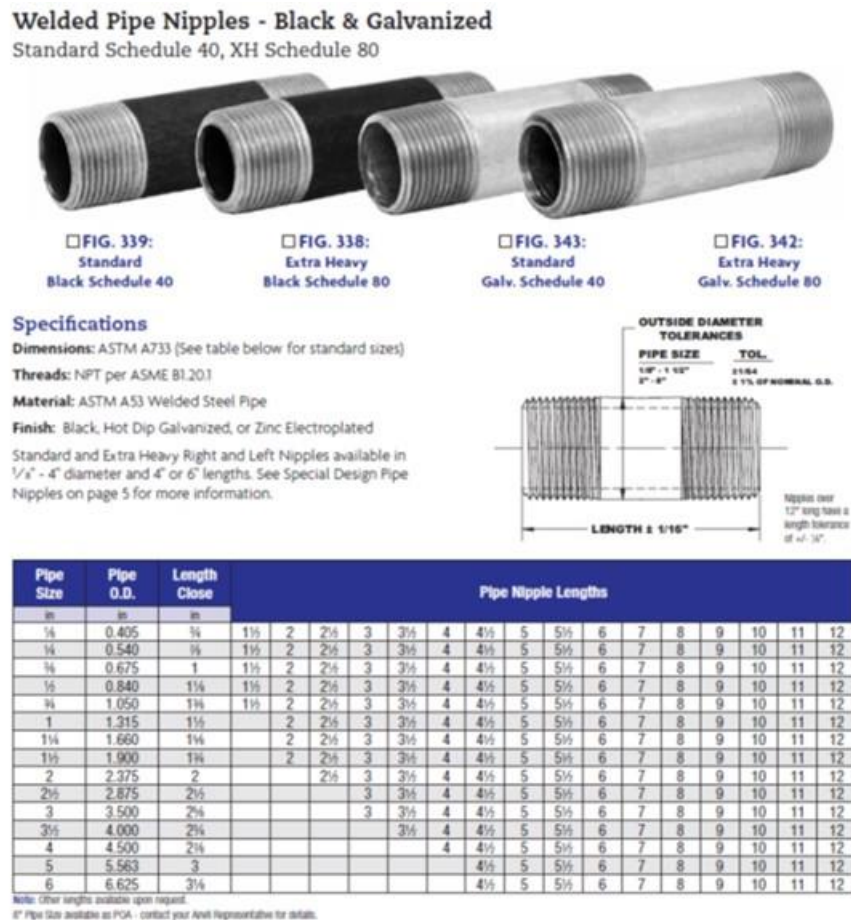

Figure 96. Pipe components specifications provided by the supplier (A&B pipe company).

Currently, FIU is aiding the SRNL team with their investigation of the machining behavior of materials based on their properties particularly in the low, medium, and high carbon steels and

stainless steels by providing the material properties and the erosion test characteristics using glass bead testing.

Subtask 19.1.1: Conclusions

Real-time particle erosion effect on the SRNL coupons has been verified and validated on an engineering scale test bed using the glass frit replicating SNRL's DWPF frit. Initial experimental results showed much less change in erosion in stainless steel when compared to the carbon steel coupons. The location of the coupon affected the erosion pattern on the coupon surface. Additionally, the UT measurements (thickness) showing wear were affected by the glass bead sizes and sand proportions, grit size and the time of addition of the sand particles in the simulant mixture. In future, the sand testing will be continued for longer durations and mixtures for glass beads and sand particles will be considered for erosion.

Subtask 19.1.1: References

1. Aravelli A., McDaniel, D., Davila, C., "Real-time Erosion-Corrosion Detection in Waste Transfer Pipelines using Guided Wave Ultrasonic Sensors", Proceedings of the Waste Management Symposia 2018, Phoenix, AZ, March 18-22, 2018.

2. Aravelli, A., Thompson, M., McDaniel, D., Krutsch, M., McNeilly, M., Imrich K., Wiersma B., "Advanced Fiber Optic and Ultrasonic Sensor Systems for Structural Health Monitoring of Pipes in Nuclear Waste Sites", IMAPS 52nd International Symposium on Microelectronics (IMAPS), Boston, MA, Sep 30-Oct 3, IMAPS (2019).

3. https://srnl.doe.gov/tech_transfer/tech_briefs/SRNL_TechBriefs_UltrasonicThicknessMassLossMeasurement.pdf.

4. Aravelli, A., McDaniel, D., Thompson, M., Imrich, K., Wiersma, B., "Erosion-Corrosion Detection in Carbon Steel Pipe Loops using SRNLs Thickness and Mass Loss Measurement Coupons", Waste Management 2020 Conference, Phoenix, AZ, March 2020.

5. https://www.olympus-ims.com/en/shop/item/269-productId.570437480.html

6. Thompson, M., McDaniel, D., Wiersma, B., Aravelli, A. "Structural Health Monitoring Technologies for Wear and Anomaly Detection in Nuclear Waste Transfer Systems", Waste Management 2021 Conference, Phoenix, AZ, March 2021.

Subtask 19.1.2: Caustic Simulant Testing using the Bench Scale Flow Loop

Subtask 19.1.2: Methodology

The purpose of this subtask is to test and demonstrate that the SRNL coupons could provide static and dynamic methods for collecting corrosion rates from pipelines using stainless steel and carbon steel coupons. For this, a bench scale loop was custom designed and installed for testing replicate caustic simulants with various concentrations. The recipe for the salt solutions was prepared by SRNL scientists and transmitted to FIU for testing in the bench loop [1]. Static testing was conducted by immersing the coupons in bottles with 2, 4 and 6 Molar salt solutions, while the dynamic testing is conducted by placing the bench scale loop in a fume hood.

Bench Scale Loop

A bench scale flow loop has been developed with a smaller footprint to test the effect of caustic flow in the pipe components. The bench scale chemical test loop has been designed as a closed loop system with simulants circulating between a tank and a pump. The pump was down selected from several pumps (available in the market) to the required flow and size parameters. It is a Dayton 1/3 HP pump with stainless steel impeller and casing suitable for caustic solutions and has a maximum flow rate of 21gpm @ 5 ft of head. The test loop mainly consists of 2- and 3-inch diameter schedule 40 carbon steel straight sections. The elbows are made of stainless steel to reduce the overall weight of the loop. The test section of 3-inch nominal diameter is made modular with 3 inches to 2-inch reducers on both sides. The test section will be used for testing the SRNL coupons (both SS and CS). The loop's footprint consists of about 5 ft length and 2 ft width with the overall pipe length about 13 ft. It is rested on and clamped to a Unistrut framework. Initially, 6 designs were made, and one was down selected based on the test variables and physical laboratory accommodation. Solidworks software was used to draw the designs. The final assembled loop is shown in Figure 97.

Figure 97. Bench scale flow loop.

Initial water tests on the custom-built bench scale loop, for leaks and thermal gradients, were conducted successfully. The 3-inch x 30-inch carbon steel test section was delivered to SRNL for customization in order to house coupons for testing. The section needed to be custom fitted to include 4 coupons, 2 on the top of the pipe and 2 more on the bottom, aligned concentrically. Additional components considered include - flow rate meters/sensors, clear pipe sections and drain valves. A mechanical flow meter has been utilized for installation on the smaller side of the loop (12-inch section) (Figure **98**) A 3-way, 2 piece stainless steel ball valve (Figure **98**) was procured for draining caustic solutions and was attached to the ¾ inch pipe section connecting the tank outlet.

Figure 98. Flow meter to replace 12-inch pipe section (left) and 3-way ball valve (right).

The bench scale chemical loop was upgraded with the acquired 3-way ball valve from Grainger. The valve is installed below the gravity drain polyethene tank to allow for easy draining of the loop. The valve is ¾ in and has 3 threaded female outlets where a chemically resistant hose can be attached if necessary. The valve is made of 316 stainless steel and is rated for chemical resistance for all the ingredients in our mixture. The next step is to run more water tests to make sure the valve fit is optimal. Figure **99** below shows images of the inlet of the loop before and after the installation of the 3-way valve.

Figure 99. 3-Way ball valve location (red arrow) (left) and installation (right).

In preparation for testing using the bench scale flow loop, the clean-up of our laboratory at FIU took place. The fume hood was previously housed for the non-metallic task (another experiment). This lab has been cleared and refitted with the secondary containment (spill deck) to account for any leaks or incidents. Figure **100** shows the fume hood with the secondary containment. The bench scale loop will be placed on top of the spill deck.
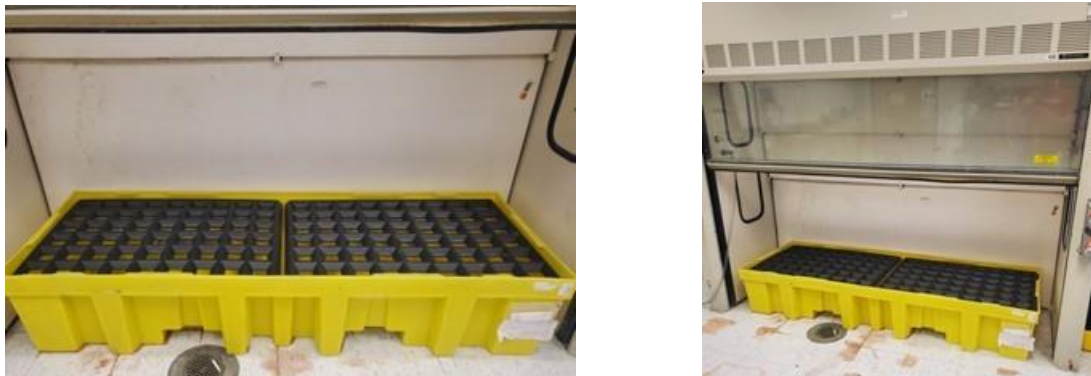
Figure 100. Inline polypropylene spill deck (secondary containment) inside fume hood.

Upon complete assembly of the bench scale corrosion pipe loop, the 3-inch section was drilled with holes to incorporate the coupons at 4 points (2 top and 2 bottom) and the loop was placed inside a fume hood for experiments. Figure **101** shows the assembled loop with coupon locations along with the borescope images of the coupons flushed inside the 3-inch section. To quantify the change in thickness due to any associated caustic corrosion, a UT sensor (Olympus V260-SM UT pencil sensor [2]) was used and the coupon surface image was captured. Mass loss was also determined. The bench loop placed inside the walk-in fume hood is shown in Figure **102**.

Figure 101. Coupon locations (arrows) (left), coupon joint (center) and borescope image of the coupon (right) in the pipe loop.

Figure 102. Assembled bench scale loop inside the fume-hood for caustic simulant testing.

Caustic Solution Preparation for Corrosion Testing

In preparation for testing of the caustic simulants to be used for static and loop testing, a baseline mixture of 250 ml and a batch mixture of 18 L with 2M solution concentration was prepared. The 18 L solution was mixed in 10 batches of 1,800 ml due to the size of the equipment available. These 10 batches were combined in a 5-gallon bucket and then pumped into a polypropylene tank. Test solution preparation with weighing and mixing the chemicals using mechanical and magnetic stirrers is shown in Figure **103**. The chemical compositions as suggested by SRNL (baseline 250ml solution), were used to calculate the composition needed for 18L of the solution. Details are provided in Table 3.
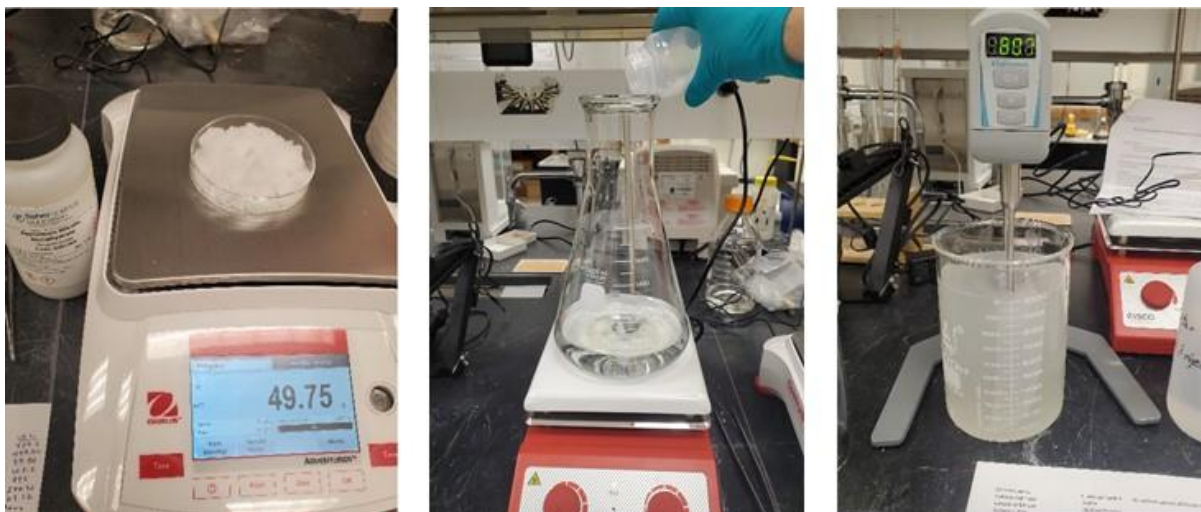

Figure 103. Caustic solution preparation -weighing (left), mixing (magnetic stirrer) (middle) and mechanical stirring (right).

Table 5. Caustic Simulant Concentrations (Baseline and Total Test Volume)

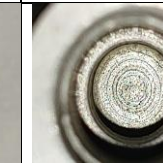| Chemical	Mass (g) (250ml) (baseline)	Mass (g) (18L) (total)
Sodium Hydroxide	10.1	727.2
Aluminum Nitrate	6.91	497.52
Sodium Sulfate	0.522	37.58
Sodium Carbonate monohydrate	2.6	187.2
Sodium Nitrate	11	792
Sodium Nitrite	3.86	277.92
Sodium Chloride	0.96	69.12

Subtask 19.1.2: Results and Discussion
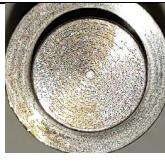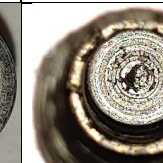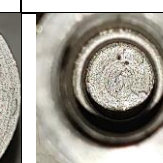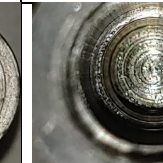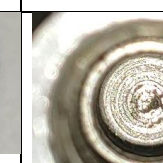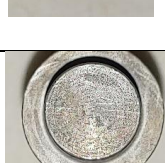
Caustic corrosion was experimentally determined under static and dynamic conditions. In order to conduct both tests, chemical solutions were prepared using the simulant recipe provided by the SRNL scientists. The volume of solution prepared was scaled according to the requirements. Static testing and results are discussed next followed by the bench loop results.

<u>**Static Coupon Test Results**</u>

Coupon immersion tests required complete immersion of coupons in the bottles. 2M concentration, 4M and 6M solutions were prepared, and coupons were immersed in the solution bottles. The caustic simulant static testing was continued for about 10 months and test data was collected every 2 weeks. The visual inspection (images) sample set over a period of 6 months are shown in Table 6 and Table 7, respectively. The Stage 2 testing (November 2021 month) coupon images show evidence of corrosion (Table 6). The 4M and 6M stainless steel have evidence of pitting corrosion evident in the visual images. The 2M stainless steel did not show many signs of pitting corrosion. The 2M carbon steel corrosion showed some minor corrosion formation inside the coupon towards the center. The corrosion rate in 4M and 6M carbon steel has remained the same. Static testing of the coupons was continued for 10 months (until August 2022) as planned. Table 7 shows the images of the 6 coupons over the period. In the high concentration solution dipped coupons, pitting corrosion continued to be observed in the carbon steel coupons. The stainless-steel coupons had layers of chromium oxidation on the interior and in some circular sections. These results provided baseline information for conducting dynamic tests.

Table 6. Static Immersion Visual Test Results of the SRNL Coupons (Month of November 2021)

Date	Molarity	Carbon Step	Carbon Inside	Stainless Step	Stainless Inside
11/12/21	2M				
11/12/21	4M				
11/12/21	6M				
11/30/21	2M				
11/30/21	4M				
11/30/21	6M				

Table 7. Static Test Coupon Images for 4 Weeks (Month of August 2022)

Month	Molarity	Stainless Step	Stainless Inside	Carbon Step	Carbon Inside
August 2 Weeks	2M				
August 2 Weeks	4M				
August 2 Weeks	6M				
August 4 Weeks	2M				
August 4 Weeks	4M				
August 4 Weeks	6M				

The pH of the solution was also measured during the experiments. It was observed to vary over time and the data during a 40-week period are shown in Figure **104**. It is evident that the pH has constantly been increasing during the tests. This leads to the conclusion that the solution turns to the basic side of the pH scale (concentrated base). This could be due to the increased corroded particles in the solution. Also, the pH value has recently been observed to be above 14. The reason is due to a slight discrepancy in the instrument along with the tendency for the solution to become a highly concentrated strong base solution (NaOH solution). Mass data was also collected for the

coupons, and it was observed that the coupons have been constantly losing mass with time. The tests will continue until the end of the year.
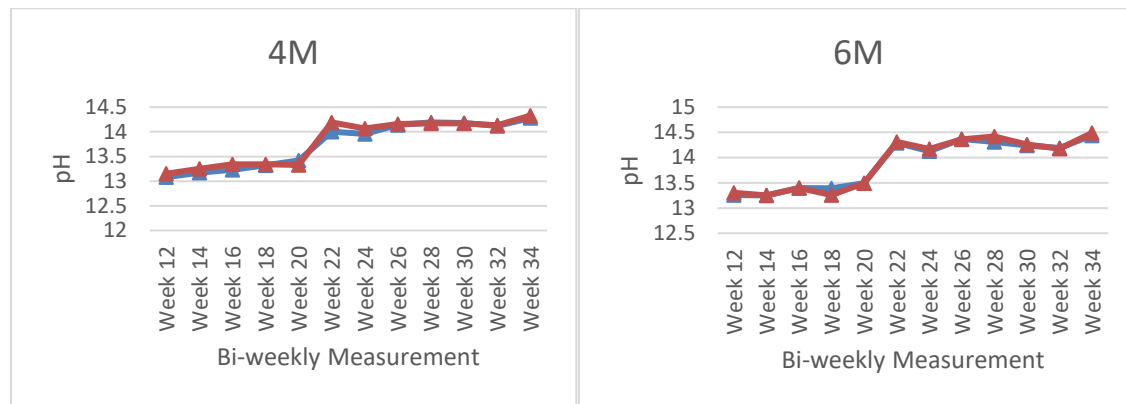
Figure 104. Static coupon test results for pH change in 4M and 6M solutions.

The mass loss captured during the 20-week period is shown in Figure **105**. It is seen that there was an initial dip in the mass loss and then it continued gradually, indicating stability during the corrosion process (oxidation). Also, samples were flushed during some of the experiments to clear the salt deposits over time. It is evident that the 6M solution-based carbon steel sample coupon resulted in a greater mass loss when compared to the 2M sample, validating a higher rate of corrosion with increase in caustic concentrations.
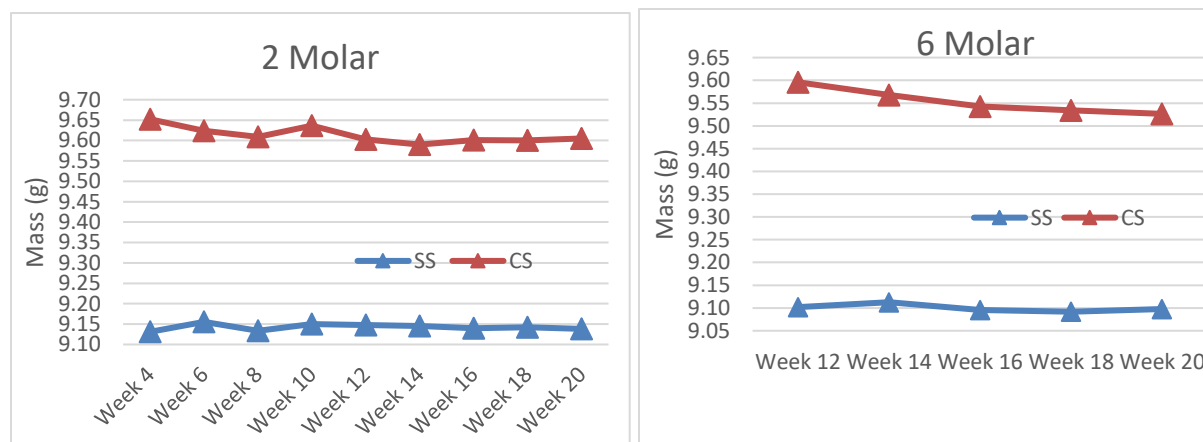
Figure 105. Mass change in 2M and 6M solutions.

In-situ Simulant Testing on the FIU-Developed Bench Scale Loop

Construction of the caustic loop was followed by conducting leak tests (water) on the loop to assess the functionally of the loop at its current configuration. During the tests, water was circulated and the temperature variation while circulating water for about 5 hrs was tested. During this test, thermal conditions of the loop were examined using a Etekcity Lasergrip 774 Infrared Thermometer [4] and a Klein Tools TI 250 Thermal Imager [5]. Temperatures were taken every

hour for the duration of the test. No leaks were observed throughout the trial. Thermal images using the camera are also shown in Figure 106.

Temperature variation at critical sections of the loop (obtained using the IR thermometer) is shown in Table 8. It is evident that a maximum temperature rise of 18-20°F is observed over 5 hrs in the loop components. Also, a maximum of 3°F difference is observed between different sections of the loop at any instant. These results indicate that the loop heats up gradually. This information will be used as a guide during the caustic chemical circulation.

Table 8. Temperature Variation During Water Tests for the Bench Loop

Time (hrs.)	1/2'' Section	2'' Section	3'' Section	Pump	Tank
0	79.2° (F)	79.2° (F)	79.2° (F)	79.2° (F)	79.2° (F)
1	97.2°(F)	99.3°(F)	100.2°(F)	124°(F)	96.6°(F)
2	109.4°(F)	109.8°(F)	110.7°(F)	127.7°(F)	106.1°(F)
3	113.9°(F)	114.4°(F)	115.8°(F)	129.6°(F)	111°(F)
4	115.6°(F)	115.4°(F)	118.5°(F)	135.6°(F)	116°(F)
5	118.7°(F)	116.7°(F)	118.4°(F)	135.6°(F)	116°(F)
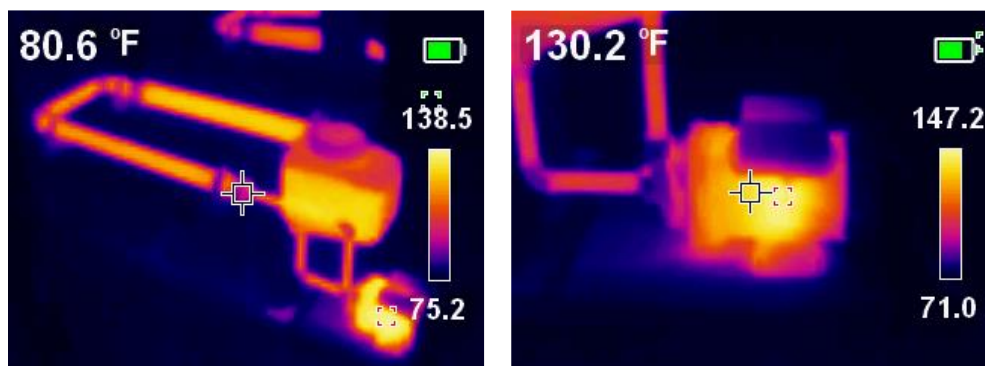
Figure 106. Thermal images of the bench scale loop during water tests.

In the next phase, 2M salt simulant testing was completed for about 2 months and the loop cleaned for the next phase of testing with 4M salt solutions. Results show minute levels of mass changes and no evident visual erosion or corrosion. Coupons will be placed under the SEM in future. Coupons have been taken out of the loop and images are shown in Figure **107**. Three (3) of the 4 coupons had a black residue/precipitate on the contact surface. Images before and after wiping off the coupon were taken. After cleaning there was no obvious change to any of the coupons. Also, the coupons were weighed for mass loss/gain. It is evident that the top 2 coupons have slightly lost weight and the bottom coupons have gained weight slightly. Loss of weight can be attributed to the abrasion of the fluid-salt mixture and corroded metal particles flowing in the pipes. The weight gain is due to salt sediment formation and deposition at the bottom of the horizontal pipe sections.

Mass change is given in Table **9**. The condition of the pipe loop inside surface, taken from the tank opening, is shown in Figure **108**. Currently, additional chemicals are being procured to mix the 4M solutions.

Figure 107. Sample coupon images (before cleaning).

Table 9. SRNL Coupon Mass Change in 2M Caustic Simulant Testing in 2 Months

Coupon	Initial Mass (gm)	Final Mass (gm)	Mass Loss (gm)
W1(CS)	9.4224	9.4091	0.0133
W2(CS)	9.1809	9.1707	0.0102
W3(SS)	9.2916	9.2918	-0.0002
W4(SS)	9.3519	9.3528	-0.0009

Figure 108. Pipe surface – internal 3-inch section (left) and eroded, corroded pipe threads (right).

Results obtained from the 2M solutions showed extremely mild chemical corrosion and hence for the next phase of testing it has been decided to use 6M solutions. The testing procedure will include 3-6 months of circulating 6M salt simulants in the bench scale loop placed inside the fume hood. The loop was prepared for the tests by conducting water tests. Formation of salt precipitates was observed in the lower sections of the pipe (3/4 inch) below the reservoir tank (Figure **109**). These deposits were formed due to the solidification of a minor chemical leak below the tank. The leak was cleaned, and the pipe junctions sealed. Additionally, the power cord was not rated for this application since the pump's electrical wiring needed a ground wire according to the specifications. A new replacement cable set was obtained and attached to the pump's electrical wiring circuit (Figure **109**).

Figure 109. Chemical precipitates (left), pump wiring configuration (center) and new wiring (right).

Currently, FIU is procuring chemicals to start with the 6M salt solution tests. Also, some sections of the pipe loop will be shipped to SRNL for further material characterization.

Subtask 19.1.2: Conclusions

The SRNL coupons have been verified and validated for caustic chemical corrosion over a period of time under static and dynamic flow conditions. The methods of static immersion and real-time loop testing have been used. A custom-built loop has been constructed and tested at FIU. The chemical recipe for the simulants was prepared by SRNL scientists and transmitted to FIU. Static immersion experiments conducted on the coupons showed evidence of minute mass loss and visual corrosion (pitting and oxidation). A greater level of corrosion was observed in the carbon steel coupons compared to the stainless-steel coupons. There were clear signs of pitting corrosion found inside of the 6M solution sample coupons, indicated by the holes near the bottom. The pH values were observed to have constantly increased, indicating a shift towards a more basic concentration. Mass loss was minute. In future, the simulant testing will be continued for longer durations and using 4M and 6 M salt simulants in the bench-scale flow loop inside a fume hood.

Subtask 19.1.2: References

1. Wiersma, B. J., Peters, T. B., Poirier, M., "Simulant Recipes for Flow-loop Testing at Florida International University", SRNL-L3000-2020-00017, December 18, 2020.

2. https://www.olympus-ims.com/en/shop/item/269-productId.570437480.html\

3. Aravelli, A., McDaniel, D., Thompson, M., Imrich, K., Wiersma, B., "Erosion-Corrosion Detection in Carbon Steel Pipe Loops using SRNLs Thickness and Mass Loss Measurement Coupons", Waste Management 2020 Conference, Phoenix, AZ, March 2020.

4. https://www.etekcity.com/products/infrared-thermometer-lasergrip-774.

5. https://www.kleintools.com/catalog/thermal-imagers/rechargeable-thermal-imager.

Subtask 19.1.3: Automated Erosion and Corrosion Detection using fluid flow dynamics and advanced data analytics

Subtask 19.1.3: Methodology

Erosion and corrosion testing in the flow loop provides adequate data for developing automated erosion and corrosion detection process; and condition monitoring of the HLW pipe system components. This subtask will investigate the use of experimental and flow simulation data to develop advanced algorithms for preventive and predictive maintenance of the tanks and transfer lines. This year's scope of work included an initial literature review of the methods for automating

the process using advanced data analytics and algorithms. In addition, the fluid flow simulation software options were investigated and evaluated for conducting the flow simulations.

Research and analysis of the fluid flow dynamics of the bench scale pipe loop was conducted using fundamental fluid dynamics and pipe flow concepts. This will provide baseline theoretical data to compare with experimental results and to optimize the number of tests.

Fluid Flow Metrics considered include:

- Velocity/flow rate changes due to pipe area differences
- Pressure loss/head loss due to changes in pipe diameter and fittings
- Reynold's number variation due to changing velocities
- Overall pressure/head loss of pipe loop system

Subtask 19.1.3: Results and Discussion

Computational Fluid Dynamics (CFD) simulations:

Computational fluid dynamic simulations were initiated to investigate the flow dynamics in the chemical loop. Manual calculations of head losses, velocities and turbulence intensities through Reynolds number were conducted. The maximum output flow rate of the single-phase pump was used for baseline calculations. Simulations were conducted using SolidWorks 2020 Flow Simulation module. Simulation results indicating surface pressure contours due to the flow are shown in Figure **110**. Results indicate high pressure in the smaller cross section tubing near the pump.
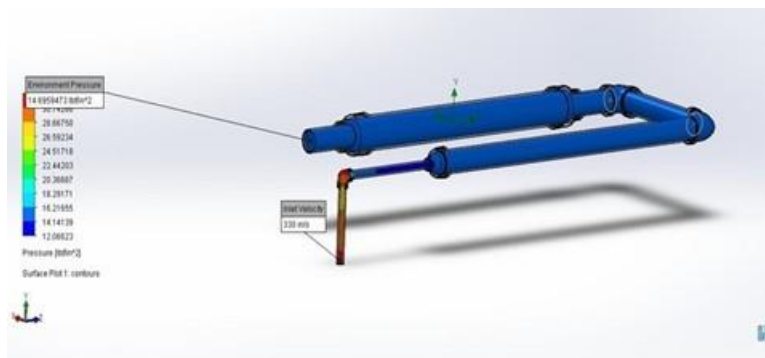
Figure 110. Surface pressure distribution in the bench scale pipe loop.

The next step was to conduct the flow velocity simulations to determine any edits necessary for the loop. Finite Element Method (FEM) based simulations with fine, medium and coarse mesh structures have been conducted. Typical results are shown in Figure **111** and Figure **112** below. Results are indicated at the test section that will house the SRNL coupons. Based on the initial conditions the full flow in the test section is evident: Inlet velocity: 330 in/s, Outlet Pressure: 14.696 lbf/in^2 (atm). These results presented have been simulated with a very fine mesh size to improve accuracy. Simulations have been run at varying mesh sizes, beginning initially with default coarse setting of 3 on a scale of 1-7 and up to a very fine size of 7. Analysis of the velocities across the entire loop in Figure **111** shows that the intensity (velocity) diminishes significantly as the pipe diameter increases. At the ½ inch inlet, a maximum volumetric flow rate of 26 GPM (330

in/s) produced by the pump is observed. Maximum velocity loss occurs at the first expansion from ½ inch to 2 inches and an additional loss at the second expansion from 2 to 3 inches. It is at the second expansion that the flow reaches the test section. This section was closely analyzed with a cut plot in the figures. The plot scale is altered to show how the velocity varies throughout. There is partial recirculation due to the expansion and the top region of the test section experiences higher flow velocity. This is important in understanding how the placement of the coupons in the top and bottom sections of the pipe effect the wear rate. Simulation results also provide the critical regions of pipe loop where changes need to be made in future. The next stage of simulations will include mesh refinement and flow condition variations. Possible addition of solids will also be considered in future.
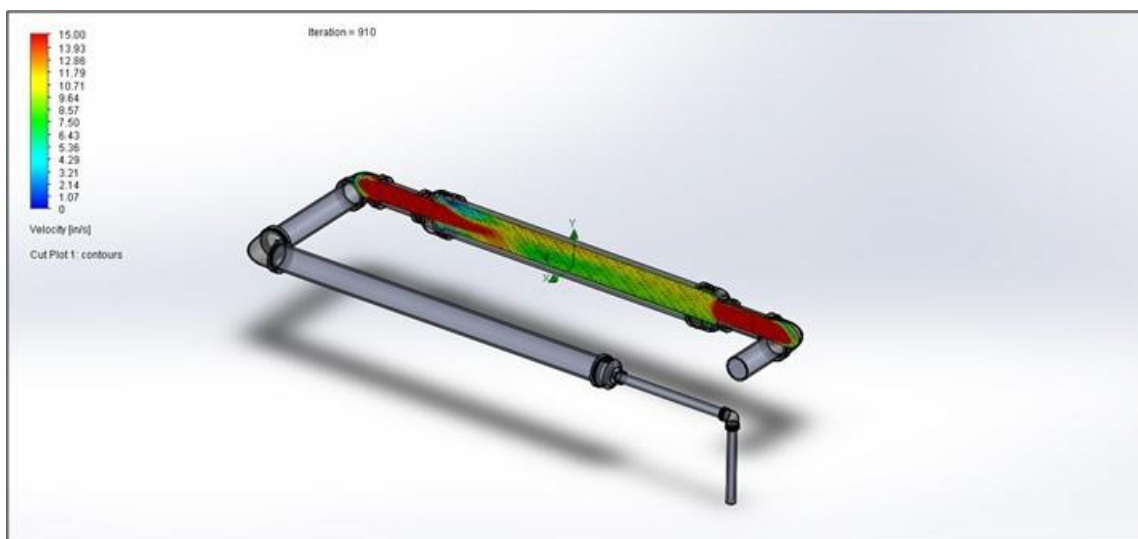
Figure 111. Trimetric view of loop system with velocity cut plot of test section.
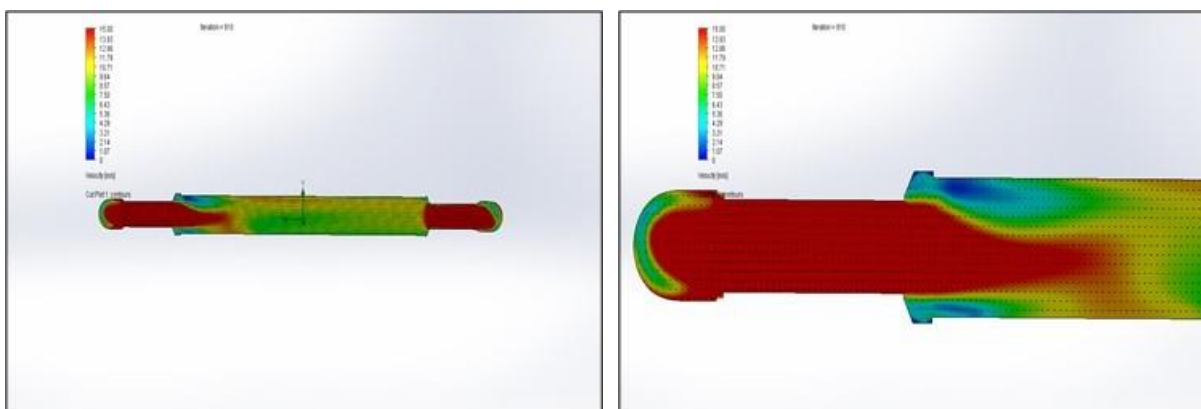
Figure 112. Velocity cut plot - Isolated view of test section (left) and detailed 2–3-inch transition section (right).

Work continued on flow simulations to compare the flow characteristics of both the bench scale loop and the engineering scale loop. Basic models were generated for both loops using routing software. CFD (Flow) simulations were performed using SolidWorks 2020 Flow Simulation Add-in. In Figure **113** and Figure **114** the first CFD iteration of a portion of the engineering scale loop is shown. The values used in the simulation are based on the volume flow rate of the pump. At the

inlet, atmospheric pressure condition is assumed. The figures show velocity contours for the loop and concentrated profiles at various bends from the inlet to the exit. Per results in the figure, it is evident that the velocity is highest at the elbows/bends.
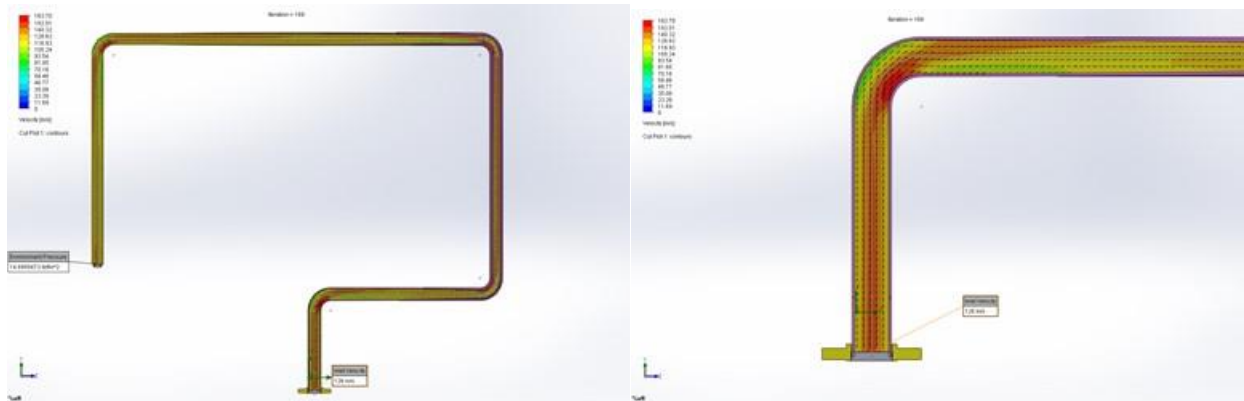
Figure 113. CFD simulation of the engineering scale loop (left) and inlet bend velocity contours (right).
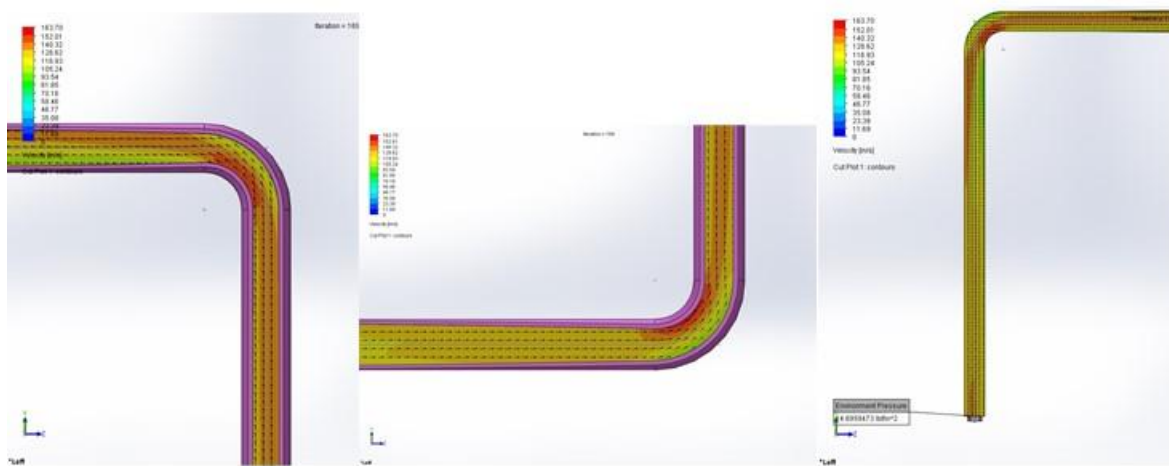
Figure 114. Velocity profile at various bends of the engineering scale pipe loop.

The physical loop has many fittings throughout that affect the flow but in our initial models, these were neglected in order to obtain baseline data. Additional work is planned to make the model closer to the actual loop. FIU will also move from simulating flow of water in the model to multi-phase flows with liquid and solid flows.

For particle erosion, COMSOL Multiphysics software's CFD module was also investigated for its suitability to use with multi-phase flows. For 2-phase flow with sand and water mixture in a pipe, COMSOL will need the particle tracing module. The model developed will simulate flow in a pipe with water and solid particles. An example initial model developed will consist of two straight cylindrical pipe sections, each 50 cm in length and 20 cm in diameter. The straight sections connect via a 90° bend with 50 cm radius of curvature. The pipe inlet velocity is 20m/s and fluid (water) is treated as an incompressible fluid. The solid particles (replicating sand) are transported at a rate of 0.6kg/hr and have a diameter of 0.17 mm. The flow is turbulent with Reynold's number Re =

3.96 x 106 and hence a turbulent model with wall functions can be used which is called the k-w model for strong streamline curvature. A structured boundary layer mesh will be used to optimize the computational cost. The sample images of the results with exemplar flow velocity streamlines and particle trajectories are shown in Figure **115** and Figure **116** [1].
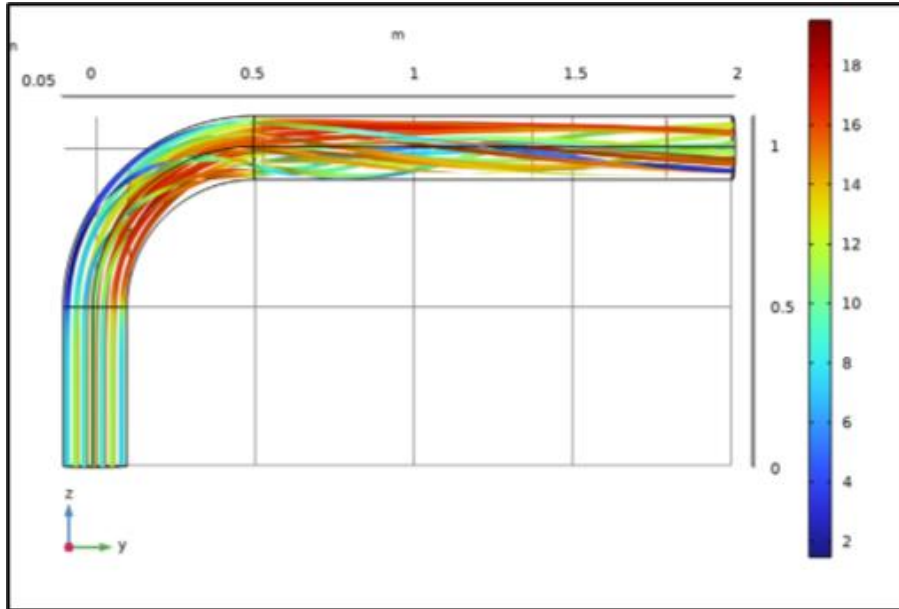
Figure 115. Fluid flow velocity streamlines near the bend.
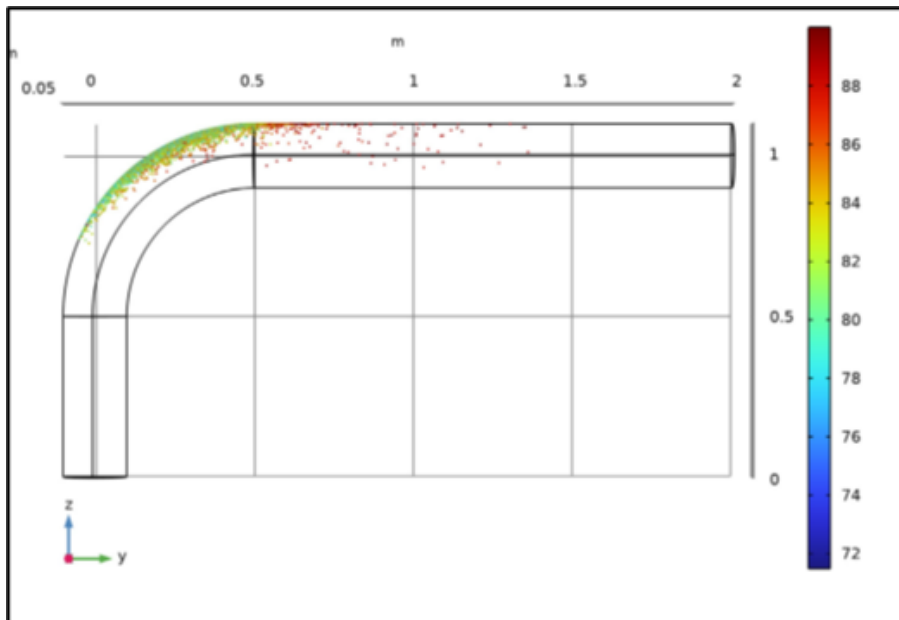
Figure 116. Solid particle trajectories with concentrations near the elbow [1].

Next, the software options available for modeling the fluid flow coupled with particle erosion and caustic corrosion were investigated. A total of 3 software solutions were down selected. These are ANSYS Fluent with Erosion module, Solidworks-Flow simulation with particle erosion, and finally COMSOL with fluid flow simulation, chemical corrosion and erosion and particle tracing modules. Based on the information obtained, it is concluded that COMSOL Multiphysics software has the capability to combine all the three models needed for the pipeline erosion, corrosion, and

particle flow simulations. Currently, FIU is investigating the feasibility of procurement options to continue with modeling and simulations.

Data Analytics - Machine Learning Model Development

Additional work was conducted on the development of machine learning models were investigated to assist in classifying the coupon corrosion image data, to determine the onset and progress of corrosion. This will assist in being able to fully automate classification of corrosion based on the images gathered in the static chemical tests. An initial machine learning model was developed for corrosion detection in carbon and stainless-steel materials. The model was based on applied neural networks. A database of about 500 images (with and without corrosion) was created. The methods of binary image classification and image augmentations were used for accurate model training, validation and prediction. A basic convolutional neural network (CNN) model resulted in an average accuracy of 0.875. The accuracy and validation (real and predicted) values are shown in Figure **117**. It is evident that the model was able to predict the corrosion with reasonable accuracy.
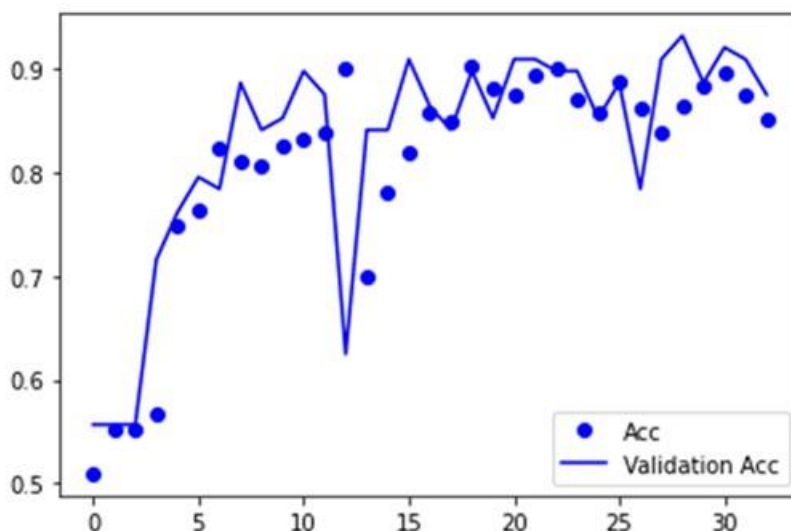
Figure 117. Corrosion prediction accuracy results using the developed CNN machine learning model.

The next phase of research in machine learning included testing of the model(s) to see how the variety of different filters effect an image. In CNN instead of neurons, filters are used that are meant to extract information based on the images. Each of the different filters can be applied for edge detection that defines the edges of an image. There are numerous ways to apply this using spatial transforms, on an image, such as Sobel or Kirsch algorithms. Figure **118** shows an example of edge detection using CNN filters. Other types of Transforms can help an image by reducing the amount of noise by blurring the image. Figure **119** shows noise reduction on a coupon using the blurring technique. These techniques are used as steps to accurately predict the corrosion in coupons.
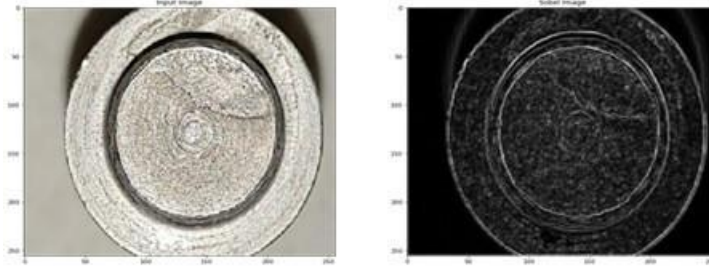
Figure 118. Edge detection on a coupon surface image.
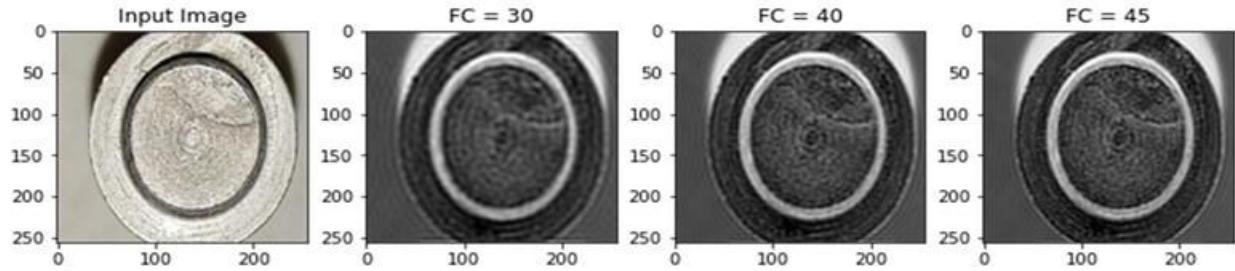
Figure 119. Noise Reduction on a coupon.

Additionally, a brief literature review was conducted to supplement the existing report based on the current results for flow-dynamics based corrosion in metal pipes. Data analytics have been used in literature to detect pipe anomalies, defect location, misalignment, and erosion-corrosion. One of the significant works [2] uses classification-based machine learning methods to differentiate between corroded and non-corroded images. The model is developed using previously collected images (experimental or simulated) of both corroded and non-corroded objects (surfaces). In this process, the images are cropped for resolution and thus increasing the size of the database. This results in a more accurate model development. Next the model is trained and used to predict the newly obtained images to automate the corrosion detection process in real-time. A sample image data set of this process is shown in Figure **120** which shows an example of corrosion damage detection and recognition using convolution neural networks for a ship hull structural plate [2]. Currently, FIU is working on enhancing the model and developing advanced models to further improve the accuracy of classifying the coupon corrosion.
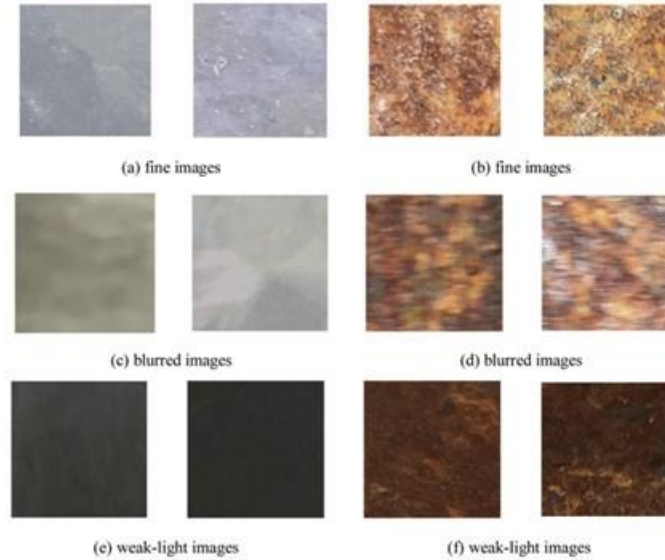
Figure 120. Non-corrosive (grey/black) and corrosive (brown) image classification [2].

Subtask 19.1.3: Conclusions

This task is recently initiated and has the objective to develop a procedure to utilize the UT data (thickness/erosion) and the visual image data (corrosion) along with the simulated data to automatically detect pipeline erosion and corrosion with minimum to no supervision by the human operators. For this, the dynamics of pipe flow are being investigated using various software. Machine learning-based data analytics models are also being studied for erosion and corrosion-based damage detection and prediction. CFD simulations with 3 different software are initiated and ML models are being developed for erosion and corrosion detection.

Subtask 19.1.3: References

1. https://www.comsol.com/particle-tracing-module
2. Y. Yao, Y. Yang, Y. Wang, and X. Zhao, "Artificial intelligence-based hull structural plate corrosion damage detection and recognition using convolutional neural network," Appl. Ocean Res., vol. 90, no.1 May, p. 101823, 2019, Doi: 10.1016/j.apor.2019.05.008.

Subtask 19.2: Evaluation of Nonmetallic Components in the Waste Transfer System

Subtask 19.2: Introduction

Nonmetallic materials are utilized in the waste transfer system at the Hanford tank farms; these include the inner hose of the hose-in-hose transfer lines (HIHTLs), Garlock® gaskets and ethylene propylene diene monomer (EPDM) O-rings. These materials are exposed to simultaneous stressors including β and γ radiation, elevated temperatures, caustic supernatant as well as high pressures during normal use. In 2011, the Defense Nuclear Facilities Safety Board recommended to the U.S. Department of Energy (DOE) to conduct post service examination of HIHTLs to improve the existing technical basis for component service life. Suppliers of the nonmetallic components often

provide information regarding the effects of some of the stressors, but limited information is available for simultaneous stressor exposure.

An extensive test plan was developed by Sandia National Laboratories to understand the simultaneous effects of the aforementioned stressors [1]; however, this test plan was never executed. Additional studies conducted by Lieberman provide information on HIHTLs at elevated temperature and pressure, but little information is gained regarding the synergistic effects with the caustic supernatant [2]. Florida International University (FIU) has been tasked with supporting this effort by conducting multi stressor testing on typical nonmetallic materials used at the Hanford tank farms. Previous years' research efforts focused on evaluating the aging behavior of EPDM by exposing samples of HIHTLs as well as EPDM dog-bone shaped specimens to a 25% sodium hydroxide (NaOH) solution at (100°F), operating (130°F) and design temperatures (170°F) for 6 months and 12 months. In addition, HIHTL and the EPDM dog-bone specimens were also exposed to only hot water at 170°F for a duration of one year. After analyzing the data from the previous phase, it became apparent that the synergistic effects of NaOH with high temperature had a significant effect on the degradation of the specimens. After discussing the findings with the site engineers, it was decided to conduct additional aging of HIHTL and EPDM dog-bone specimens at various concentrations of NaOH as well as water only at the elevated temperatures. Four test loops were developed at FIU allowing for the aging of HIHTL as well as dog-bone specimens utilizing 6.25%, 12.5% and 25% NaOH and water only at 170°F for a duration of one year. After aging, the test specimens had their material properties measured and compared to the baseline (unaged) values. This report presents the results of the material property tests of the specimens that were aged with 6.25%, 12.5% and 25% NaOH and water only at 170°F for a duration of one year.

Subtask 19.2: Objectives

In order to reinforce the findings from the previous phase of testing, HIHTL coupons as well as EPDM material coupons were used to run additional aging experiments. FIU engineers worked with Hanford personnel to develop experimental combinations that involve aging HIHTL and EPDM material coupons for one-year utilizing sodium hydroxide at concentrations of 6.25%, 12.5% and 25% at 170°F as well as water only at 170°F. Comparing the results of this testing with previous data will provide a better understanding of how the elevated temperature and the sodium hydroxide affect the material properties of the components.

Subtask 19.2.1: Phase 2 of HIHTL coupons

Aging of HIHTL coupons has been completed.

Subtask 19.2.2: Material and Mechanical Testing for HIHTL

Subtask 19.2.2: Methodology

In order to perform this research, four sets of HIHTLs as well EPDM dog-bone specimens were aged in four aging test loops that utilized sodium hydroxide at concentrations of 6.25%, 12.5% and 25% at 170°F as well as water only at 170°F, respectively, as the circulating solution. After aging, the material properties of the specimens were measured and will be compared to the values of the baseline (unaged) specimens. The material properties measured included the burst pressure of the HIHTL specimens, the tensile strength of the EPDM dog-bones, and scanning electron microscopy (SEM) analysis of both HIHTL and dog-bone specimens.

Burst Pressure Testing

Figure 121 shows an image of the HIHTL burst pressure test apparatus with the acrylic safety cover removed. The test apparatus consists of a hydraulic pump, pressure gauge, and a pressure transducer with a range of zero to 48 MPa with an accuracy of 0.25% of full-scale output.

.
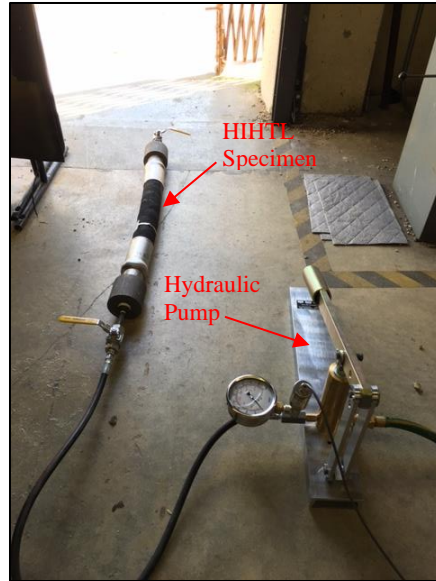
Figure 121. HIHTL burst pressure test apparatus.

Tensile Strength Testing

Figure 122 shows an image of the tensile strength test apparatus. The tensile strength test apparatus consists of an MTS Criterion™ Model 43 tensile testing machine with a force accuracy of ± 0.5% of the applied force.
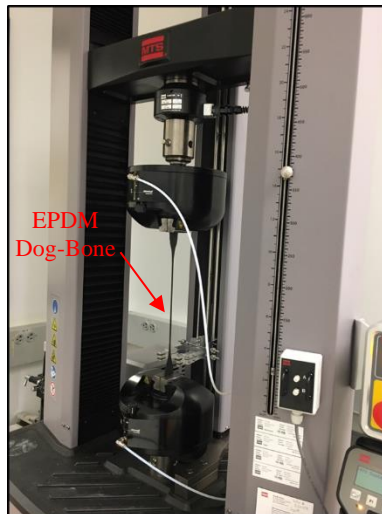
Figure 122. Tensile strength test apparatus.

Scanning Electron Microscopy (SEM) Analysis

Figure 123 shows an image of the Joel SM-F100 Schottky Field Emission Scanning Electron Microscope used to perform scanning electron microscopy (SEM) analysis on the specimens.

Figure 123. Joel SM-F100 Schottky Field Emission Scanning Electron Microscope.

Subtask 19.2.2: Results and Discussion

Burst Pressure Testing Results

Figure 124 shows the results of burst pressure tests on the hose specimens. As can be seen from the figure, the greatest degradation of burst pressure occurred at the lowest concentrations of NaOH with hoses aged with hot water only having the greatest degradation.
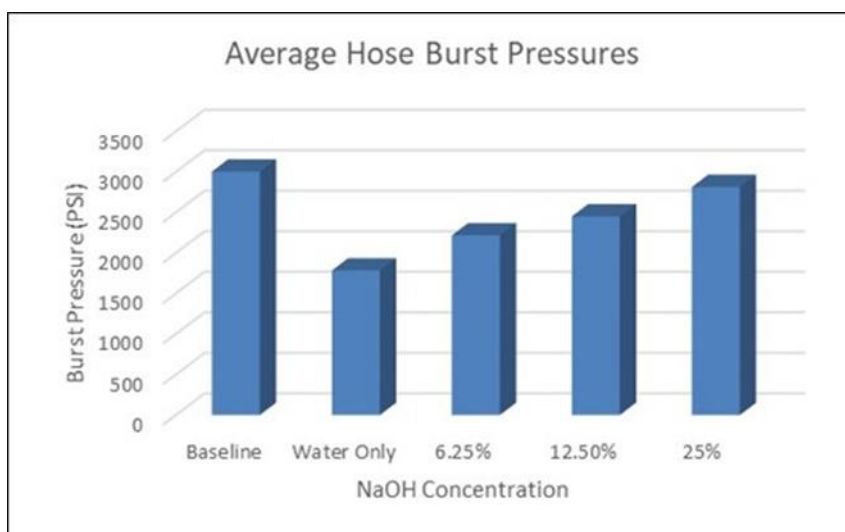
Figure 124. Average hose burst pressures.

Two different types of failures were observed during the tests, internal failure and rupture. Figure 125 and Figure **126** show a rupture and an internal-type failure respectively.

Figure 125. A rupture hose failure.

Figure 126. Internal hose failure.

Tensile Strength Testing Results

Figure 127 shows the results of the tensile strength tests. As with the hose results, the greatest degradation occurred at the NaOH concentration of 6.25%.
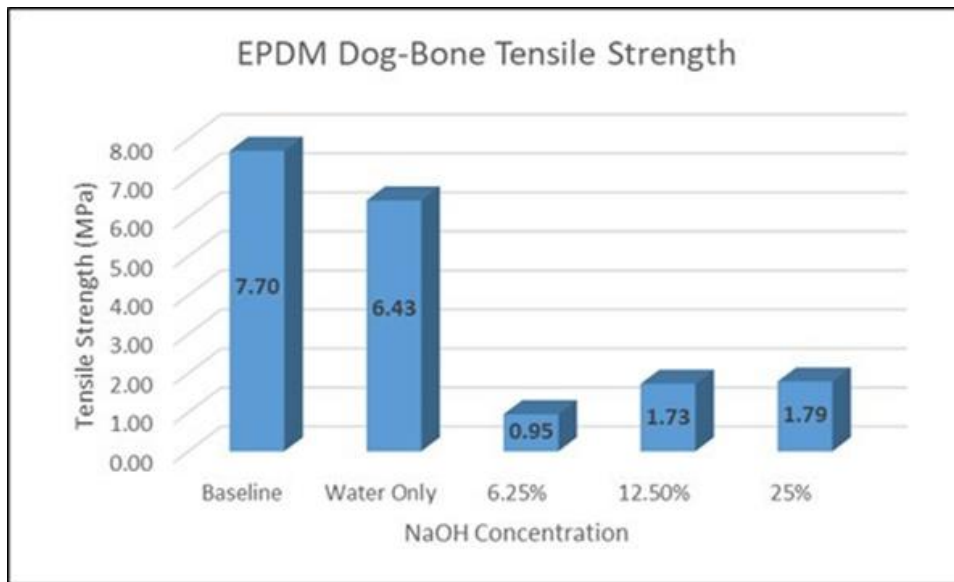
Figure 127. Average dog-bone tensile strength results.

Figure 128 thru Figure 131 show the stress-strain curves for the dog-bones aged in water-only, 6.25%, 12.5%, and 25% NaOH concentration solutions respectively.
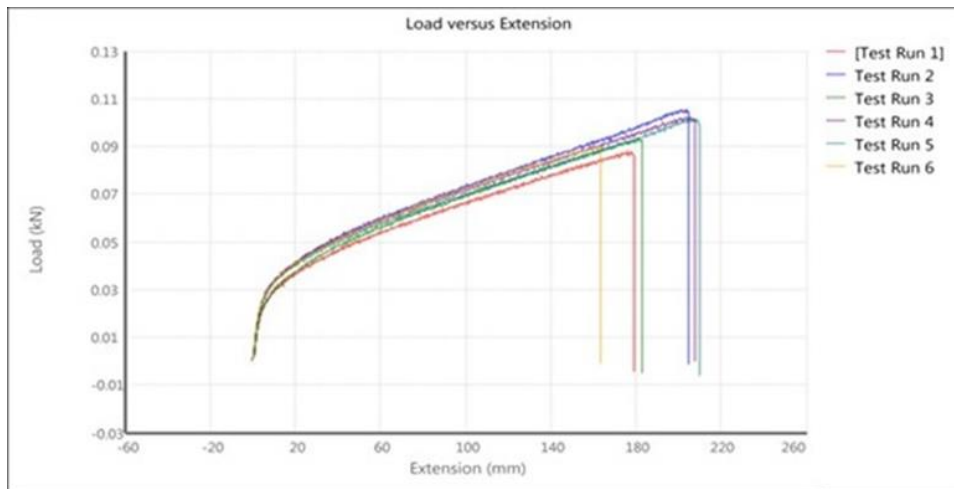
Figure 128. Water only tensile results.
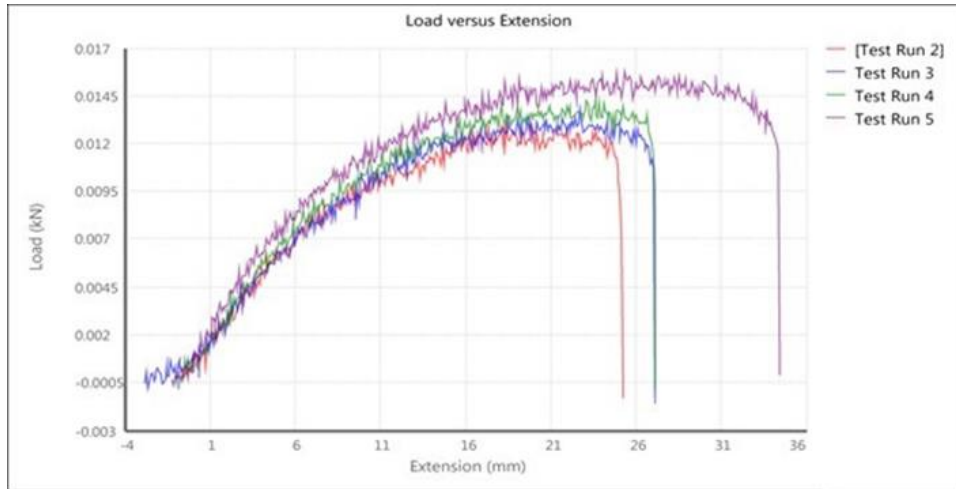
Figure 129. 6.25% NaOH tensile results.
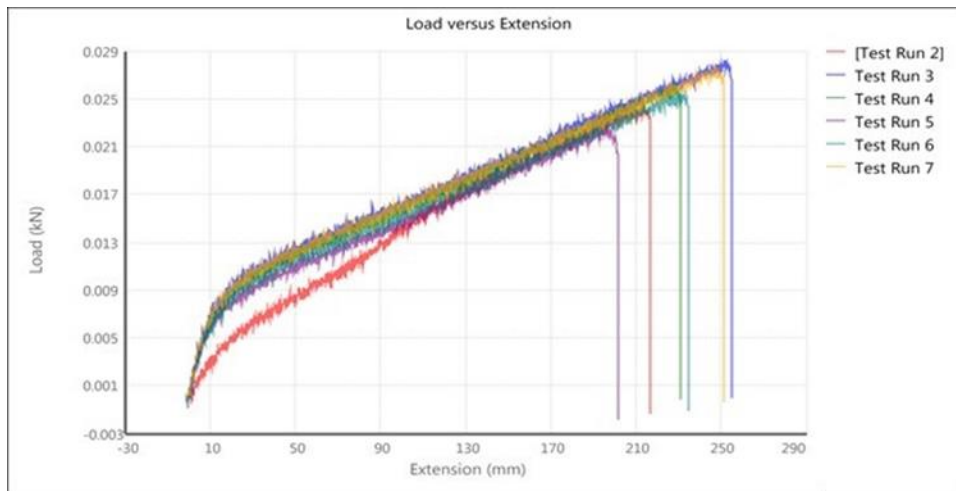
Figure 130. 12.5% NaOH tensile results.
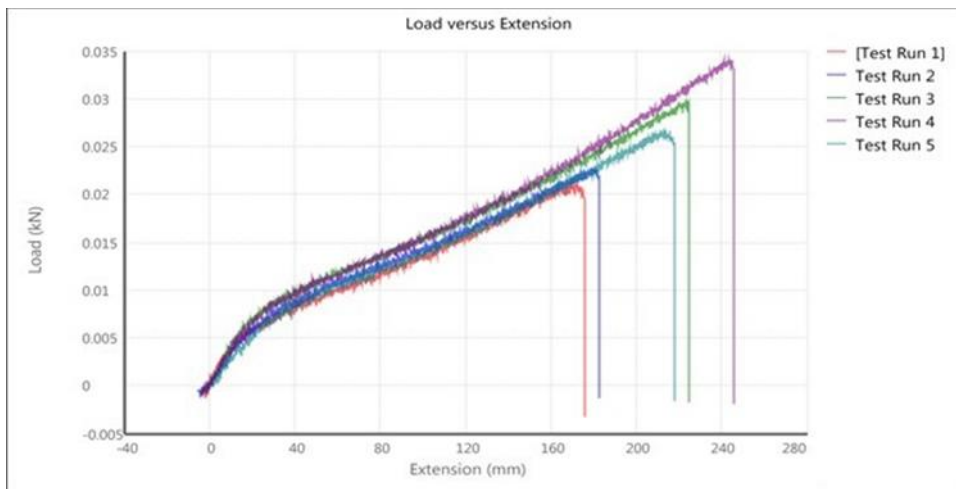
Figure 131. 25% NaOH results.

Scanning Electron Microscopy (SEM) Analysis

Dog-Bone Specimens

Scanning electron microscopy (SEM) analysis was conducted on the aged EPDM dog-bone specimens. Figure 132 thru Figure 136 show the SEM scans of the baseline (unaged) specimen, and the specimens aged with water only, 25% NaOH, 12.5% NaOH, and 6.25% NaOH at 170°F. The amount of material degradation observed is in good agreement with the amount of degradation in tensile strength. When compared to the tensile strength of the baseline specimen, the tensile strength of the specimens aged with water-only, 25% NaOH, 12.5% NaOH, and 6.25% NaOH had a tensile strength that was 16.49%, 76.75%, 77.53%, and 87.66% respectively less than the baseline value. Figure 127 shows these results graphically.
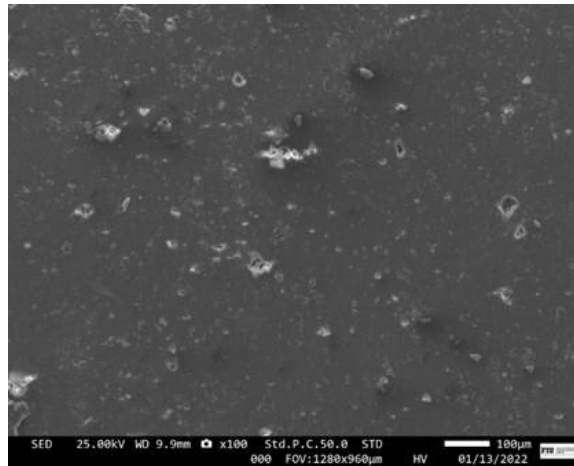
Figure 132. SEM scan of baseline (unaged) dog-bone specimen @ 100X magnification.
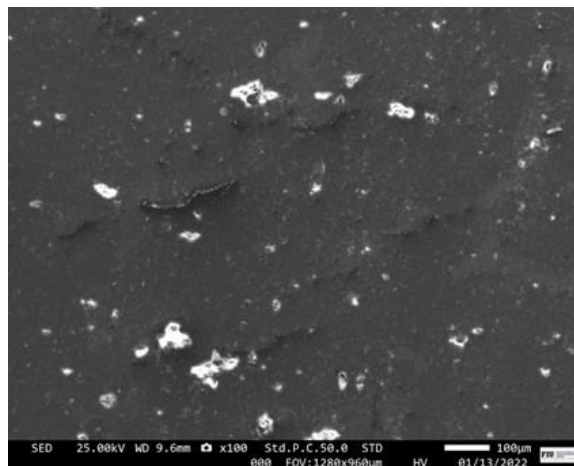
Figure 133. SEM scan of dog-bone specimen aged with water-only at 170°F @ 100X magnification.
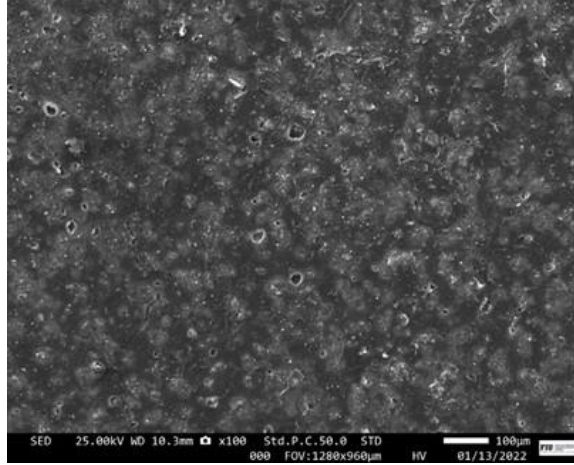
Figure 134. SEM scan of dog-bone specimen aged with 25%-NaOH at 170°F @ 100X magnification.
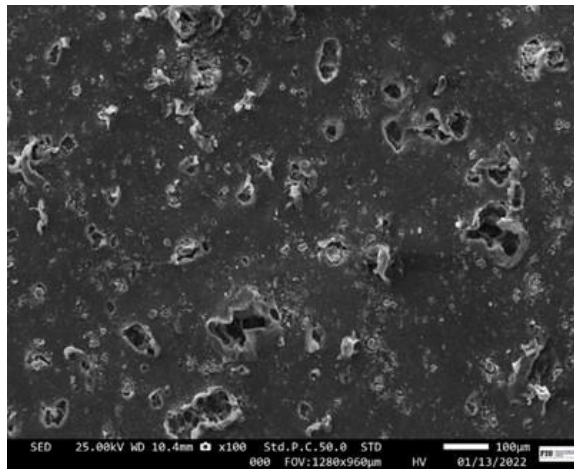
Figure 135. SEM scan of dog-bone specimen aged with 12.5%-NaOH at 170°F @ 100X magnification.
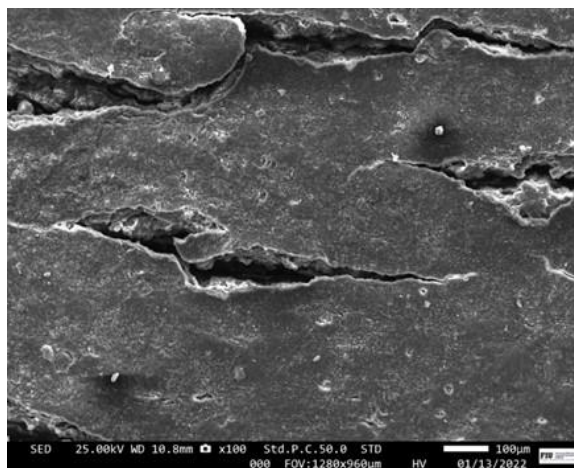
Figure 136. SEM scan of dog-bone specimen aged with 6.25%-NaOH at 170°F @ 100X magnification.

HIHTL Specimens

SEM analysis was also conducted on specimens cutout of the aged HIHTL. Figure 137 shows the scan of the inside of a baseline (unaged) hose, while Figure 138 shows the scan of the inside of a base hose aged with water only at 170°F. Figure 139 thru Figure 141 show the scans of the insides of hoses aged with 6.25%, 12.5%, and 25% concentration NaOH solutions at 170°F. Of the specimens aged with NaOH solution, the specimen aged with the 6.25% NaOH concentration had the greatest degradation, while the specimen aged with the 25% NaOH solution had the least degradation.
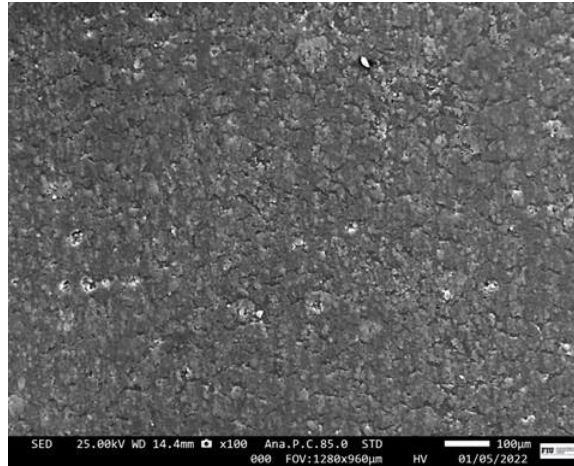
Figure 137. SEM scan of the inside of a baseline (unaged) hose.
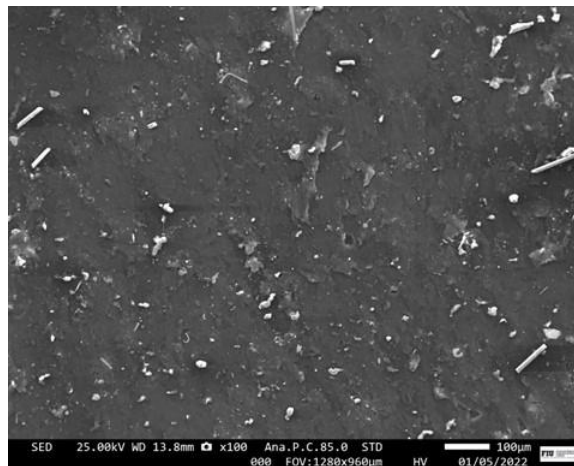
Figure 138. SEM scan of the inside of a hose aged with water only at 170°F.
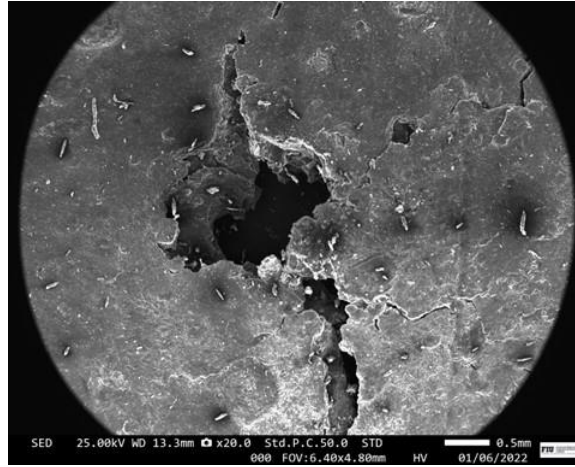
Figure 139. SEM scan of the inside of a hose aged with 6.25% NaOH at 170°F.
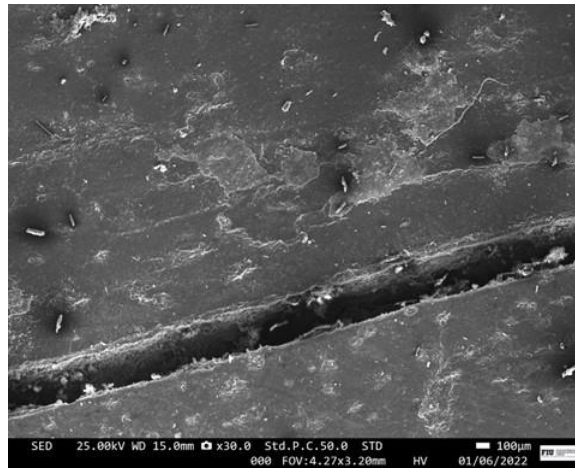
Figure 140. SEM scan of the inside of a hose aged with 12.5% NaOH at 170°F.
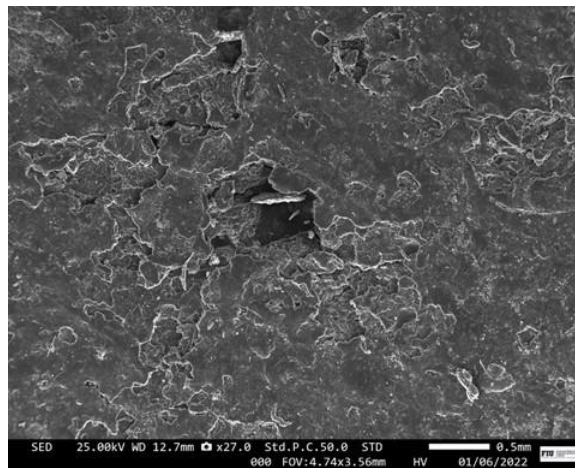
Figure 141. SEM scan of the inside of a hose aged with 25% NaOH at 170°F.

Scanning Electron Microscopy with Energy-Dispersive X-Ray Spectroscopy (SEM-EDX) Analysis

Scanning Electron Microscopy with Energy-Dispersive X-ray Spectroscopy (SEM-EDX) analysis was conducted on the EPDM dog-bone specimens aged with NaOH concentrations of 6.25%, 12.5%, and 25.0%. Analysis was conducted at a cross section of the narrow part of each dog-bone to determine the amount of sodium (Na) that had penetrated into the material. Figure 142 through Figure **145** show the results of this analysis.
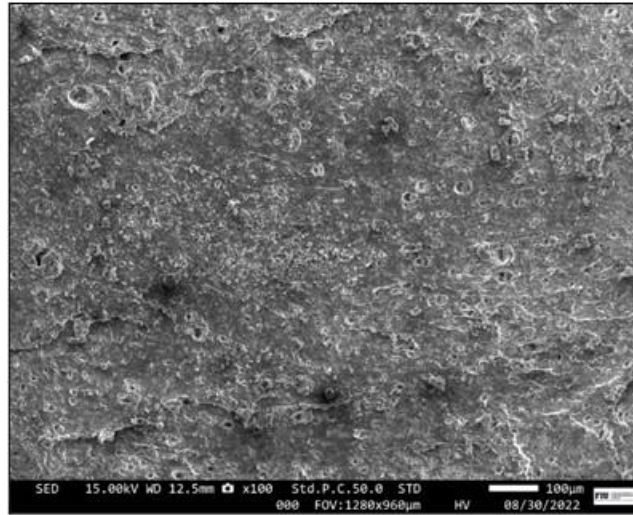
Figure 142. SEM image of dog-bone cross section aged with 25% NaOH (100X magnification).
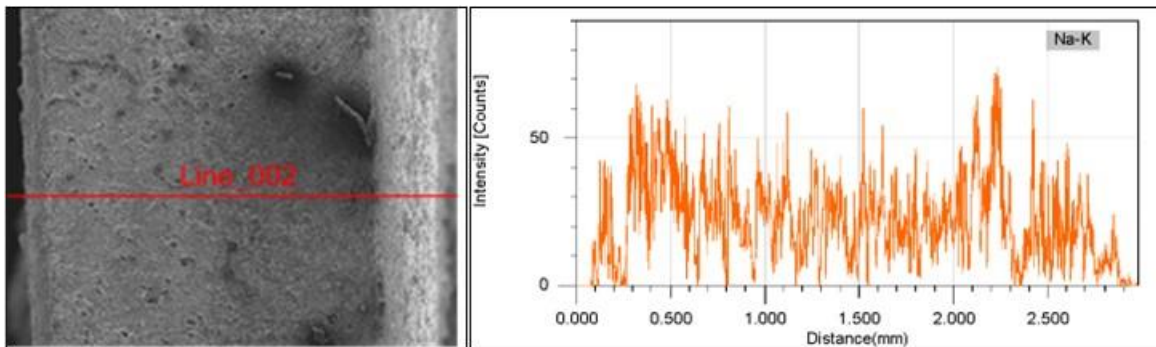
Figure 143. SEM-EDX analysis of a dog-bone aged with 12.5% NaOH solution.
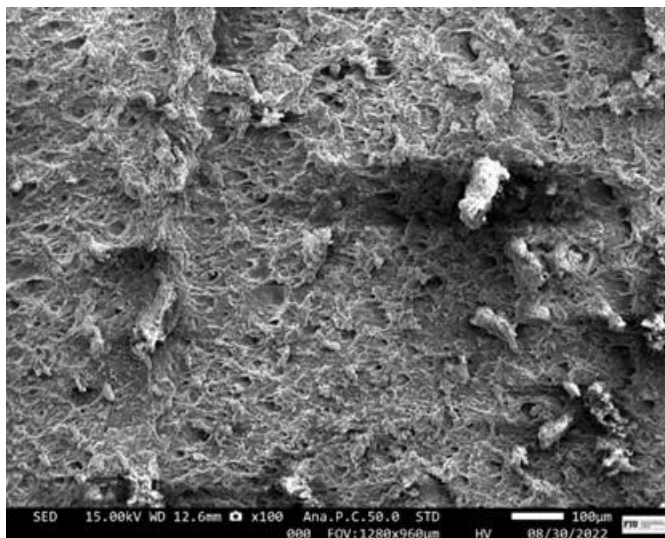
Figure 144. SEM image of dog-bone cross section aged with 6.25% NaOH (100X magnification).
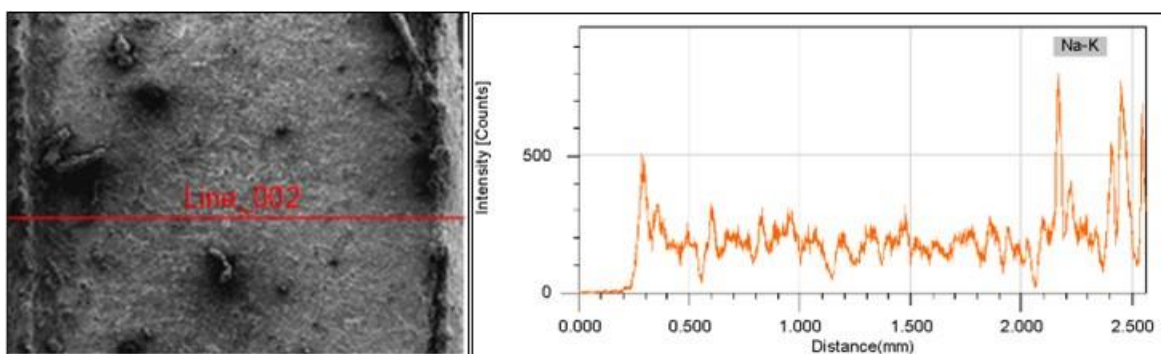
Figure 145. SEM-EDX analysis of a dog-bone aged with 6.25% NaOH solution.

Analysis of the results showed that the greatest amount of material degradation as well as sodium penetration occurred in the specimens aged with the 6.25% NaOH solution, while the specimens aged with the 12.5% and the 25% solutions had less material degradation and had lower but similar sodium penetrations. This is in good agreement with the tensile strength results for these specimens. The greatest degradation in tensile strength occurred with the specimens aged with 6.25% NaOH solution which had an 88% degradation in strength. The specimens aged with 12.5% and 25% NaOH solutions had a degradation in tensile strength of 78% and 77% respectively.

Material Surface Porosity and Roughness Analysis

Dog-Bones

Material surface porosity and roughness analysis on the dog-bone specimens aged with NaOH concentrations of 6.25%, 12.5%, and 25.0% as well as specimens aged with water only. ImageJ software was utilized for the analysis and the results showed that when compared to the baseline (unaged) dog-bones, the surface roughness (Ra) for the dog-bones aged with 6.25%, 12.50%, 25.00% NaOH, and water only increased by 325%, 213%, 181%, and 50% respectively. In addition, the porosity (% area) for the dog-bones aged with 6.25%, 12.50%, 25.00% NaOH, and water only increased by 869%, 416%, 349%, and 56% respectively. This corresponds well with the tensile strength test results where the degradation of material strength increased as the NaOH concentration decreased. Figure 146 thru Figure **150** show ImageJ scans of the dog-bone specimens

aged with NaOH concentrations of 6.25%, 12.5%, and 25.0% water only, and baseline dog-bone specimens.
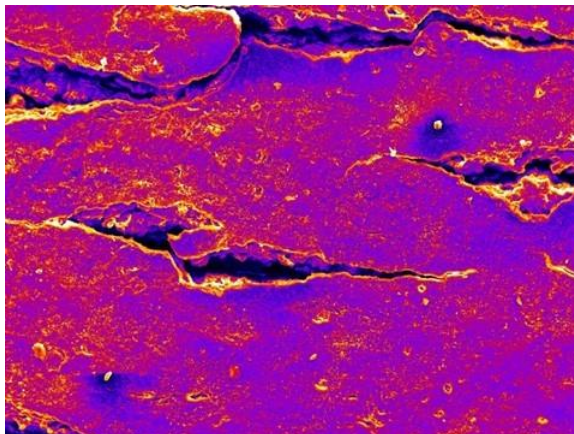
Figure 146. ImageJ scan of dog-bone aged with 6.25% NaOH (100X magnification).
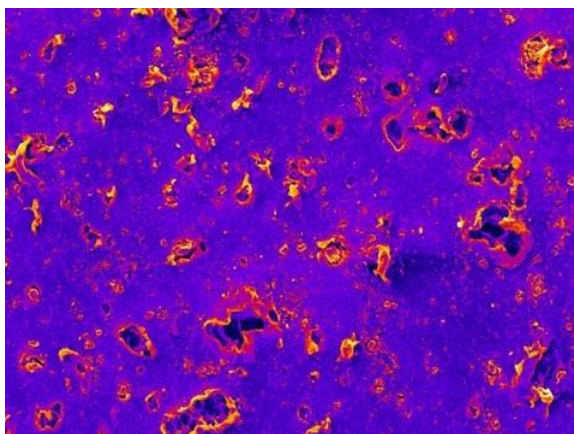
Figure 147. ImageJ scan of dog-bone aged with 12.5% NaOH (100X magnification).
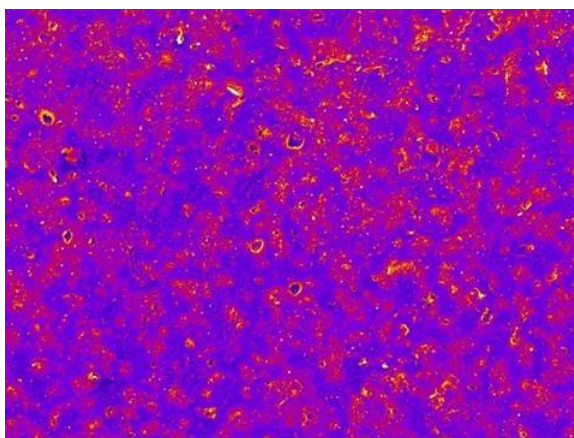
Figure 148. ImageJ scan of dog-bone aged with 25% NaOH (100X magnification).
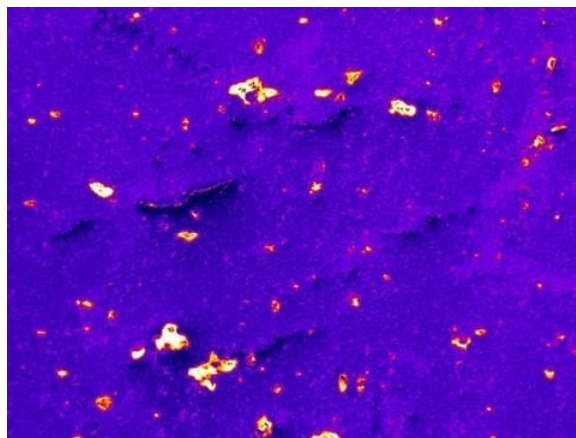
Figure 149. ImageJ scan of dog-bone aged with hot water (100X magnification).
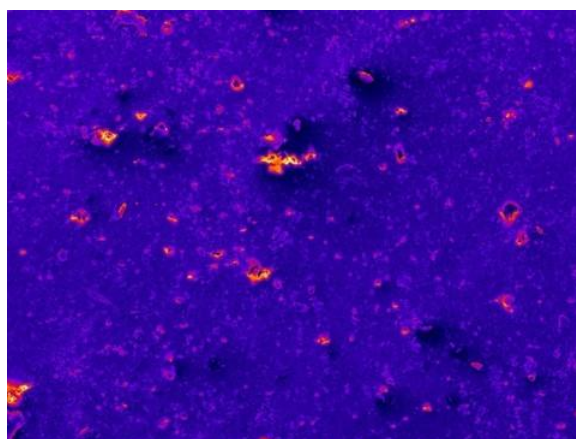
Figure 150. ImageJ scan of baseline (unaged) dog-bone (100X magnification).

HIHTL

ImageJ software was also utilized to analyze the surface roughness and the porosity of the HIHTL specimens. Figure 151 shows an ImageJ image of a baseline HIHTL specimen and Figure 152 thru Figure 155 show ImageJ images of the insides of the HIHTL specimens aged with water only, 6.25%, 12.5%, and 25% NaOH at 170°F. As shown in Table 10, when the surface roughness (Ra) of the HIHTL specimens aged with 6.25%, 12.50%, 25.00% NaOH, and water only were compared with the baseline value, a 99%, 85%, 81%, and 8% increase in roughness was observed, respectively. In addition, when the porosity of the HIHTL specimens exposed to 6.25%, 12.50%, 25.00% NaOH solutions, and water only were compared to the baseline value, porosity increases of 384%, 294%, 162%, and 32% were observed, respectively. This is in good agreement with the burst pressure results as well as the roughness and porosity results of the dog-bone specimens.

Table 10. HIHTL Surface Roughness and Porosity

Sample	Surface roughness (Ra)	Change (%)	Porosity	Change (%)
Baseline (Unaged)	10.77	0	5.31	0
Water only	11.63	8	7.04	32
6.25% NaOH	21.39	99	25.70	384
12.50% NaOH	19.89	85	20.92	294
25.00% NaOH	19.43	81	13.91	162
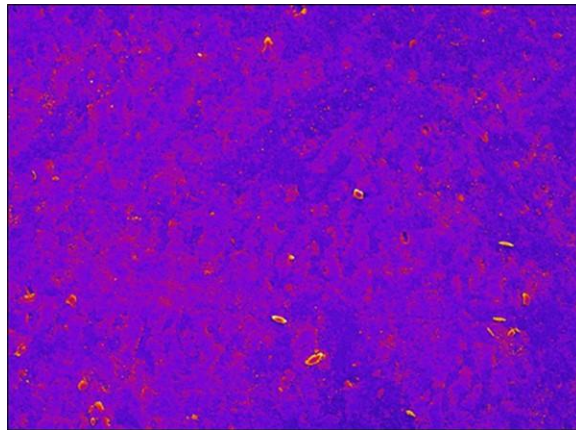
Figure 151. ImageJ image of the inside of a baseline HIHTL.
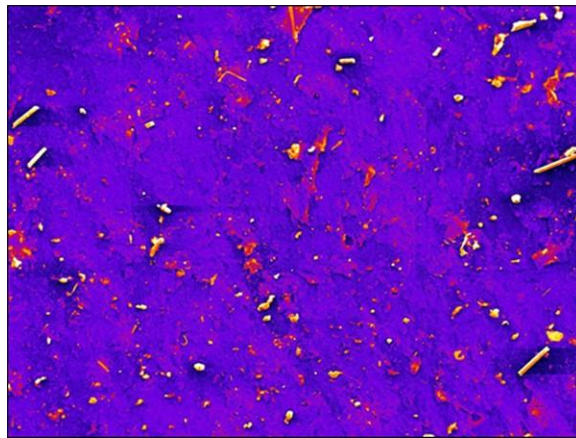
Figure 152. ImageJ image of the inside of a HIHTL aged with water @ 170°F.
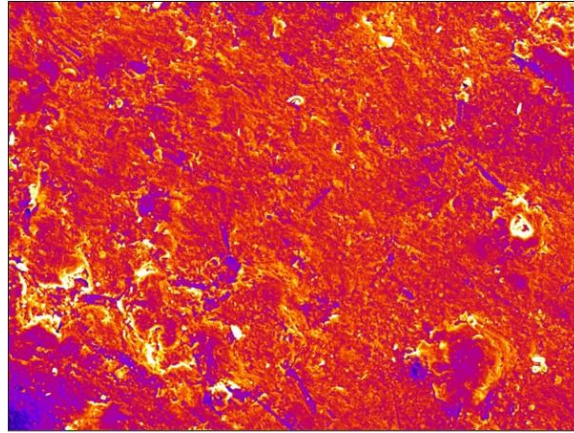
Figure 153. ImageJ image of the inside of a HIHTL aged with 6.25% NaOH @ 170°F.
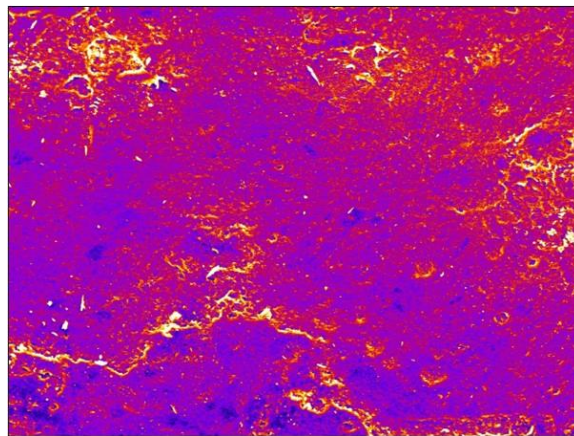
Figure 154. ImageJ image of the inside of a HIHTL aged with 12.5% NaOH @ 170°F.
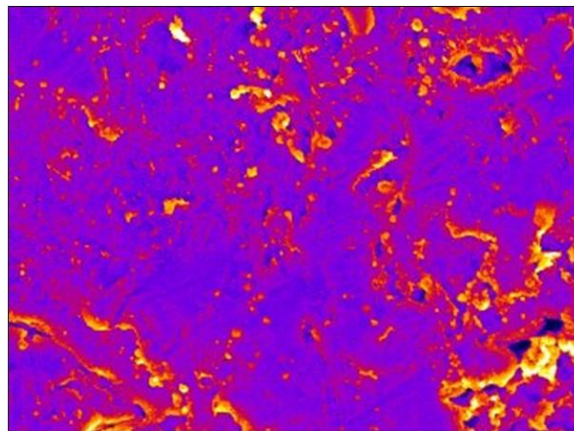
Figure 155. ImageJ image of the inside of a HIHTL aged with 25.0% NaOH @ 170°F.

Subtask 19.2.2: Conclusions

This year's research concentrated on the effect of solution concentration on the degradation of the HIHTL used in caustic liquid waste transfer lines at the Energy's Hanford Site Tank Farm. During waste transport, the inner hose of the HIHTL is exposed to caustic solutions at high temperatures and high pressures, as well as β and γ radiation. The experiments conducted at constant temperature (170°F) with solution containing 0.00 to 25.00% NaOH showed that greatest deterioration of the HIHTL occurred in solutions with the lower NaOH concentrations. The HIHTL samples exposed to solutions with the 25.00% NaOH had an average reduction in burst strength of 6% when compared to the baseline specimens, while the specimens exposed to the solutions with 12.5, 6.25, and 0.00% NaOH (i.e., water only) had burst pressure reduction of 18, 26, and 41%, respectively.

Even though the samples exposed to water only had the most significant reduction in burst pressure, all failures of the HIHTL aged with water only were due to internal hose failures rather than ruptures. Similar to the HIHTL specimens, for the EPDM dog-bone samples, the highest loss of tensile strength occurred for the samples that were exposed to solutions with the lowest NaOH concentration. When compared to the baseline value, the tensile strengths of the dog-bone samples were reduced by 87%, 77%, and 76% when exposed to solutions of 6.25, 12.50, and 25.00% NaOH, respectively. The specimens exposed to only hot water had 15% reduction in tensile strength.

Except for the samples that were exposed to water only, these results of the dog-bone samples are similar to those obtained from the HIHTL burst pressure testing. The microscopic examination of the hose and dog-bone specimens showed that the specimens exposed to the 6.25% NaOH solution had the highest deterioration while the specimen exposed to the 25.00% NaOH solution had the least deterioration. Both hose and dog-bone specimens exposed to water only showed minimal deterioration. The extent of deterioration to the inner surface of the HIHTL increased and the burst pressure decreased as the NaOH concentration decreased. Even after one year of exposure where approximately 6-million gallons of solution was pumped through the hoses, the minimum burst pressure still had a factor of safety greater than four.

The next phase of testing will focus on determining the extent of chemical interactions causing deterioration on the HIHTL and dog-bone samples at lower NaOH concentrations in comparison to those occurring at higher NaOH concentrations.

Subtask 19.2.2: References

1. Brush, LH., Ottinnger Farnum, C., Dahl, M., Joslyn, CC., Venetz, TJ. (2013). Test Plan for the Irradiation of Nonmetallic Materials. Albuquerque, New Mexico: Sandia National Laboratories, Albuquerque, NM.

TASK 20: CORROSION PROTECTION AND CHARACTERIZATION OF EM INFRASTRUCTURE

Subtask 20.1: Evaluation of Coatings for the H-Canyon Exhaust Tunnel

Subtask 20.1: Introduction

The H-Canyon is the only remaining chemical processing facility in America capable of reprocessing plutonium, highly-enriched uranium and other radioactive materials. The H-Canyon Exhaust (HCAEX) Tunnel used to contain and direct the exhaust air flow from the canyon chemical process areas to the sand filter system, where radioactive contamination is removed. After several structural integrity inspections of the HCAEX tunnel, mandated by mission requirements at the Savannah River Site, there is a great concern about the concrete structure degradation. Videos/pictures taken during inspections evidenced significant degradation of the interior concrete walls characterized by surface erosion exposing concrete coarse aggregates, rebars exposed in some tunnel sections and significant amount of concrete loss, all promoted by the aggressive environment inside the tunnel (primarily nitric acid vapors).

Subtask 20.1: Objectives

The objective of this task is to investigate protective coatings that can be used to mitigate and prevent further degradation of concrete walls exposed to the adverse environments in the HCAEX tunnel. Potential coatings will be applied on aged and non-aged concrete surfaces similar to the tunnel degraded walls and further evaluated through accelerated aging tests at the laboratory. A preliminary coating selection will be performed based on research findings. FIU initiated communications with various coating companies to identify and prepare a list with the potential coating options for the evaluation stage. Also, a comprehensive test plan for the evaluation of the coating options was prepared. In addition, concrete specimens with raw materials and mix design similar to the tunnel have been prepared and will be the substrate of the coatings. A group of concrete samples will be aged before coating application. In line with the aforementioned objective, the following subtasks will be executed to support the effort:

- Initiate the evaluation of potential coatings through accelerated aging tests. The accelerated aging conditions will consider the worst-case scenario during the concrete aging experiments. Several variables of importance in the coating performance will be included in the study such as surface preparation, conditions of the surface and others.
- Based on the preliminary results of the coating performance in aggressive environments, each of the coatings will be ranked. For this ranking, the results of various parameters under study will be considered such as visual inspection, adhesion, thickness, and others.

Subtask 20.1.1: Initiate the Evaluation of Coatings through Accelerated Aging Tests

Subtask 20.1.1: Methodology

Based on lessons learned and results of the concrete aging process, the enhanced aging condition was selected for the accelerated aging of the coatings. The enhanced aging conditions consists of exposing the surface of the specimen to a 0.5M nitric acid solution. Once a week, the surface in

contact with the acid solution is exposed to erosion by using a wire brush. This aging procedure combines the chemical and physical effect of the acid solution and the erosion, respectively. Concrete specimens, aged and non-aged and with and without embedded rebar will be used for the bench-scale testing. The abovementioned concrete specimens were the substrate for the evaluation of potential coatings.

Test plan

A factorial design of three variables at two levels was used leading to 8 different experiments. Table 11 below shows the test plan with the experiments for each coating. The single and synergistic effect of the variables were studied. The three variables under study are 1) surface preparation, 2) steel rebar presence and 3) aging of the substrate. Two levels of each variable were studied and represented in the table.

Four potential coatings, from three different manufacturers Belzona, Carboline and Sherwin-Williams, were selected for the study and three of them are under evaluation so far. The coatings include coating systems or a single coating.

A fourth company, Framatome, also showed interest in evaluating one or two of their coatings to protect the tunnel. The coatings' information has been received and FIU is working on the preparation of more concrete samples that will be the substrate of the potential coatings.

Table 11. Test Plan for Accelerated Aging of Coatings

Test ID	Carboline ID	Belzona ID	S-W ID	Aged/Non-aged surface	Surface Preparation (Yes/No)	Steel rebar (Yes/No)
T1	CT1-1*	BT1-1*	ST1-1*	Aged	Yes	Yes
T2	CT2-1*	BT2-1*	ST2-1*	Aged	Yes	No
T3	CT3-1*	BT3-1*	ST3-1*	Aged	No	Yes
T4	CT4-1*	BT4-1*	ST4-1*	Aged	No	No
T5	CT5-1*	BT5-1*	ST5-1*	Non-aged	No	Yes
T6	CT6-1*	BT6-1*	ST6-1*	Non-aged	No	No
T7	CT7-1*	BT7-1*	ST7-1*	Non-aged	yes	yes
T8	CT8-1*	BT8-1*	ST8-1*	Non-aged	Yes	No

ID: identification, *: there are three replicates for each test case and only "No 1" is represented in the table. For example, the replicates for Carboline's T1 case would be CT1-1, CT1-2 and CT1-3, S-W: Sherwin-William samples.

Specimen preparation

Concrete samples of 4-inch diameter and 2-inch height were used as the substrate to evaluate potential coatings. The concrete samples were prepared in a previous stage of the investigation, using a mix design and raw materials similar to the tunnel. Some of the samples were aged through accelerated aging tests and others were not aged for comparative purposes. After the aging process, aged concrete surfaces with protruded coarse aggregates (uneven), exposed rebar (some cases) and chemical damage were obtained. The developed concrete specimens were used as the substrate of the coatings.

The coating companies prepared the surface of selected concrete samples before the coating application. The type of surface preparation was determined by each coating company and may not be the same. Some samples did not receive surface preparation and served as a reference for comparative purposes. The same analysis was done for the samples with and without rebar.

Table 12 below shows the major characteristics of the coatings under study. Belzona company proposed two different coatings, Belzona 4311 and Belzona 1381. Both are single coatings. Only one of the two Belzona's coating, Belzona 4311, is under evaluation so far. The other two companies, Carboline and Sherwin-Williams, proposed coating systems consisting of a resurfacer or repair mortar followed by a coating system (multiple coats). Based on recommendations of Savannah River site engineers, only the coatings without the resurfacer or repair mortar will be evaluated. The surface of the concrete samples was prepared and coated at the manufacturer facilities. Once the applied coatings were cured, samples were sent to FIU laboratories for testing.

Before coating application, some samples received surface preparation, including the group of samples: T1, T2, T7 and T8 (Table 11). For each group, three replicates were prepared. For example, for the T1 group the replicates identification are T1-1, T1-2 and T1-3 (Table 11). The same identification process was done for the rest of the groups. Some of the samples have steel rebar, embedded or exposed, identified as T1, T3, T5 and T7 (Table 11).

Table 12. Potential Coatings for the Accelerated Aging Tests

	Company	Coating	Characteristics
1	Belzona	**Belzona 4311**. *Epoxy coating*	- One coat - Chemical resistant coating, up to 20% nitric acid solutions.
2		**Belzona 1381**. *Epoxy coating*	- One coat - Erosion and chemical resistant coating, up to 10% nitric acid solutions.
3	Sherwin-Williams	1. Repair mortar (<u>optional</u>). **AW Cook Horizontal Pipe Lining Mortar** 2. Prime coat (<u>optional</u>). **Sherwin-Williams Macropoxy 5000 Pre-Prime.** *Epoxy coating* 3. Finish coat. **Sherwin-Williams Envirolastic AR425.** *Polyurea coating*	- Coating system. Multiple coats. - Repair mortar is <u>optional</u>. - Abrasion resistant coating (finish coat)

4	Carboline	1. Resurfacer (<u>optional</u>). **Carbocrete 4010.** *Fiber-reinforced repair mortar* 2. Prime coat. **Dudick Primer 67.** *Moisture-tolerant epoxy primer for steel and concrete.* 3. Tie coat primer. **Dudick Primer 27.** *Vinyl Ester primer for steel and concrete (required as a tie coat)* 4. Vinyl ester lining. **Dudick Protecto-Coat 700/705.** *Flake filled, thermosetting polyester lining*	- Coating system. Multiple coats. - Moisture tolerant primer. - Abrasion resistant coating (finish coat)

Accelerated aging conditions

The enhanced aging consists of exposing the samples (top coated surface) to a 0.5M nitric acid solution (pH = 0.3) for the time of the experiment. Once a week, samples were exposed to erosion using a wire brush. Figure 156 shows the schematic of the test setup developed for the exposure of the coated samples to the acid solution. A similar setup was used to age the concrete surfaces. The test setup was placed inside a fume hood to reduce the risk of operator exposure to nitric acid fumes.
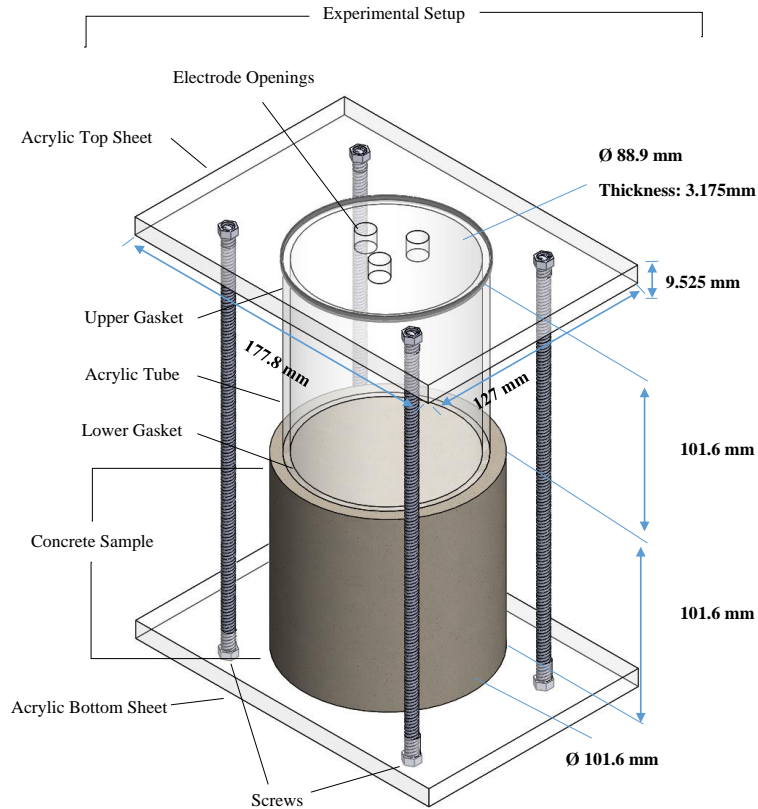
Figure 156. Schematic of test setup for coatings exposure to acid solutions.

The procedure summarized below was followed for the evaluation of coated surfaces via the accelerated aging conditions.

I.   *Take initial data of the samples* - After labelling the samples, visual inspection and images of the coated surface are taken. This allows detection of possible failures on the coatings such as erosion, blistering, cracking, scaling and others. In addition, the initial thickness of the coating is measured. Images of the side and top views are taken.

II. *Measure impedance* - Impedance measurements are carried out with time at the open circuit potential (OCP) condition with 10 mV potential perturbation.

III. *Measure pH* - The acidic test solution in contact with the coated surface is collected for pH measurements. The pH values are recorded over time.

IV. *Measure coating thickness* - Ensure the sample is dry before making measurements. Place drops of water in selected locations. Record all 15 thickness measurements (3 measurements per location, 5 locations on sample) with the Positector 200 Thickness Gage and record the minimum, maximum and average of each sample.

V.   *Visual Inspection* - Perform a visual inspection and document the exposed coated surface with photographs (side and top views). This step is repeated at least once a week. Inspect and record the presence of possible coating's failures.

VI. *Erosion* - The specimen is eroded with a small, circular wire brush in a circular motion across the samples' surface for approximately 1 minute.

VII.   *Acid replacement* - Add 200 mL of the acid solution with adjusted pH or new in the corresponding acrylic container, exposing the coated concrete sample to the acidic environment.

VIII.   Once a week, repeat steps II through VII for each sample.

Measurements

Several durability measurements such as visual inspection, pH changes of the acid solution, coating thickness, coating adhesion, failures identification/evaluation, impedance measurements, as well as surface characterization including x-ray diffraction (XRD), scanning electron microscopy with energy dispersive x-ray (SEM-EDS) and others will be performed for evaluating the potential coatings. Visual inspection of the coated specimens was conducted before, during and after the aging tests and images, thickness and failure identification and evaluation were recorded for each time. Because this is an ongoing investigation, surface characterization is not completed and will not be included in this summary document. Table 13 summarizes the measurements that will be used to evaluate the coating performance.

Table 13. Measurements to Evaluate Coating Behavior

Test	Age	Method
Visual inspection (failures)	Over time	ASTM D6577 [4]
Coating thickness	Over time	Coating Thickness Gauge
Water absorption	Over time	Electrochemical
Coating protective properties (impedance)	Over time	ASTM D6577 [4], Electrochemical
pH change (solution)	Over time	pH measures
Adhesion	before/after test	Pull-off test, ASTM D7234 [5], ASTM D4541[6]
Surface characterization (SEM-EDS, XRD, IR.)	before/after test	

Coating thickness measurements were conducted in 5 different locations of the coated surface of each sample, over time, using a Positector 200 Thickness Gage. For each location, at least three measurements were taken. Average values were calculated to get information of the coating's durability.

The evaluation of the failures (blistering, cracking, erosion, etc.) was performed by visual comparison between the samples studied (three replicates) and standard photographs specifically designed for each defect as well as the reference sample (not exposed), conforming to the ASTM D714 [7], ASTM D772[8], and ASTM D661 standards [9].

The pH of the acid solutions was measured with time to control and keep the concentration constant. By using the pH formula, the concentration of the acid solutions, 0.5M, was determined and compared with the original pH value (0.3). The deviation from the original value would indicate coating acid attack. The deviation calculated was used to determine the volume of concentrated acid to be added to keep the concentration of the solution constant.

Impedance measurements were also performed on the coated surfaces providing useful information about the coating protective properties related to durability. The impedance measurements were conducted over time using a PMC-1000 multichannel potentiostat, at the open circuit potential (OCP) condition with 10 mV potential perturbation. Measurements were performed at a frequency range from 1MHz to 1Hz. A three-electrode arrangement was used using a saturated calomel reference electrode as a reference electrode, a platinum mesh as the counter electrode, and the coated sample as the working electrode.

Subtask 20.1.1: Results and Discussion

Carboline coatings

The Carboline coating system under evaluation is composed of three different coats: 1) a moisture-tolerant epoxy primer for steel and concrete, 2) a vinyl ester primer for steel and 3) a flake filled, thermosetting polyester topcoat resistant to abrasion. Because this is an ongoing investigation, the preliminary evaluation of the coating was done based on visual inspection, failure analysis and coating thickness measurements.

Visual inspection and failure analysis

Figure 157 shows images of Carboline-coated specimens before and during accelerated aging conditions. The samples presented here, with (CT1-1, CT7-1) and without (CT3-2, CT5-1) surface preparation, as well as aged (CT1-1, CT3-2) and non-aged (CT5-1, CT7-1) concrete substrates, before coating application, are representative of all test cases (CT1-CT8).

In general, no failures were observed on the coated surfaces after 33 days of accelerated aging, only the detachment of some protruded coarse aggregates on the CT1-1 sample. The loss of surface material (coarse aggregates) will promote a faster deterioration of the coating, starting from the surrounding areas. The failures analyzed included blistering, cracking and scaling. The detachment of some coating particles during the erosion of the samples was also detected that was also observed in the acidic test solution.

The preparation of the substrate greatly determines the durability of the coating. In this study, selected samples received surface preparation (CT1-1, CT7-1) and for comparative purposes another group did not receive preparation (CT3-2, CT5-1). In general, a difference in the coating behavior among samples with and without surface preparation was not observed, thus far.

However, the presence of exposed rebar before coating application (samples CT1-1 and CT3-2 are representatives of this case) could lead to future failures. Peeling or detachment of the coating on top of the rebar was also not observed. Once the steel rebar is oxidized, the corrosion products formed could lead to the coating failure.
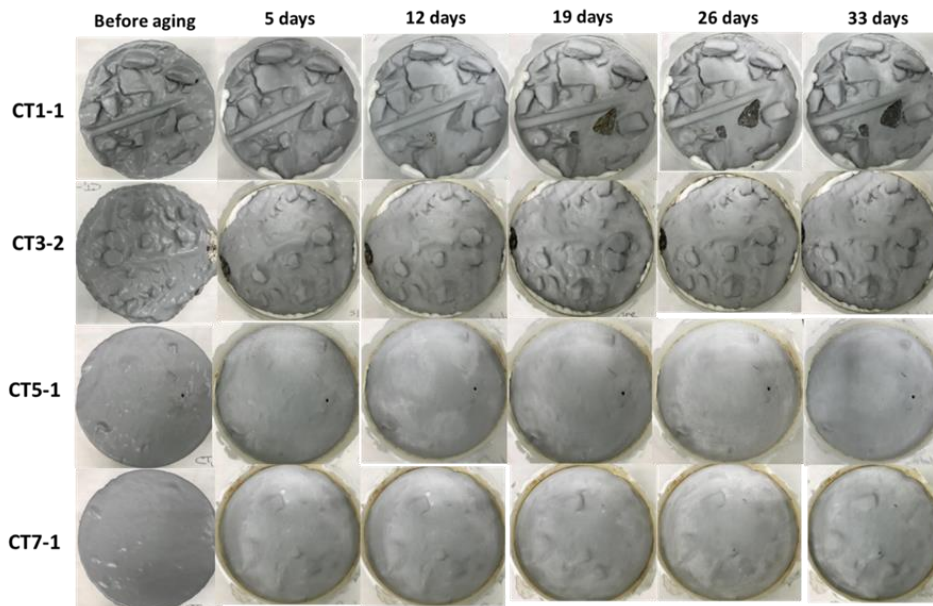
Figure 157. Images of top view of Carboline-coated samples, with (CT1-1, CT7-1) and without (CT3-2, CT5-1) surface preparation, before and during accelerated aging

Coating thickness

The thickness of the coatings was monitored over time. This parameter gives quantitative information of the coatings related to its durability. Due to the accelerated aging of the coatings, erosion combined with the acid attack, a deterioration of the coating properties and a decrease in the thickness over time is expected.

The coating type will also determine the deterioration rate. The Carboline coating is a coating system where the topcoat is a thermosetting polyester resistant to abrasion. A slower deterioration of the coating and consequently of the thickness is therefore expected.

Figure 158 shows the evolution of the thickness over time for selected Carboline samples. In general, the coating thickness decreases over time for all selected test cases. The lowest thickness is observed on CT1 samples. The rest of the samples, CT3, CT5 and CT7, show a similar behavior of thickness.
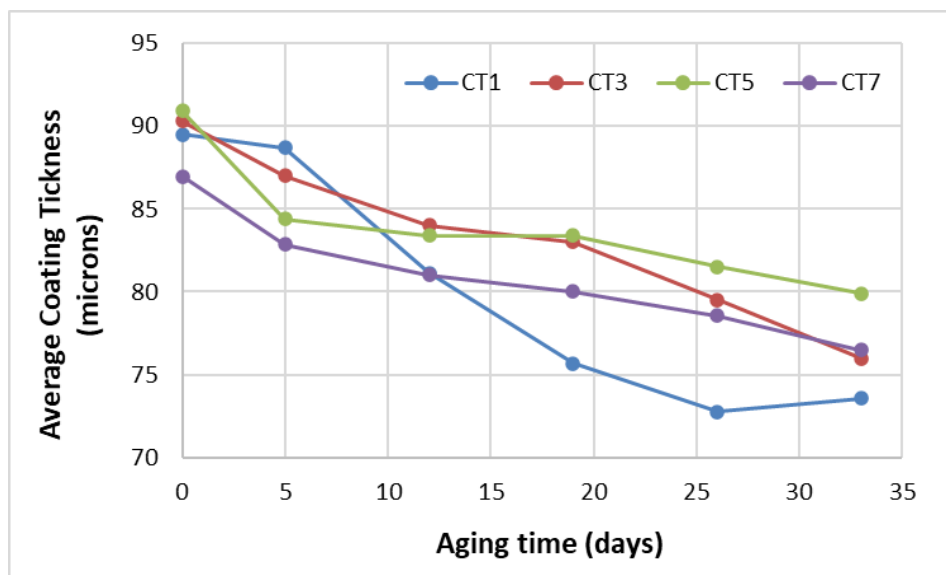
Figure 158. Average thickness of selected Carboline-coated samples, with (CT1, CT7) and without (CT3, CT5) surface preparation during accelerated aging.

The thickness loss of selected coatings was calculated with the initial and final values. As a result, coated samples with surface preparation, CT1 and CT7, had a thickness loss between 10-11%, from the initial value. For the samples without surface preparation, CT3 and CT5, the thickness loss ranged between 10-14% from the initial value. These values are very similar and there is no evidence, thus far, that the surface preparation reduced thickness loss.

Belzona coatings

The Belzona 4311, a single epoxy coating resistant to chemicals, is under evaluation. The evaluation of the coating was done based on visual inspection, failure analysis and coating thickness measurements.

Visual inspection and failure analysis

Figure 159 shows images of Belzona-coated specimens before and during accelerated aging conditions. Only Belzona samples without rebar are under evaluation so far. The samples presented here, with (BT2-1, BT8-1) and without (BT4-1, BT6-1) surface preparation, as well as aged (BT2-1, BT4-1) and non-aged (BT6-1, BT8-1) concrete substrates, before coating application, are representative of all test cases (BT1-BT8).

In general, no blistering, cracking, or scaling failures were observed on the coated surfaces after 35 days of accelerated aging. However, an increment of the coating's deterioration over time for all tested samples was observed. The deterioration is located on the area where the erosion takes place, and it increases over time. After 14 days of accelerated aging, it is more evident how the color of the coating is lighter due to the loss of material (coating particles) from the aging process. The coating particles detached from the surface were observed in the acidic test solution. In

addition, as a general trend, a difference was not observed in the coating behavior among samples with (BT2-1, BT8-1) and without (BT4-1, BT6-1) surface preparation.
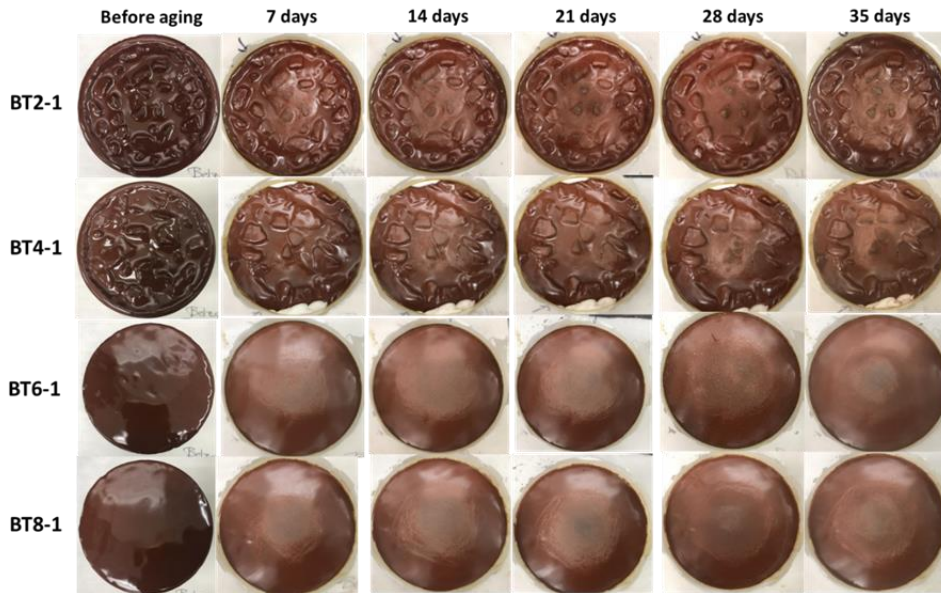
Figure 159. Comparative images of the top view of Belzona-coated specimens, with (BT2-1, BT8-1) and without (BT4-1, BT6-1) surface preparation, before and after aging conditions.

Coating thickness

The thickness of the Belzona coatings was monitored over time to get insight about the coatings' durability. Figure 160 shows the evolution of the thickness over time for Belzona samples. In general, the thickness decreases over time for all test cases. Also, no matter the test case, the thickness of the samples shows a similar trend over time. Because the Belzona material used to cover the concrete samples was a single epoxy coating, it is not expected to be resistant to erosion. It is expected to deteriorate faster and consequently a have a greater thickness loss.
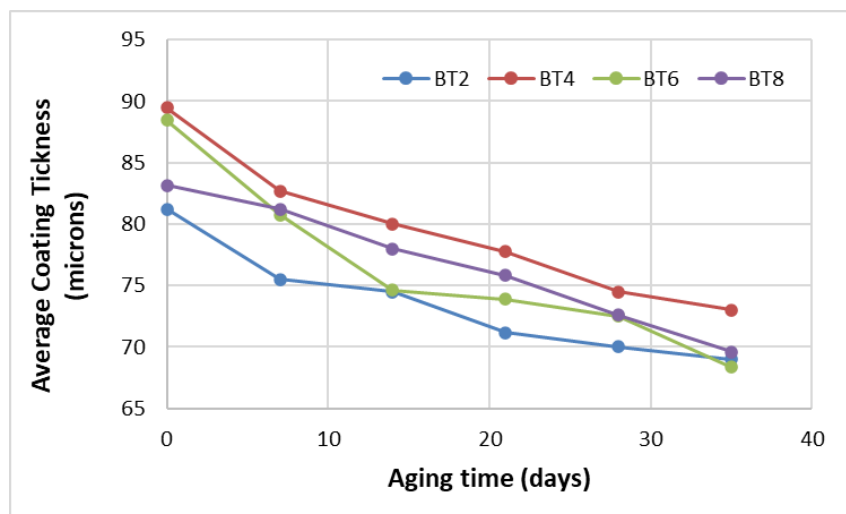
Figure 160. Average thickness of selected Belzona-coated samples, with (BT2, BT8) and without (BT4, BT6) surface preparation, during accelerated aging.

The thickness loss of selected coatings was calculated with the initial and final values. As a result, coated samples with surface preparation, BT2 and BT8, had a thickness loss between 7-20%, from the initial value. For the samples without surface preparation, BT4 and BT6, the thickness loss ranged between 15-23%. The results suggest that samples with surface preparation have lower thickness loss compared with those without preparation.

Sherwin-Williams coatings

A coating system composed of multiple coats, 1) a pre-prime epoxy coating and 2) a polyurea topcoat, was the Sherwin-Williams material under investigation. The coating system should provide barrier protection to the concrete substrate against the aggressive environment. Also, the polyurea topcoat, an abrasion resistant coating, can help in the reduction of the erosion effect caused by the heavy winds inside the tunnel combined with debris.

At the time this summary document was written, Sherwin-William-coated samples were received, and only initial information of the coated samples is presented here. The initial information of the coating includes visual inspection and failure analysis.

Visual inspection and failure analysis

Figure 161 shows representative images of Sherwin-Williams-coated specimens before the beginning of the accelerated aging (initial conditions). The samples presented here include, with (ST1, ST2, ST7 and ST8) and without (ST3, ST4, ST5 and ST6) surface preparation, as well as aged (ST1, ST2, ST3 and ST4) and non-aged (ST5, ST6, ST7 and ST8) concrete substrates, before coating application, which are representative of all test cases (ST1-ST8). No failures were observed on the coated surfaces at the initial conditions. The failures analyzed included blistering, cracking and scaling.
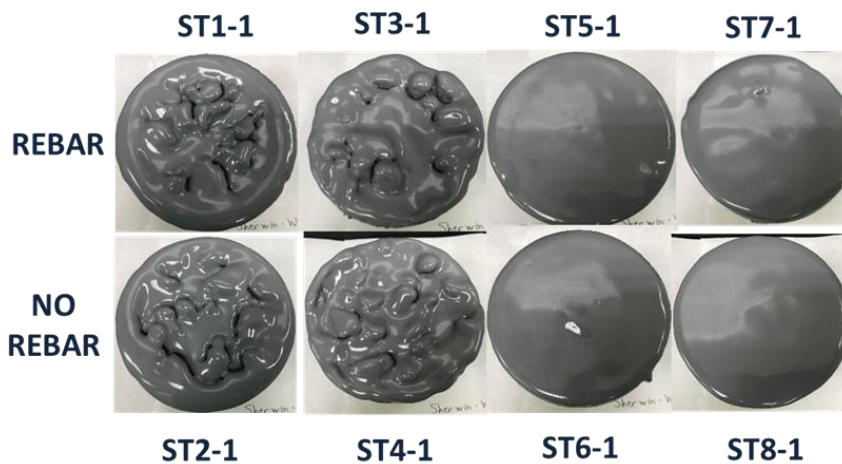
Figure 161. Top view of Sherwin-Williams-coated samples, with (ST1, ST3, ST5 and ST7) and without (ST2, ST4, ST6 and ST8) surface preparation, at the initial conditions. Only Replicate 1 is presented here, representative of all replicates

Subtask 20.1.1: Conclusions

Visual inspection, failure analysis and thickness measurements showed slow degradation of the coatings over time. The degradation of the coatings was characterized by loss of coating particles

and in some cases, detachment of some coarse aggregates. The reduction of thickness over time, for all tested coatings, indicated degradation and loss of protective properties. The erosion of the surfaces played a key role in the degradation of the coatings.

Subtask 20.1.1: References

1. Bob J. Gilliam et al. "Inspection and Assessment of the H-Canyon Ventilation System at the Savannah River Site". Phoenix, Arizona. Waste Management Conference, 2015.

2. Staff Report, Defense nuclear facilities safety board. "H-Canyon exhaust tunnel fragility analysis input and assumptions". 2018.

3. Echeverria, M. et al. "Aging of concrete for the evaluation of repair materials to protect the HCAEX tunnel at Savannah River". Waste Management 2020 Conference, Phoenix, AZ, March 2020. (Best Poster of Track). Paper # 20301

4. ASTM D6577 "Standard Guide for Testing Industrial Protective Coatings". 2019.

5. ASTM D7234-21 "Standard Test Method for Pull-Off Adhesion Strength of Coatings on Concrete Using Portable Pull-Off Adhesion Testers". 2021.

6. ASTM D4541. "Standard Test Method for Pull-Off Strength of Coatings Using Portable Adhesion Testers". 2017.

7. ASTM D714-02. "Standard Test Method for Evaluating Degree of Blistering of Paints". 2017.

8. ASTM D772-18. "Standard Test Method for Evaluating Degree of Flaking (Scaling) of Exterior Paints". 2018.

9. ASTM D661-19. "Standard Test Method for Evaluating Degree of Cracking of Exterior Paints". 2019.

Subtask 20.1.2: Establish a Ranking of Coating Candidates from Research Findings

Subtask 20.1.2: Methodology

In this investigation, four coatings candidates, Carboline, Belzona, Sherwin-Williams and Framatome were selected for the accelerated aging and evaluation. In this ongoing investigation, only two coatings, Carboline and Belzona, were exposed to accelerated aging conditions thus far and will be considered for this preliminary selection.

The ranking was based on the coating's performance to the accelerated aging conditions, 0.5M nitric acid solution and erosion. Parameters considered for the ranking included preliminary results on 1) visual inspection, 2) failures, 3) thickness loss and 4) impedance.

Subtask 20.1.2: Results and Discussion

Results of visual inspection, coating thickness and electrochemical measures supported the selection. Carboline coating system showed less thickness loss than Belzona single coating. Also, impedance measurements confirmed greatest drop of the impedance modulus for Belzona coating thus far, indicative of reduction of the protective properties. Preliminary results suggest that Carboline coating system will offer greater barrier protection and protective properties than Belzona single coating in aggressive environments with nitric acid and erosion.

Subtask 20.1.2: Conclusions

Preliminary results suggest that the Carboline coating system will offer greater barrier protection and protective properties than the Belzona single coating in aggressive environments with nitric acid and erosion.

Subtask 20.2: Corrosion Evaluation of Steel Canisters for Hanford Integrated Disposal Facility

Subtask 20.2: Introduction

A current challenge for DOE and relevant DOE sites is to understand the durability of the steel canisters/containers that will contain low-activity waste (LAW) and secondary waste forms, encapsulated in glass and grout respectively, and that will be placed within the Integrated Disposal Facility (IDF) at Hanford. Currently, corrosion data of the steel and weld regions of the canisters at Hanford that is exposed to groundwater is limited. In addition, there is limited information on groundwater in contact with waste forms. The primary technical need is to study the corrosion rate of the steel canister's exterior that is exposed to Hanford groundwater and determine how well it shields the waste form that is inside the canister from exposure. Additionally, FIU will investigate how the corrosion rate varies in situations where groundwater has also contacted the waste forms.

Subtask 20.2: Objectives

The objective of this subtask is to evaluate material (steel 304, carbon steel, mild steel and weld regions) behavior of the canisters in environments similar to IDF conditions and obtain site-specific corrosion data through electrochemical measurements. Obtaining such data can be used to predict the canister's useful life. The following subtask will be executed to meet this objective:

- Obtain site-specific corrosion data of the 304 SS canister/container material exposed to simulated IDF conditions by using electrochemical techniques. The corrosion performance of 304 SS canister/container material and the effect of the surface condition will be studied. A solution that simulates Hanford groundwater at the IDF will be used.

Subtask 20.2.1: Corrosion Behavior of Canister Materials for the Steel Corrosion Study at Hanford - 304 Stainless Steel

Subtask 20.2.1: Methodology

In this section, information about the test plan, specimens' preparation, test setup and electrochemical measurements is presented.

Test Plan

Table 14 shows the test plan developed to get corrosion data of various canister/container materials exposed to simulated Hanford IDF groundwater. Several electrochemical tests and surface characterization tests are listed. The candidates' materials under study are 304SS, 316SS, Hastelloy, 409SS, high carbon steel and ASTM A-569-93 Carbon Steel. Table 15 shows the reason for using each candidate material.

Table 14. Test Plan

Candidate Sample Type	Tests							
	Potentiodynamic Polarization		Corrosion Potential 7-28 day		Polarization Resistance during Ecorr		Post-corrosion Examination with SEM	
	GW A*	GW B*	GW A	GW B	GW A	GW B	GW A	GW B
Stainless Steel 304								
Heat Treated SS 304								
Welded SS304								
Welded SS304 - Heat Treat								
ASTM A-569-93 Carbon Steel								
high carbon steel								
Hastelloy								
316 Stainless Steel								
409 Stainless Steel								

*: GW A and GW B are two representative Hanford groundwater simulants.

Table 15. Candidate Materials Type for Canister/Container and Reason

| Candidate Sample Type	Reason
Stainless Steel 304	Glass container base material
Heat Treated SS 304	Base canister material with glass poured within
Welded SS304	Represent canister lid (weak point)
Welded SS304 - Heat Treat	Represent canister lid (weak point) after heat cycle
ASTM A-569-93 Carbon Steel	B-25 box steel type
high carbon steel	Worst case scenario
Hastelloy	Best case scenario for a container but expensive
316 Stainless Steel	55-gallon drum material
409 Stainless Steel	55-gallon drum material

Variables of interest in this study are the type of material and the effect of heat treatment and welding on the materials behavior to corrosion. Because this is a multiphase study, in this initial phase, corrosion data for 304SS canister material only is obtained.

Specimen preparation

FIU procured 304 SS square bars and threaded 316 SS rods for the preparation of the specimens. The material under study is the 304 SS. The 304 SS bar was cut to the dimensions of 0.75-inch height, 0.5-inch width and 0.5-inch thickness. The back of the sample was threaded, and a piece of 316 SS rod screwed to it to facilitate the electrical connection between the sample and the cables connected to the rod. Only the bottom squared section of the 304 SS sample was under study, with an area of 1.61 cm^2. The specimen was fixed in a cold resin that will allow only one side of the square bar (bottom) to be in contact with the solution. The surface of the sample was cleaned with detergent to remove any grease, oil or dust from the surface. The surface was grinded with 120 grit sandpaper and then, carefully washed with tap water, deionized water and dried. Once the sample was dried, it was stored in a desiccator until the beginning of the electrochemical tests.

Test setup and test solutions

Figure 162 shows the test setup inside a Faraday Cage which is used for the electrochemical measurements. A three-electrode arrangement was used to perform the measurement including a reference electrode (saturated calomel-SCE), a working electrode (the 304 SS sample) and a counter electrode (a platinum mesh). The electrodes were in contact with the test solution and only the bottom surface of the sample (working electrode) was immersed in the solution during the experiment. A PMC-1000 potentiostat was used for the electrochemical measurements, connected to the computer through the VersaStudio software.
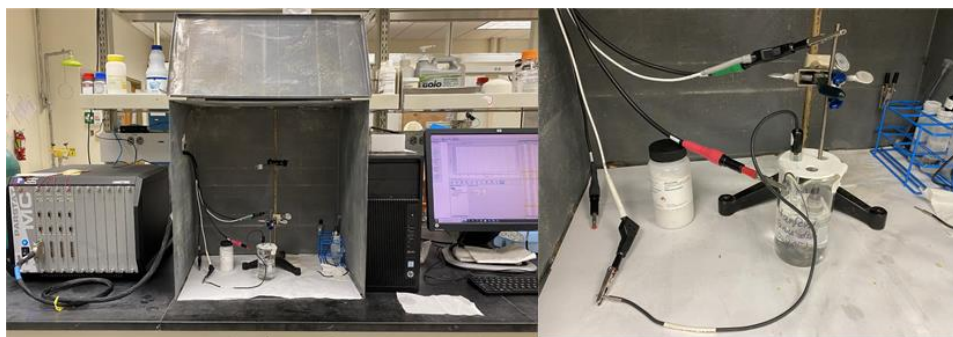
Figure 162. View of the potentiostat, the Faraday Cage and computer (left image) used for electrochemical measurements. Zoom of the experimental setup (right image).

The test solution simulates the infiltrating water that would reach the containers/canisters if the IDF surface barrier fails. Hence, the materials being studied will be immersed in this solution for the duration of the experiments. This solution will be identified as GWA. For comparative purposes, a similar solution, identified as GWB, was prepared only containing the chloride ions of the IDF Hanford groundwater recipe.

Electrochemical measurements

There are various electrochemical techniques such as the traditional direct current (dc) techniques, the well-established alternate current (ac) techniques including the electrochemical impedance spectroscopy and others, as well as newer techniques such as electrochemical noise analysis [2]. Corrosion potential (Ecorr), potentiodynamic polarization (PDP) and linear polarization resistance (LPR) are some of the measurements that were conducted on the 304SS material.

Sequence of measurements: Ecorr-LPR-PDP

In this investigation, a sequence of electrochemical measurements was conducted on the samples as shown below:

- Ecorr for 1 hour
- LPR +/- 10 mV Vs Ecorr (@0.1667 mV/s)
- Ecorr for 1 hour
- LPR +/- 10 mV Vs Ecorr (@0.1667 mV/s)
- Repeat previous steps for 48 hours
- PDP/LV (potentiodynamic polarization/lineal voltammetry) from -300 mV Vs Ecorr to 1V Vs Reference electrode (maybe cut at 1mA/cm2)

Using the VersaStudio software, the previous sequence was created. This sequence was performed on 304SS specimens using the two testing solutions, GWA and GWB, previously defined.

Subtask 20.2.1: Results and Discussion

The electrochemical test results of the 304 SS immersed in GWA and GWB are presented in two different sections. Each section will include results of 1) corrosion potential, 2) polarization resistance (Rp) and 3) potentiodynamic polarization. Since this is an ongoing experiment, only preliminary results are presented here.

Electrochemical test results for 304SS in GWA

Corrosion potential (Ecorr)

Figure 163 shows the Ecorr of the 304SS immersed in GWA at different immersion times. Only selected Ecorr measurements in a period of 48 hours are presented in the graph. Ecorr and open circuit potential (OCP) is used indistinctly in this document. During the first 24 hours of measurement (OCP_1), the Ecorr continuously increased from ~ -240 mV Vs SCE to ~ -180 mV Vs SCE. Then, continued increasing from -180 mV Vs SCE to -110 mV Vs SCE, at the end of the last Ecorr measurement (OCP_45). From the 5th to the last measurement, Ecorr remained constant for the time tested, with small increases between each 24-hour measurement. The stabilization of the Ecorr values could suggest the possible formation of the passive film.
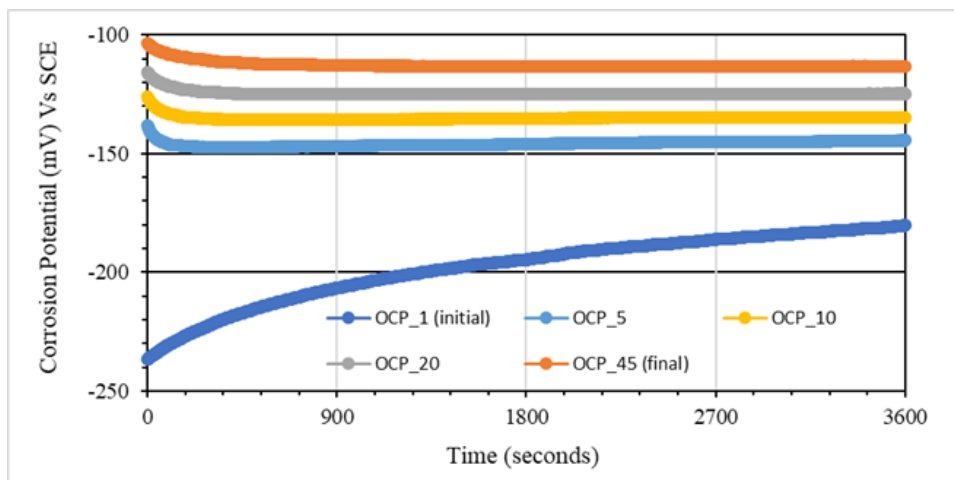
Figure 163. Corrosion potential for 304 stainless steel canister material at different immersion times in simulated Hanford groundwater A.

Polarization resistance (Rp)

Figure 164 shows the evolution of potential versus current after conducting LPR tests. Selected LPR data, initial (LPR_1), intermediate (e.g., LPR_5, LPR_20) and final (LPR_45), are plotted in this graph. In these tests, a small potential perturbation, +/- 10 mV relative to Ecorr, was applied to the specimen and the current response was measured. The potential increases from -190 mV Vs SCE to -100 mV Vs SCE. It is observed that the potential drastically increases when the current is around 0 A and the same behavior is repeated for all LPR measurements. This seems to be related with the equipment and it is only observed at lower currents, near the low current limit of the potentiostat.

Figure 164. Polarization resistance plots for 304 stainless steel canister material at different immersion times in simulated Hanford groundwater A.

Table 16 shows the electrochemical parameters calculated using the LPR data. Parameters includes the Rp, corrosion current (Icorr), current density (icorr) and corrosion rate (R).

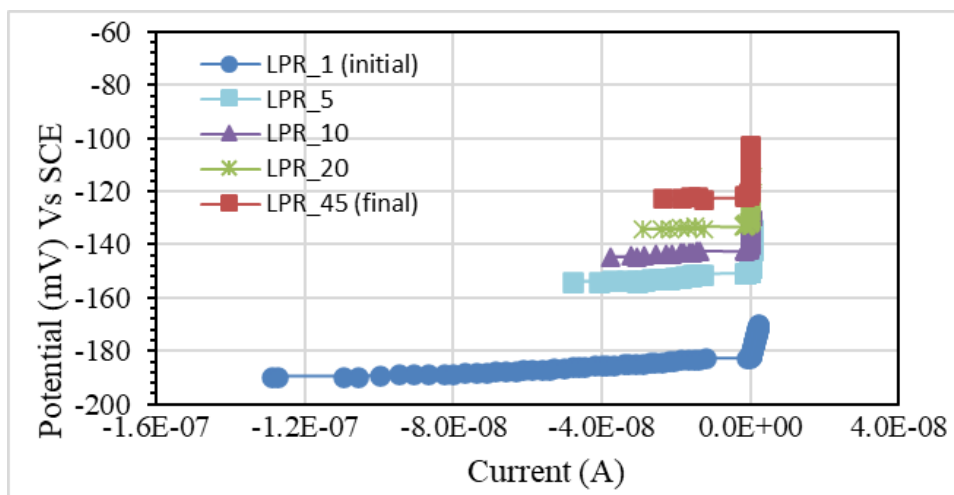**Table 16. Calculated corrosion parameters from LPR data for 304 stainless steel canister material at different immersion times in simulated Hanford groundwater A**

LPR_#	Rp [Ω]	Icorr (A)	icorr (A/cm^2)	R (g/m^{2}y)	R (μm/y)
1	4.92E7	5.28E-7	3.27E-7	29.84	3.76
5	8.11E8	3.21E-8	1.99E-8	1.81	0.23
10	2.00E10	1.30E-9	8.06E-10	0.07	0.01
20	9.38E8	2.77E-8	1.72E-8	1.57	0.20
45	1.15E10	2.26E-9	1.40E-9	0.13	0.02

First, the polarization resistance (Rp) was determined through the slope of the curve. Only the left side of the curve with respect to 0 A current was used. The Icorr was then determined by using the Stern-Geary equation (2) and the Stern-Geary constant (K) equal to 26 mV (for active steel) was assumed. The icorr and R were also determined using equations 2, 3 and 4, previously defined in materials and methods section.

The Rp is inversely proportional to the Icorr, icorr and R. It can be observed how the Rp values increase with immersion time from 4.92E7 Ω to 1.15E10 Ω and Icorr, icorr and R values decrease. The decrease of the R and icorr after 48 hours of measurement to small values of 0.13 g/m^{2}y and 1.40E-9A/cm^{2}may suggest that the steel is passivating.

Potentiodynamic polarization (PDP)

Figure 165 shows the polarization curve of 304 SS specimen immersed in GWA. This graph offers insight into the electrochemical performance of the canister material. It is noticeable that the system under study has anodic control by electron transfer and cathodic control by diffusion. Icorr and Ecorr were obtained from the Tafel method, with values 1.8E-5 A and -70 mV Vs SCE, respectively. The calculated icorr and R values (in two different units) were 1.12E-5 A/cm^2 and 1016.89g/m^{2}y and 128.07μm/y, respectively. Very high R values were obtained for the 304SS in GWA. More visual damage (pitting corrosion) was observed on the 304SS sample exposed to GWB than the sample exposed to GWA.
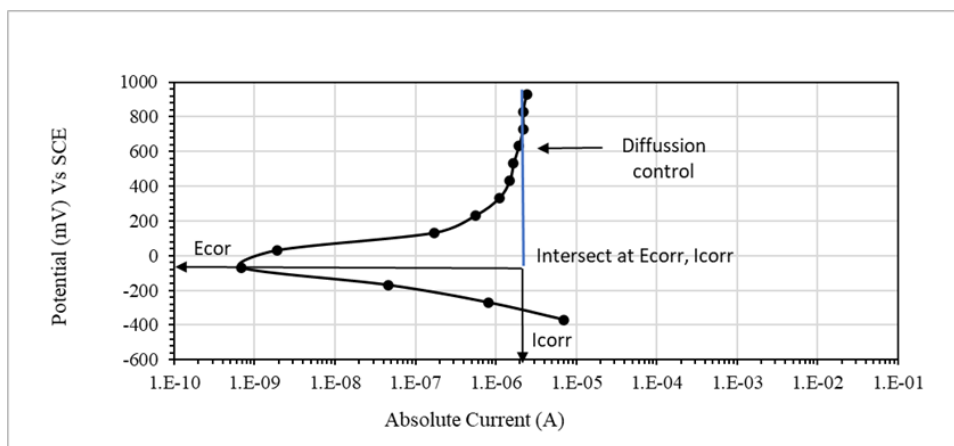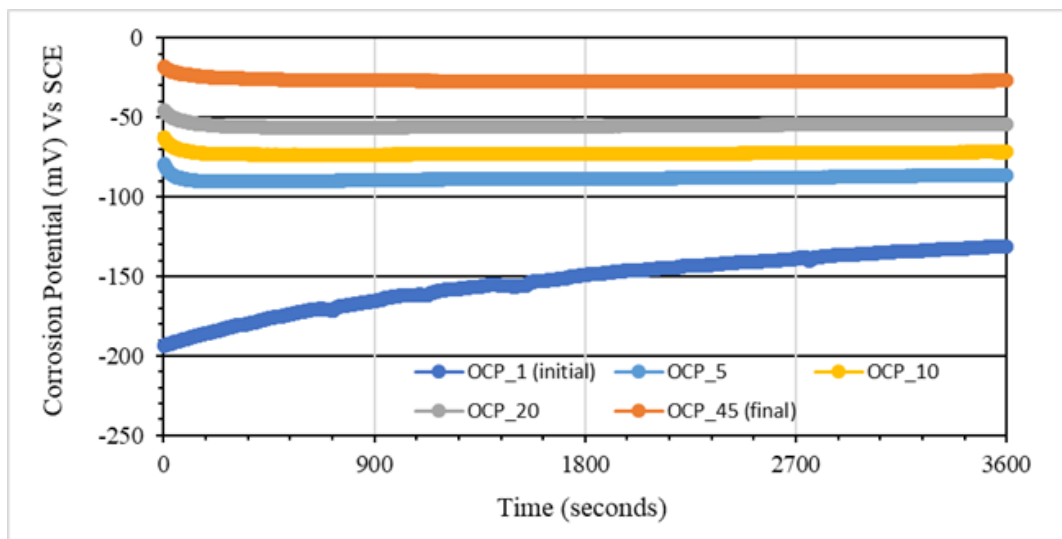

Figure 165. Polarization resistance plots for 304 stainless steel canister material at different immersion times in simulated Hanford groundwater A.

Electrochemical test results for 304SS in GWB

Corrosion potential (Ecorr)

Figure 166 shows the Ecorr of the 304SS immersed in GWB at different immersion times. Only selected Ecorr measurements in a period of 48 hours are presented in the graph. In general, a significant increase was observed from ~ -190 mV Vs SCE to ~ -20 mV Vs SCE. The Ecorr increase in GWB was greater than in GWA. At the beginning (OCP_1), the Ecorr increased from ~ -190 mV Vs SCE to ~ -140 mV Vs SCE and continuously increased from -140 mV Vs SCE to -20 mV Vs SCE at the end of the last 24-hour measurement (OCP_45). From the 5th to the last measurement, Ecorr remained constant, with small increases between each 24-hour measurement. The stabilization of the Ecorr values could suggest the possible formation of the passive film. Similar behavior was observed on the 304SS specimen when exposed in GWA.

Figure 166. Corrosion potential for 304 stainless steel canister material at different immersion times in simulated Hanford groundwater B.

Polarization resistance (Rp)

Figure 167 shows the polarization graph for the 304SS specimen immersed in GWB. A small potential perturbation, +/- 10 mV relative to Ecorr, was applied to the specimen and the current response was measured. Selected LPR data, at various immersion times, are plotted in this graph. The potential increases from -140 mV Vs SCE to -20 mV Vs SCE from the first to the last LPR measurement. It can be observed how the potential drastically increases when the current is very low (~ 0 A) and the same behavior is repeated for all LPR measurements.
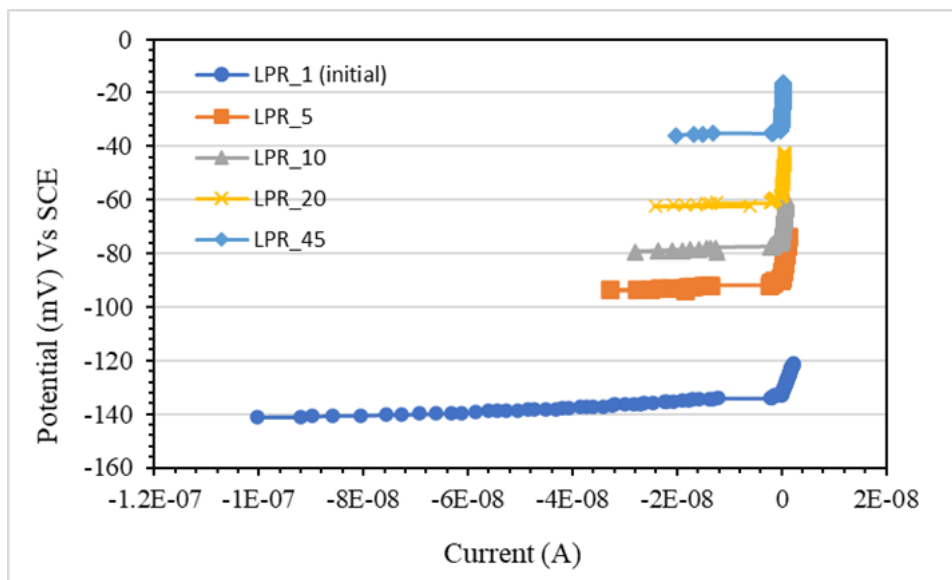
Figure 167. Polarization resistance plots for 304 stainless steel canister material at different immersion times in simulated Hanford groundwater B.

Table 17 shows the electrochemical parameters calculated using the LPR data for the 304SS immersed in GWB.

Table 17. Calculated corrosion parameters from LPR data for 304 stainless steel canister material at different immersion times in simulated Hanford groundwater B

| LPR_#	Rp [Ω]	Icorr (A)	icorr (A/cm^2)	R (g/m^{2}y)	R (µm/y)
1	7.52E+07	3.46E-07	2.14E-07	19.52	2.21
5	4.91E+07	5.30E-07	3.29E-07	29.93	3.39
10	9.08E+07	2.86E-07	1.78E-07	16.18	1.83
20	4.92E+07	5.29E-07	3.28E-07	29.87	3.39
45	3.37E+07	7.71E-07	4.78E-07	43.57	4.94

The Rp was determined using the slope of the curve. Only left side of the curve with respect to 0 A current was used. The Icorr was then determined by using the Stern-Geary equation. The icorr and R were also determined using the corresponding expressions.

The Rp values are similar, ranging from ~3E7 to 9E7, for all the immersion times. However, a slight increase is observed from LPR_10 measurement and over. The Rp is inversely proportional to the current, and R. In addition, it was observed that the highest Rp value (9.08E7 Ω) corresponded to the lowest R (16.18g/m^{2}y, 1.83µm/y). The highest R and icorr at the end of the LPR test suggests the active behavior of the material that could be related to the presence of the chloride ions in the GWB solution.

Potentiodynamic polarization (PDP)

Figure 168 shows the polarization curve of 304 SS specimen immersed in GWB. It is noticeable that the system (anodic and cathodic branches) under study is controlled by electron transfer. Icorr and Ecorr were obtained from the Tafel method, with values 1.4E-8 A and -80 mV Vs SCE,

respectively. The calculated icorr and R values (in two different units) were 8.68E-9 A/cm^2 and 0.79 g/m^{2}y and 0.1 µm/y, respectively.
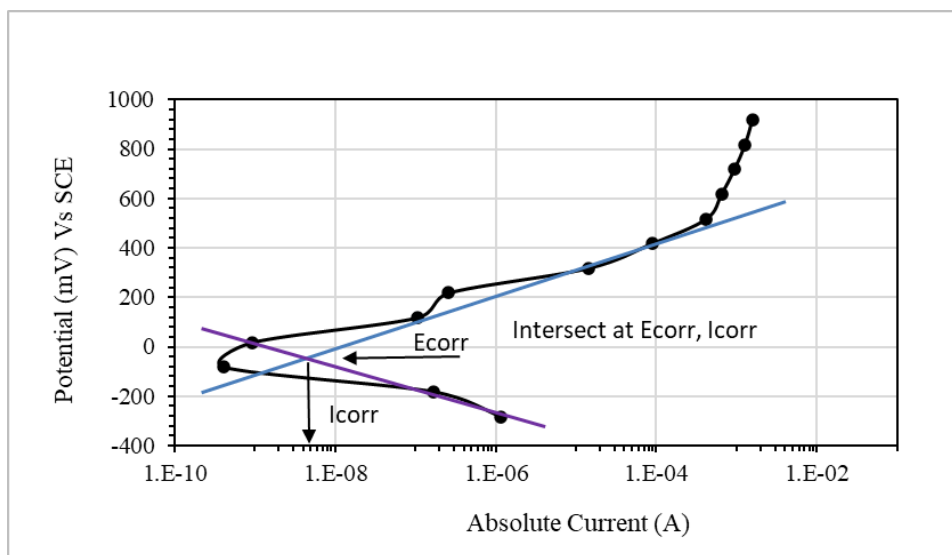
Figure 168. Potentiodynamic graph for 304 stainless steel canister material at different immersion times in simulated Hanford groundwater B.

Subtask 20.2.1: Conclusions

Electrochemical measurements included corrosion potential, linear polarization resistance and potentiodynamic polarizations allowing useful corrosion data of the canister materials to be acquired. Potentiodynamic curves of the 304 stainless steel specimens exposed to simulated Hanford groundwater (GWA) showed anodic control by electron transfer and cathodic control by diffusion. However, 304 stainless steel samples exposed to a reference solution (GWB), only with chloride ions, depict anodic and cathodic control by electron transfer.

Subtask 20.2.1: References

1. Serne R.J. et al. "Extended leach testing of simulated LAW cast stone monoliths". Pacific Northwest National Laboratory. RPT-SWCS-010, Rev. A. June 2016.

2. Marcus, F. and Mansfeld, F. "Analytical methods in corrosion science and engineering". Taylor and Francis group. 2005.

3. Kruger, J. and Hardman, V. Kay. "Current understanding of pitting and crevice corrosion and its application to test methods for determining the susceptibility to such corrosion of nuclear waste metallic containers". Center for Materials Science. Washington, D.C. 20234. 1982.

4. Hiromoto S. "Corrosion of metallic biomaterials" in Metals for Biomedical Devices, 2010, Book chapter.

5. R.A. Buchanan, E.E. Stansbury, in Handbook of Environmental degradation of materials, 2012.

6. ASTM G102 − 89 (Reapproved 2015). "Standard practice for calculation of corrosion rates and related information from electrochemical measurements". ASTM International.

CONFERENCE PARTICIPATION, PUBLICATIONS, AWARDS & ACADEMIC MILESTONES

Oral and Poster presentations (presenter is underlined)

<u>B. Cintas</u>, D. McDaniel, A. Aravelli, S. Tashakori, D. Sinnott, M. Poirier, "Evaluation of Pipeline Flushing Requirements for High-Level Waste at Hanford and Savannah River", Proceedings of the Waste Management Symposia 2022, Phoenix, AZ, March 6-10, 2022.

<u>M. Boan</u>, A. Litzinger, L. Lagos, D. McDaniel, "Development and Evaluation of Aged Concrete Surfaces for the Study of Coatings for the HCAEX Tunnel at Savannah River", Proceedings of the Waste Management Symposia 2022, Phoenix, AZ, March 6-10, 2022.

A. Awwad, <u>D. McDaniel</u>, J. Rivera, L. Lagos, "Effects of Sodium Hydroxide, Temperature, and Exposure Duration on Hose-In-Hose Transfer Lines used in the Hanford Waste Transfer System", Proceedings of the Waste Management Symposia 2022, Phoenix, AZ, March 6-10, 2022.

<u>J. Adams</u>, T. Tran, A. Abrahao, A. Pappas, D. McDaniel, L. Lagos, "Radiological Surveillance of Hanford Tank Farm Using an Autonomous Mobile Platform", Proceedings of the Waste Management Symposia 2022, Phoenix, AZ, March 6-10, 2022.

A. Aravelli, R. Piloto, D. Sinnott, <u>D. McDaniel</u>, L. Lagos, B. Wiersma, "Effect of Caustic Simulant Flow on the Corrosion Characteristics of Waste Transfer Components", Proceedings of the Waste Management Symposia 2022, Phoenix, AZ, March 6-10, 2022.

<u>M. Telusma</u>, J. Natividad, D. McDaniel, L. Lagos, "High Fidelity Simulation of an Omni-Directional Wall Crawling Mobile Platform for Use Inside the H-Canyon Tunnel", Proceedings of the Waste Management Symposia 2022, Phoenix, AZ, March 6-10, 2022.

<u>S. Story</u>, D. Martin, S. Tashakori, D. McDaniel, G. Soon, L. Lagos, "Development and Deployment of the Miniature Rover for Inspection of Hanford's Double Shell Tank (DST)", Proceedings of the Waste Management Symposia 2022, Phoenix, AZ, March 6-10, 2022.

WM Student Posters

<u>Aubrey Litzinger</u> - Standard Aging of Concrete for the Study of Protection Systems at Savannah River Site (22485)

<u>Brendon Cintas</u> - Evaluation of Pipe Length on Flushing Requirements for High-Level Waste at Hanford and Savannah River (22484)

<u>Desmond Sinnott</u> - Design and Development of a Bench Scale Pipe Loop for Corrosion Monitoring Using Caustic Simulants (22506)

<u>Jeff Natividad</u> - Mechanical Updates on the Robotic System for Coating Application in Savannah River Site H-Canyon Exhaust Tunnel (22482)

<u>Joel Adams</u> - Development of Intelligent Mobile Robot Platforms for Performing Nuclear Surveillance (22499)

<u>Sebastian Story</u> - Retrofitted Pneumatic Pipe Crawler for Transfer Line Inspection of Double Shell Tanks at Hanford Site (22480)

Awards

<u>A. Litzinger</u> (DOE Fellow), M. Echeverria, L. Lagos and D. McDaniel. "Standard Aging of Concrete for the Study of Protection Systems for H-Canyon Exhaust Tunnel at Savannah River Site". (Poster). Waste Management 2022 Conference, Phoenix, AZ, March 2022. (Best Poster of Undergrad Students Category)

<u>Thi Tran</u> (DOE Fellow) (Roy G. Post Scholarship winner) – presented poster "Intelligent Data Management to Produce Digital Twins from Autonomous Robotic Platforms" (22489) during Roy G. Post Scholarship Winners Poster Display.

Academic Milestones

DOE Fellow Aubrey Litzinger graduated with a B.S. degree in Environmental Engineering in Spring 2022 and is continuing to pursue a M.S. in Environmental Engineering at FIU.

DOE Fellows Philip Moore, Sebastian Story and Josue Estrada completed bachelor's degrees in Mechanical Engineering and are continuing to pursue a M.S. in Mechanical Engineering at FIU.

ACKNOWLEDGEMENTS

APPENDIX

The following documents are available at the DOE Research website for the Cooperative Agreement between the U.S. Department of Energy Office of Environmental Management and the Applied Research Center at Florida International University:
https://doeresearch.fiu.edu/SitePages/Welcome.aspx

FIU Year 2 Annual Research Review Presentations:

1. FIU Research Review - Project 1
2. FIU Research Review - Project 2
3. FIU Research Review - Project 3 – D&D
4. FIU Research Review - Project 3 – IT ML
5. FIU Research Review - Project 4 & 5
6. FIU Research Review - Project 4 - DOE Fellow Aubrey Litzinger
7. FIU Research Review - Project 4 - DOE Fellow Aurelien Meray
8. FIU Research Review - Project 4 - DOE Fellow Joel Adams
9. FIU Research Review - Project 4 - DOE Fellow Mariah Doughman
10. FIU Research Review - Project 4 - DOE Fellow Nicholas Espinal
11. FIU Research Review - Project 4 - DOE Fellow Philip Moore
12. FIU Research Review - Project 5 - DOE Fellow Olivia Bustillo
13. FIU Research Review - Project 5 - DOE Fellow Shawn Cameron
14. FIU Research Review - Wrap Up - Project 1
15. FIU Research Review - Wrap Up - Project 2
16. FIU Research Review - Wrap Up - Project 3 – D&D
17. FIU Research Review - Wrap Up - Project 3 – IT ML
18. FIU Research Review - Wrap Up - Project 4
19. FIU Research Review - Wrap Up - Project 5